



國立臺灣大學理學院地質科學所

博士論文

Department of Geosciences

College of Science

National Taiwan University

Doctoral Dissertation

以自動化全波形地震矩逆推法與多重訊號分類

反投影法探討地震破裂特性

AutoBATS and 3D MUSIC: New Approaches to
Imaging Earthquake Rupture Behaviors

簡珮如

Pei-Ru Jian

指導教授：洪淑蕙 博士

Adviser: Shu-Huie Hung, Ph.D.

中華民國 107 年 6 月

June 2018

國立臺灣大學博士學位論文

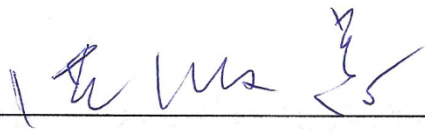
口試委員會審定書

以自動化全波形地震矩逆推法與多重訊號分類反
投影法探討地震破裂特性

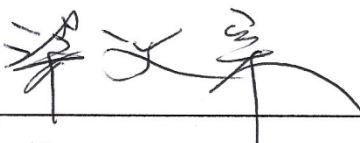
AutoBATS and 3D MUSIC : New Approaches to
Imaging Earthquake Rupture Behaviors

本論文係簡珮如君 (D01224005) 在國立臺灣大學地質科學系暨研究所完成之博士學位論文，於民國一百零七年四月二十三日承下列考試委員審查通過及口試及格，特此證明

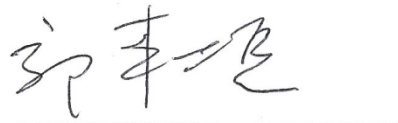
口試委員：

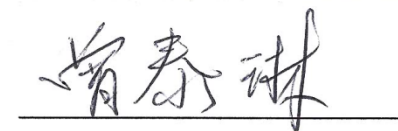


(指導教授) (簽名)









誌謝

六年前拿起了課本重新朝著二十年前已經放棄的夢想前進。在不惑與知天命之間，我完成博士學業了，雖然女科學家這個志願還是那麼遙遠。有幸的是，身邊多位女科學家給我鼓勵與激勵。感謝我的指導教授：洪淑蕙老師，她對研究有過人的執著與耐心，對科學有著最高的標準與要求；亦師亦友的曾泰琳老師，秉持著對教育與追求真理的熱忱，給予研究、生活上多方面的協助與討論。感謝孟令森老師教導陣列地震學當中研究地震破裂影像的最新技術，我才能完成這份論文。另外，感謝郭本垣老師與梁文宗老師總是適時地以各種暗喻給予我繼續的能量。而我會一直記得曾經上過喬凌雲老師的哲學式逆推與小波課。陳勁吾老師則是讓我常常想起白雪下的查爾斯河。感謝孫道遠老師，我開始學習看波形了。

從念博士開始，身邊好友用盡蠻荒之力地鼓勵我，因為研究中遇到的挫折、瓶頸與照顧家庭的分身乏術總是令人想要放棄，謝謝香蕉甜甜圈裡的每個人：最懂得其中辛苦之處的燕玲，淡定的欣穎，過去與現在進行式中一起苦熬的學弟妹：佑蘋、彥廷、亦修、姿綺、葳葳、汶珮與靜瑤。謝謝同辦公室的昱廷、思維、姿萱一直忍耐我瘋言瘋語的疲勞轟炸。幾年前認識了佩澄，我們閒聊時有最吵的笑聲。謝謝秀芳常常聽我發牢騷，還陪我一起討論照顧小孩的甘苦談，感謝玉秀、家翰與碩芬在行政上的協助。


不管在生活與研究中遇到任何困難，最大的安慰是每天都可以抱抱可愛的小 Allen，看著漸漸長大的 Allen 比寫 paper 更有成就感啊。今年我們家有兩位畢業生，Allen 從小學畢業，我從博士畢業，我們將一起邁向未來。還要謝謝多年大學好友貴美以無比的耐心教導 Allen 鋼琴與英文，讓我對 Allen 的課業上少了許多擔心，兩位家庭主婦也常常互相鼓勵與打氣呢。二十一年前我準備碩士論文時，剛退伍的老皮曾經幫忙剪貼圖片和頁碼；老皮念碩士時，我很努力督促他完成碩士論文，因為他比較喜歡研究數位相機。這些年，老皮幫忙做了很多家事(所幸我的標準是睜一隻眼閉一隻眼)，在精神上支持我繼續追求夢想。我還要感謝上蒼，我的父母依然健康，我才能無後顧之憂完成論文，最感謝的人是我的父母，他們以默默、堅毅地人生態度給予我最大的支持，以此博士論文獻給我的父親與母親。

摘要

地震發生時，除了發震時間、位置及規模，地震學家對於地震的破裂過程尤其重視，其中地震的規模與斷層型態說明每次地震釋放能量的大小以及是以何種錯動方式釋放，而地震的破裂方向、長度、時間與速度等則可闡述地震發生時的運動特性。本論文為了對地震物理特性有更多了解，先是針對台灣區域地震提出了穩定與全面性掃描的震源機制逆推，接著以三維的多重信號分類演算反投影法(MUSIC Back Projection) 分別研究了 2013 年鄂霍克次海的深震與在台灣造成死傷的美濃地震破裂行為。最後結合新的台灣區域地震震源機制目錄與西南台灣甲仙、美濃地震的地震破裂特性進一步探討此兩個造成死傷的地震的相互關係。

自從全球或區域地震網快速發展後，成就了大量的地震研究，尤其是系統化地建立全球或區域的震源機制目錄。台灣自 1995 年設置寬頻地震網以後，便定期提供震源機制目錄，然而以人工選取資料和參數的地震矩逆推法既耗時亦無法迅速提供防災資訊。本論文提出了以自動化方式同時全面掃描不同逆推設定進行地震矩逆推而得到最後的震源機制解，逆推設定包括三種選站策略、濾波頻率及四組不同莫合面深度的速度構造。並以最新 1995 至 2016 年的地震矩震源機制目錄得出新的地震矩與芮氏規模的關係式。此全新自動化逆推將為台灣地震科學訊息中心提供迅速並且穩定的震源機制解。

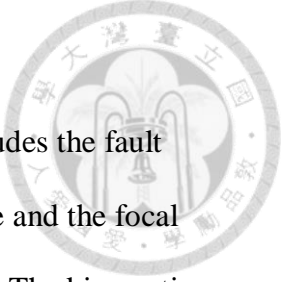
近來，世界各地為了求得更高解析度的地球物理研究，例如地球構造、地震行為、以及防災需求等而設置了高密度地震網。高密度地震網更促進了地震破裂影像研究，其中，MUSIC BP 是陣列地震學(Array Seismology)當中的最新應用：無需預設地震的斷層型態，直接以反投影方法分析地震破裂時的時間、空間演變狀態。本論文，藉由結合 P 波與 pP 或 sP 波的反投影影像使該方法得以應用於三維空間。我以三維反投影法得出 2013 年規模 8.3 鄂霍次克海深震是由兩個深度差了 10~15 公里的水平破裂所組成，兩組破裂彼此間是接近平行而往相反方向傳遞，其中往東北方向的破裂以 3.0~3.3 km/s 的速度延伸約 30~40 公里，往南南西的破裂長約為 80 公里，破裂速度增加為 4.25~4.8 km/s。推測往東北方向較短且較慢的破裂與太平洋板塊北端因受軟流圈角落流或是背景地幔加溫有關。



台灣西南部於 2010 及 2016 年分別發生了造成死傷的甲仙與美濃地震，本論文首度嘗試以反投影法解析規模 6 左右位於中地殼(mid-crust)的地震破裂特性，除了結合 P 波與 pP/sP 波的反投影影像，我們也分析全球的 P 波位移波形，藉由地震破裂具有方向性之性質來驗證反投影法影像。經過分析，我們發現這兩個地震有許多相似之處，包含接近的震央位置、震源機制，並且兩起地震以相近的破裂(2.0~2.5 km/s)速度往西北西方向破裂，因此我將兩起地震視為一組雙震(doublet)。反投影法影像結合餘震分布，我發現兩個地震的破裂區域是分開並且呈現互相平行。進一步大膽假設此雙震發生於一個位在中地殼的盲斷層上，而該區域較低的 b 值暗示該斷層長期累積應力，而無論是甲仙或是美濃地震之後，另一個破裂區域都出現震後庫倫應力大幅增加卻無任何餘震被觸發，因此推測兩個破裂區域屬於彼此獨立分開而且是斷層上兩個強補釘區域(asperity)。綜合破裂特性、b-值及庫倫應力計算，此雙震系列由較深的補釘率先破裂釋放長期累積的應力，接著較淺的補釘或許是被觸發卻延遲而發生了更大規模的美濃地震。

關鍵字:地震矩逆推、自動化震源機制解、多重信號分類演算、反投影法、地震破裂、鄂霍次克海深震、甲仙地震、美濃地震。

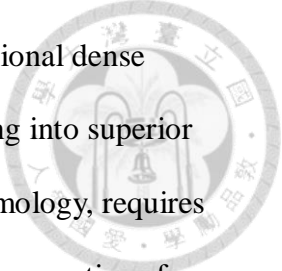
Abstract



The key knowledge of what happened during an earthquake includes the fault types, seismic energy and the rupture process. The moment magnitude and the focal mechanism tell how much and how an earthquake releases the energy. The kinematic properties of an earthquake moreover represent the rupture length, duration, propagation and speed. In this thesis, I dedicate on understanding the earthquake rupture properties by developing new automatic moment tensor (MT) inversion scheme for compiling reliable regional MT solutions and applying Multiple Signal Classification Back Projection (MUSIC BP) for earthquake rupture imaging including the 2013 Okhotsk deep earthquake and 2016 catastrophic Meinong earthquake in Taiwan. With the aid of AutoBATS MT catalog and MUSIC BP method, I further probe in to explore interacts of 2010 Jiashian and 2016 Meinong earthquakes.

The global/regional seismic networks facilitate the explosion growth on the earthquake studies especially on systematically compiling global/regional focal mechanism catalogs. In 1995, Taiwan participated in developing the Broadband Array for Taiwan Seismology (BATS) network and determining the regional CMT catalog (BATS CMT) routinely but manually. Hence I develop the new automatic MT inversion algorithm which provides more reliable and stable MT solutions by performing the MT inversion with comprehensive scanning of inversion settings of three station-choosing criteria, frequency bands and four moho-depth velocity models. A new M_W - M_L relation is updated with the complete AutoBATS MT catalog from 1995 ~ 2016. The new near real-time AutoBATS MT algorithm is employed for providing real time MT solutions for Data Management Center of IES (DMC-IES).

The ambitions of studying earthquakes, earth structures, especially the earthquake



engineering for seismic hazard prevention expedite the worldwide/regional dense seismic networks development and push the earthquake source imaging into superior high resolution level. The MUSIC BP, a new application of array seismology, requires no prior fault plane information to reveal the spatiotemporal rupture propagations for earthquakes. Here, I adopt the MUSIC BP method to three dimension and improve the spatial resolution effectively by integrating the BP images of direct P wave and depth phases. The 3D BP images of P- and pP-waves reveal the complex rupture behavior of 2013 great Okhotsk deep earthquake: two-stages of anti-parallel subhorizontal ruptures occurring at different depth. The depth aperture between two ruptures is about 10~15 km. The 1st rupture stage propagated NE-ward with speed of 3.0~3.3 km/s extending for about 30~40 km. Then the SSW-direction deeper rupture elongated for about 80 km with speed of 4.25~4.8 km/s. The initial slow and restricted NE-ward rupture may relate with the warmer northern tip of the Pacific slab which is heated by the ambient mantle and corner asthenosphere flow.

Contributed by the capability of integrating BP images of depth phases with P-wave, the rupture characteristics of two Taiwan mid-crust earthquakes with magnitude 6+ could be revealed for the first time: the 2010 Jiashian and 2016 Meinong earthquakes. In addition, the directivity analysis of global vertical displacement waveforms is included to ascertain the BP results of two earthquakes. I concluded that both earthquakes rupture toward NW-direction with comparable rupture speed of 2.0~2.5 km/s and two closed by rupture zones along with the corresponding aftershock distributions are well separated. From the similar focal mechanisms, rupture properties and close epicenters of two earthquakes, I infer those as the SW-Taiwan doublet events which might occur on a mid-crust unknown blind fault. The overall low b-value of the

rupture area implies that this strong blind fault has been sustained the stress accumulation for at least 20 years. Two isolated parallel rupture zones are considered as two strong asperities because neither the Jiashian nor Meinong earthquakes induce any aftershock activities across to the other rupture zone where inherited great increase of static stress change after the mainshock. In summary, the earthquake rupture properties, b-value and Coulomb stress change studies support the assumption that the deeper asperity (2010 Jiashian event) initiated the stress releasing process and might delaying trigger the shallower asperity (2016 Meinong event) to further release the long-time accumulated stress.

Keywords: moment tensor inversion, automatic MT solutions, AutoBATS, MUSIC, back projection, earthquake rupture imaging, Okhotsk deep earthquake, Jiashian earthquake, Meinong earthquakes.

Table of Contents



口試委員會審定書.....	i
誌謝	ii
摘要	iii
Abstract	v
Table of Contents	viii
List of Figures	xi
List of Tables	xiv
Chapter 1 Introduction	1
Chapter 2 A new automatic full-waveform regional moment tensor inversion algorithm and its applications in the Taiwan Area	13
2.1 Abstract.....	13
2.2 Introduction.....	14
2.3 Moment tensor inversion and regional waveform data	19
2.4 Automatic determination of the optimal MT solution with thoroughly scanned parameters	22
2.5 Comparisons and discussions	33
2.5.1 Consistency between Global CMT and AutoBATS MT	33
2.5.2 Comparisons between the original BATS and new AutoBATS MT solutions...	38
2.5.3 Moment magnitude and local magnitude relationship for Taiwan.....	41
2.5.4 Seismotectonic features revealed by AutoBATS MTs	44
2.6 Conclusions.....	47
Chapter 3 3D MUSIC back projection rupture images of the 2013 great Okhotsk deep earthquake sequence	49

3.1	Abstract.....	49
3.2	Introduction.....	50
3.3	Method and data.....	56
3.4	3D BP rupture image of the 2013 Okhotsk earthquake sequence.....	60
3.4.1	Two-stage antiparallel subhorizontal rupture	60
3.4.2	Super shear ruptures of two aftershocks	65
3.5	Synthetic examination	68
3.6	Discussions	75
3.7	Conclusions.....	83
Chapter 4 Rupture characteristics of the 2016 Meinong earthquake revealed		
by the back-projection and directivity analysis of teleseismic broadband		
	waveforms	84
4.1	Abstract.....	84
4.2	Introduction.....	85
4.3	Methods and data	88
4.4	Back projection source image	89
4.5	Rupture directivity and source radiation analysis	96
4.6	Discussions and conclusions.....	98
Chapter 5 The 2010 Jiashian and 2016 Meinong earthquakes: doublet		
	ruptures interact across two strong asperities	100
5.1	Abstract.....	100
5.2	Introduction.....	101
5.3	The MUSIC Back Projection and data	107
5.4	Rupture Characteristics of the Jiashian Earthquake	109
5.4.1	Back Projection Rupture Image.....	109
5.4.2	3-D Rupture Directivity Analysis	114

5.5	The 2010 Jiashian and 2016 Meinong doublet sequence	119
5.6	The frequency-magnitude distribution (FMD) and the static stress transfer in Southwestern Taiwan.....	123
5.7	Conclusions.....	130
Chapter 6	Appendixes	131
6.1	Supplementary material of Chapter 4.....	131
6.2	Supplementary material of Chapter 5.....	136
Reference	145

List of Figures

Figure 1.1 Flowchart of new real-time AutoBATS MT inversion scheme:	4
Figure 1.2 Illustration of a 3D back projection method and the smearing effects.....	8
Figure 2.1 AutoBATS MT solutions for earthquakes from May 1996 to April 2016.	18
Figure 2.2 MT inversion results for the earthquake on 2015/05/25 ($M_L=4.9$) in southern Taiwan.....	28
Figure 2.3 MT inversion results for the intermediate-depth earthquake on 2014/12/10 ($M_L=6.7$) beneath the Ryukyu subduction zone.	29
Figure 2.4 Number of events, Average K-angle and CLVD component with respect to M_w	32
Figure 2.5 Diagram illustrating the consistency between AutoBATS MT and Global CMT.	34
Figure 2.6 Comparisons of the focal mechanism and centroid depth between AutoBATS and Global CMT catalogs.	37
Figure 2.7 Comparisons of the focal mechanism and centroid depth between AutoBATS and BATS catalogs.....	40
Figure 2.8 M_w differences between AutoBATS and Global CMT catalog and relation of $M_{w(ABATS)}$ and $M_{L(CWB)}$	42
Figure 2.9 Cross-sections of focal mechanisms from AutoBATS catalog.	46
Figure 3.1 Historical deep-focus seismicity of Kuril subduction zone since 1900.	51
Figure 3.2 Coherently aligned vertical seismograms and seismic networks used for BP images.	59
Figure 3.3 High frequency P-wave (0.5~2.0 Hz) 3D BP imaging snapshots for the mainshock.	61
Figure 3.4 Low frequency (0.125~1.0 Hz) 3D BP imaging snapshots for mainshock. ..	64
Figure 3.5 3D BP imaging results summaries for the mainshock.	65
Figure 3.6 Coherently aligned vertical seismograms of two aftershocks from EU seismic network.....	67
Figure 3.7 High frequency P-wave 3D BP images of two aftershocks by using EU array data.....	67
Figure 3.8 Synthetic tests of vertical rupture scenarios.	70

Figure 3.9 Synthetic tests of SE-ward dipping rupture scenario.	72
Figure 3.10 Synthetic tests of two-stage anti-parallel rupture scenarios.	73
Figure 3.11 The tectonic setting of northern Kuril subduction zone and the BP imaging results of 2013 great Okhotsk deep earthquake sequence, including the mainshock and two largest aftershocks.....	77
Figure 3.12 Cross-sections of the 3D BP results of 2013 Okhotsk mainshock.	78
Figure 3.13 Cross-sections of the 3D BP results of two aftershocks.....	81
Figure 4.1 Tectonic settings of Meinong earthquake and the profiles showing BP results and aftershock distributions.	87
Figure 4.2 The resulting BP images from the AU and EU seismic array.	93
Figure 4.3 Teleseismic waveforms, travel time differences between depth phases and P arrivals and the amplitude ratio of pP/sP.....	94
Figure 4.4 Directivity analysis result, the rupture distances and times at EU and AU array and the comparison of BP result with finite fault inversion.	97
Figure 5.1 Map showing seismicity and tectonic settings in Taiwan	104
Figure 5.2 The resulting BP images of 2010 Jiashian earthquake from the EU and AU seismic array.....	111
Figure 5.3 The resulting BP images of Jiashian and Meinong earthquakes.....	113
Figure 5.4 Global displacement waveforms of 2010 Jiashian earthquake.	117
Figure 5.5 The directivity analysis results and comparison with BP results for 2010 Jiashian earthquake.....	118
Figure 5.6 Fault settings for 2010 Jiashian and 2016 Meinong doublet events.	122
Figure 5.7 Earthquake numbers and temporal b-value variation in JSMN fault and Southwestern Taiwan.	125
Figure 5.8 3D sketch of fault geometry settings and the Coulomb stress change induced by Jiashian and Meinong doublet.	129
Figure A1. The epicenter and array distribution and the aligned vertical velocity waveforms of two arrays.....	132
Figure A2. Synthetic velocity seismograms on the vertical component compared with the observed ones shown in Fig. 3(a).	133
Figure A3 The P-wave ray paths, 1D average velocity model and the tomographic	

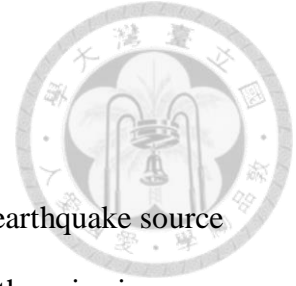
images along the ray path.....	134
Figure A4 Test for recovery of a synthetic source scenario by the MUSIC BP method.....	135
Figure B1 The seismic arrays and aligned P waves used for the BP images of 2010 Jiashian earthquake.....	138
Figure B2 Synthetic velocity seismograms for comparison with the observed ones shown in Figure 5.4	139
Figure B3 1D average velocity models and tomographic images along the ray paths of P and depth phases.....	140
Figure B4 The stress inversion results.	141
Figure B5 The earthquake numbers and temporal b-value variation.....	142
Figure B6 The 3D sketch of two causative faults for Jiashian and Meinong doublets and the Coulomb stress change induced by two earthquakes.	143
Figure B7 The 3D sketch of JSMN fault or two-separated faults and the Coulomb stress change across the SCM and TN fault areas induced by 2010 Jiashian earthquake.	144

List of Tables

Table 2.1 Quality classifications of the misfit and non-DC component in the released
AutoBATS MT catalog 27

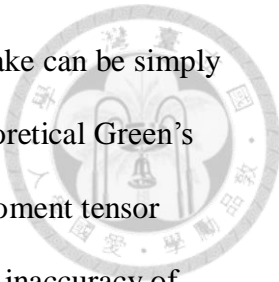


Chapter 1 Introduction



One of the key problems in seismology is the understanding of earthquake source processes. The kinematic source properties of an earthquake include the seismic moment, fault geometry, dislocation across the fault plane and the spatio-temporal distributions of the slip. When an earthquake occurred, besides the origin time and hypocenter location, the fundamental information of focal mechanism describing the fault geometry and dislocation across the fault plane is directly related to the response of the tectonic stress accumulation and release at the fault zone. Other than the focal mechanism, the rupture parameters including the rupture extent, speed, direction, duration and stress drop would control the behavior of the rupture front and reveal the physical properties of the fault itself. The estimated seismic moment and kinematic source rupture characteristics are the basis for further simulations of dynamic rupture scenario of an earthquake.

Understanding of the lithospheric deformation and tectonic stress regimes relies on continuous long-term observations of seismicity accompanied with a complete and reliable focal mechanism catalog. Routine determinations of focal mechanisms of global earthquakes with moment magnitude $M_w \geq 5.5$ or regional earthquakes in seismically vulnerable areas had been developed and performed by many state agencies or research institutes, such as Global Centroid Moment Tensor (Global CMT) project (Ekström et al., 2012), the United States Geological Survey (Spikin, 1986), GEOFON (Bormann, 2012), and GEOSCOPE (Vallée et al., 2011). In general, the earthquake focal mechanism can be represented by 5 or 6 independent components of the moment tensor (MT) associated with equivalent body-force couples acting on the



point-source location. Then the moment tensor solution of an earthquake can be simply obtained by a linear inversion of the observed waveform data and theoretical Green's functions. However, the challenges of retrieving stable and reliable moment tensor solutions reside in the intrinsic noises, imperfect coverage of data and inaccuracy of the Green's functions because of an inappropriate velocity model and mislocated centroid position used. In recent years, owing to the speedy progress of the computational capacities and data transmission of seismic networks, the real-time moment tensor inversion becomes possible to quickly gain the basic earthquake information for characterizing and responding to potential seismic hazards. Lee et al. (2014) developed a real-time moment tensor monitoring system (RMT) to automatically detect and simultaneously determine the epicenters and moment tensors of earthquakes in Taiwan, achieved at the expense of enormous computational resources. On the other hand, studies of seismogenic structures and seismotectonics demand a complete earthquake catalog that contains reliable and well-resolved moment tensor solutions. It is thus necessary to carry out a comprehensive exploration of several inversion settings, including the data, centroid location, velocity structure, and others that could lead to unstable or ambiguous inversion results but often were neglected in real-time solutions.

In the first part of my PhD thesis, I focus on establishing a new AutoBATS moment tensor inversion algorithm mainly for abundant regional seismicity in Taiwan. The goal of the study is to report both near real-time and stable MTs by taking into account the uncertainties of the inversion settings mentioned previously. Different from Lee et al. (2014) conducting a grid search of candidate earthquake locations using continuous longer-period broadband seismic data at a few BATS stations, I prefer to

take the best use of high-precision hypocenters to lower the mislocation effects on the MT solutions, which are determined by much denser CWBSN (Central Weather Bureau Seismograph Network). Instead of fixing the inversion settings for all the earthquakes that occurred in tectonically distinct settings, I would like to deliver the final moment tensor solutions together with the validation of the stability or reliability of the solutions by scanning four different Moho-depth models representative of the structures in the Taiwan region, three strategies of data selection, and three filtering frequency bands for all the used data.

In Chapter 2 , I present the new AutoBATS moment tensor inversion approach and its application to regional earthquakes in the Taiwan area. The reliability of the inversion scheme is verified by making the comparison of our newly obtained CMT catalog with the Global CMT solutions and the previous BATS catalog. Benefiting from this fast, reliable inversion scheme, I also update the regional moment tensor catalog for Taiwan earthquakes from 1996 to 2016. A new relation between moment magnitude (M_w) and local magnitude (M_L) is also examined based on our complete AutoBATS MT catalog. Figure 1.1 illustrates the flow chart of the newly developed AutoBATS moment tensor inversion method which has already been implemented in the real-time moment tensor report system of Data Management Center of IES (DMC-IES).

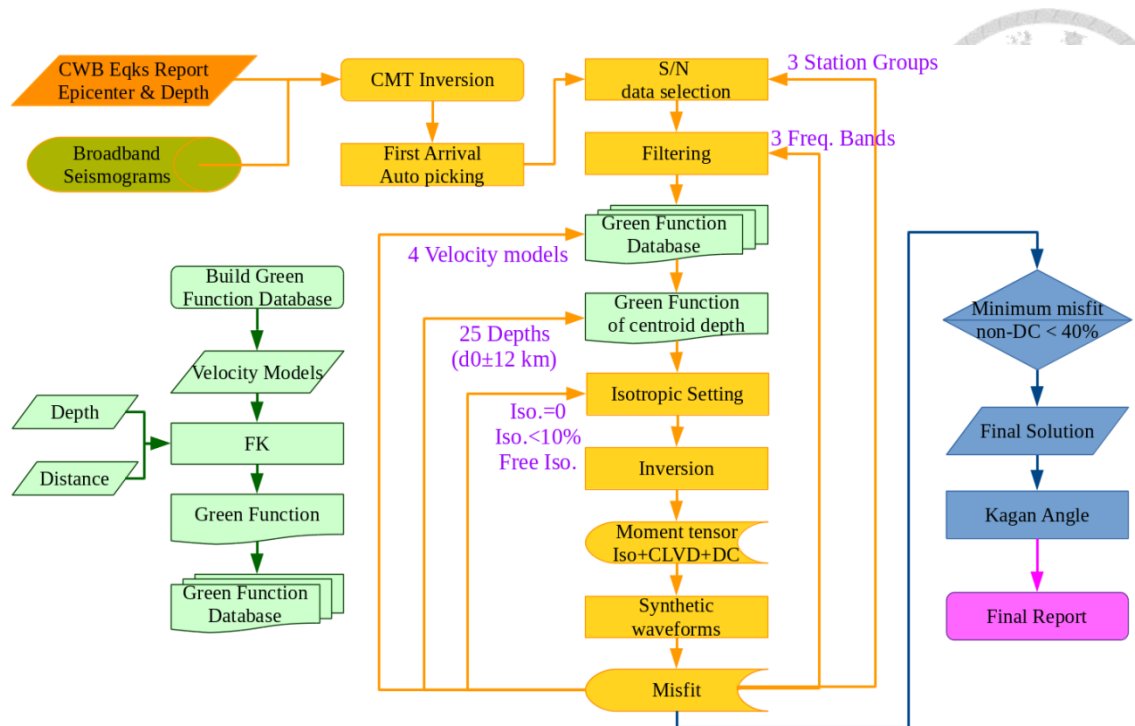


Figure 1.1 Flowchart of new real-time AutoBATS MT inversion scheme.

In general, a point-source approximation for major and great earthquakes is not sufficient to characterize the earthquake rupture propagating away on the finite-size fault plane. Therefore, the second part of the thesis is devoted to investigate the rupture characteristics of large earthquakes using high-density, high-frequency seismic array data.

Over the past several decades, numerous studies have employed different waveform inversion methods such as the multiple point source moment tensor inversion (Kao et al., 2000; Chen and Wen, 2015) and finite fault inversion (Antolik et al., 1996; Ji et al., 2002; Ye et al., 2012) to unravel the complex rupture history of many devastating earthquakes. These methods intend to recover the details of the rupture process by modeling a finite earthquake source as multiple subevents or discretized subfaults on the fault plane with variable source parameters. Although the

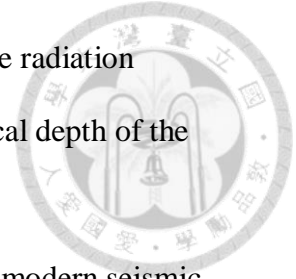
forward modelling theory that forms the foundation for the source inversion and the numerical inversion algorithm have been developed for years and become routinely applied to global large earthquakes, the finite-source inversion is known to be a notoriously ill-posed and underdetermined geophysical inverse problem (Ide, 2015) with too many unknown, poorly constrained model parameters involved in the inversion. As a result, it leads to highly non-unique results that strongly depend on the imposed a priori constraints such as the fault geometry, rupture speed, rise time, and etc. In addition, the relative complexity of high-frequency seismograms often affected by strong crustal velocity heterogeneity but not accounted properly in the waveform inversion limits the use of shorter period waveform data in the inversion.

Contributed by the worldwide deployment of dense seismic arrays such as USArray, ORFEUS (European network) and Hi-net (Japanese network), a high-resolution back projection (BP) technique alternative to the finite source waveform inversion have been widely applied to imaging the rupture propagation history of large earthquakes. In contrast to the inversion approach, the BP method requires neither the adjustment of a priori damping and smoothing parameters imposed on the inversion models nor the knowledge of the Green's functions, fault geometry, and rupture kinematics. It basically retrieves and stack coherent, high-frequency teleseismic seismic wavefield recorded across the array and project them back in time to track the positions of the strongest energy radiators among subfault grids throughout the rupture duration. As the onsets of the wavetrains used in the BP imaging are aligned properly, the errors in predicted travel times due to the heterogeneous velocity structure between the source and receiver are negligible. Ishii et al. (2005) first demonstrated the efficacy of the BP method to image a ~1300-km long rupture

propagating northward for the 2004 Sumatra-Andaman megathrust earthquake. Since then, it has become an effective approach to illuminate the rupture process for major earthquakes, such as the 2008 Sichuan earthquake, 2010 Chilean earthquake, and intermediate- and deep-focus earthquakes (Xu et al., 2009; Kiser et al., 2011b; Kiser and Ishii, 2012; Koper et al., 2012).

The classical BP approach, similar to the time-domain beamforming technique, shifts the traveltimes from a trial subfault grid relative to the hypocenter and stacks the moveout-corrected waveforms across the array to locate the energy radiation point associated with the maximum amplitude of the stacked waveforms integrated over certain time intervals. However, Ishii et al. (2007) noticed the spatial and temporal artifacts of the ghost stacks from the synthetic BP experiments that could cause the biased estimate of the time and location of the energy radiators. Such the ghost swimming artifact mainly arises from nonstationary seismic wavetrains within which the amplitudes are highly variable such that the weak arrivals in the beamforming image can be obscured by the movement of large-amplitude arrivals (Walker and Shearer, 2009; Xu et al., 2009; Meng et al., 2012a, 2012b). Meng et al. (2012b) developed a more viable BP method for non-stationary seismic waveforms based on the subspace-based method, the Multiple Signal Classification (MUSIC) algorithm. It has been demonstrated that the MUSIC BP technique provides superior resolution of the source images compared to that obtained with the classical time-domain BP method by adopting the “reference window” strategy to mitigate the artificial swimming effect efficaciously. Despite of the improvement of the BP method, it is still difficult to entirely suppress the smearing effect as illustrated in Figure 1.2b because of the intrinsic trade-off between travel time and distance. Therefore, most of the BP

imaging studies is restricted to 2D applications only, i.e. the candidate radiation sources confined in an assumed horizontal plane positioned at the focal depth of the earthquake.



On May 24, 2013, the largest deep earthquake ever recorded by modern seismic networks struck about 609 km beneath the Sea of Okhotsk. The focal mechanism from the Global CMT solution indicates this deep earthquake ruptured on either a sub-horizontal or sub-vertical fault plane. The finite-fault inversion reaches the inconclusive fault-plane orientation because the results of assuming either one of the nodal planes yield equal fits to the observed and synthetic waveforms (Ye et al., 2013). On the other hand, Chen et al. (2014) and Zhan et al. (2014) performed the multiple point source inversion and directivity analysis but obtained opposite conclusions on the actual fault plane. In Chapter 3, I attempt to develop a three-dimensional (3D) MUSIC BP method (Figure 1.2a) to resolve the ambiguity between the sub-vertical and sub-horizontal fault plane. To facilitate suppressing the smearing effects in the BP image and retrieve the stable rupture propagating process in 3D, I include the 3D BP images obtained by depth phases, pP, which travel upward to the surface and turning back to the distant stations and have the take-off angle different from the down-going direct P-wave. Since the smearing zone is parallel to the ray path from the source to the receiver array, combining the BP images obtained with different phases would help reduce the smearing area (Figure 1.2b).

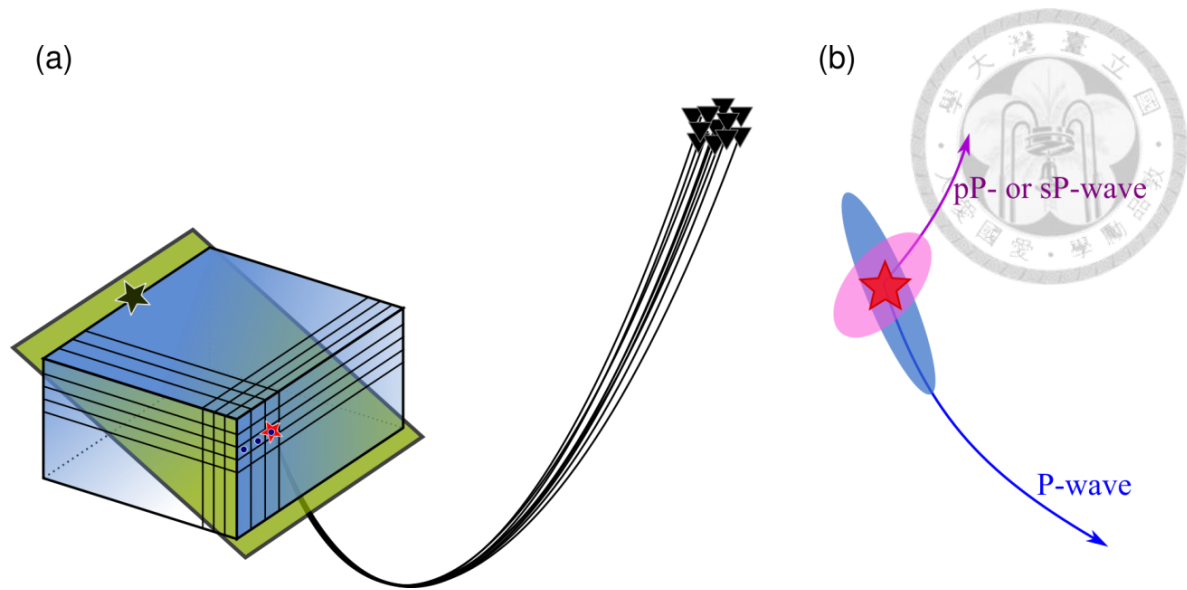


Figure 1.2 Illustration of a 3D back projection method and the smearing effects.

(a) Configuration of a 3D source volume discretized into grids of subfaults and the source-to-array geometry. (b) The elongated smearing zones expected to be seen in the BP images obtained with teleseismic P and depth phases.

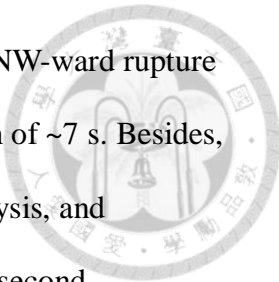
The combined P- and pP- wave 3D BP image of the 2013 Okhotsk earthquake seen from the North American (NA) seismic network shows a two-stage, anti-parallel rupture. The rupture propagates about 30-40 km northeastward during the first stage; it then jumps to greater depths and propagate at least 80 km in the reverse (S-ward) direction. The two anti-parallel ruptures are separated by a vertical distance of about 10-15 km. The average rupture speeds during the two stages are 3.0-3.3 and 4.25-4.80 km/s, respectively. The initial NE-ward rupture ends near the northern tip of the subducted Pacific slab that most likely has been heated up by the ambient warm mantle and asthenospheric flow around the slab edge (Peyton et al., 2001; Park et al., 2002; Davaille and Lees, 2004a). This may cause a relatively slower speed of the first NE-ward propagating rupture as well as prevent it from continuously growing.

In order to understand the resolution and limitations of the 3D MUSIC BP

technique, I perform a suite of synthetic experiments that mimic several possible rupture scenarios for the Okhotsk earthquake, including the rupture propagating vertically up- or down-ward, and horizontally perpendicular or parallel to the source-to-array azimuth. All of these synthetic results show the capability of the 3D P-wave BP MUSIC method to recover the hypothetical subevents. As expected, the combined P- and pP-waves BP images can help stabilize the resolved rupture image and locate the energy radiators with much smaller spatial uncertainties than that obtained with P waves only.

As the BP method mainly uses high-frequency teleseismic wavefield for source imaging, there are few applications to shallow earthquakes with magnitude less than 7 that could also produce destructive hazards. There are on average one to three earthquakes with magnitude greater than 6 that hit the Taiwan region every year, and some of them have caused severe damages and fatalities such as the 2016 Meinong earthquake and 2018 Hualien earthquake. To better understand the rupture kinematics of these earthquakes and corresponding seismogenic fault zones, I applied the MUSIC BP imaging and directivity analysis to unravel the rupture process of two strong earthquakes, the 2016 Meinong and 2010 Jiashian earthquakes that recently occurred nearby in southern Taiwan with comparable magnitudes and focal mechanisms.

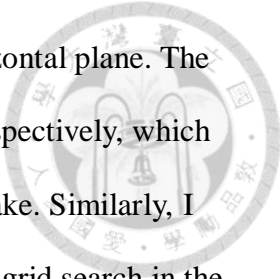
In Chapter 4, I present the first application of the MUSIC BP method to quantify the details of the rupture process for a moderate earthquake, the 2016 Mw 6.4 Meinong earthquake that severely hit southwestern Taiwan, a region with relatively low seismicity in the past and caused the deaths of over 100 people in the populated Tainan city about 30 km west of the epicenter. I use high-frequency P and depth-phase sP wavetrains from the dense European (EU) and Australian (AU) seismic networks. The



P-wave BP results either from the EU or AU array show a consistent NW-ward rupture extending about 16 km with a single-peak radiation burst and duration of ~7 s. Besides, through forward waveform modeling, the slowness-backazimuth analysis, and radiation pattern of depth-phase sP/pP amplitude ratios, I confirm the second displacement pulse that begins ~8 s after the onset of the first P-wave pulse mainly consists of the depth-phase pP and sP energy. Therefore, I conduct the same BP imaging using the aligned sP wavetrains. The integrated P- and sP-wave BP images resulting from the EU and AU array data are overall in accordance with each other showing a unilateral subhorizontal rupture propagating northwest. To verify the kinematic rupture properties derived from the BP imaging, I also employ the directivity analysis assuming a kinematic unilateral rupture model using global broadband displacement waveforms.

As demonstrated by the study of the Meinong earthquake, the MUSIC BP technique has shown great success in unraveling the rupture behavior of moderate-size earthquakes generally with relatively short rupture length about tens of kilometers and source duration about a few seconds. Therefore, I attempt to apply the same approach to studying the rupture process of the 2010 Jiashian earthquake which shares several seismological similarities with the 2016 Meinong earthquake, including the nearby epicenter, similar focal mechanism and comparable seismic moment. The results are summarized in Chapter 5.

According to the integrated P- and sP-wave BP images obtained with the EU and AU array data, I found the Jiashian earthquake predominantly ruptured toward northwest as the Meinong earthquake did. However, unlike the Meinong event with a nearly horizontal rupture, the Jiashian earthquake ruptured obliquely in both the



along-strike and updip direction, which is about $16\text{-}20^\circ$ from the horizontal plane. The estimated rupture length and duration is about 10-11 km and 4-5 s, respectively, which give the average rupture speed similar to that of the Meinong earthquake. Similarly, I conduct the directivity analysis to validate our BP results. I perform a grid search in the space of the rupture length and velocity, and the strike and dip of the rupture propagation direction and find the optimal solution that yields a global minimum misfit of observed and predicted apparent rupture durations. The F-test shows that the additional testing variables, the rupture strike and dip, are statistically significant to improve the fit between the observed and predicted source time duration.

Motivated by the similarity of the seismic moment tensor and rupture properties between the Jiashian and Meinong earthquake as well as the spatial distributions of the mainshock and aftershock sequences, I proposed a blind subsurface fault striking NW and dipping to NE (hereafter referred as to the JSMN fault) is the causative fault responsible for the occurrence of the two earthquakes. Besides, I investigate the temporal b-value variations and static stress changes induced by the two events. By compiling all the observations and analyzing results, I propose the Jiashian and Meinong earthquakes are the doublet events which have occurred as a result of failure of the two strong asperities on the JSMN fault. After continuous stress buildup on the fault for at least 45 years mainly exerted by the plate convergence, the accumulated stress exceeding the strength of the smaller asperity on the deeper eastern end of the fault released and initiated the rupture of the Jiashian earthquake. The static Coulomb stress transfer triggered by the slip of the Jiashian event suggests an additional stress increase in the vicinity of the shallower western asperity. With additional tectonic stress loading for six years, the failure of the shallower and stronger asperity took place

and initiated the rupture of the Meinong earthquake.



Chapter 2 A new automatic full-waveform regional moment tensor inversion algorithm and its applications in the Taiwan Area



Original published in Jian, P.-R., T.-L. Tseng, W.-T. Liang, and P.-H. Huang (2018). A New Automatic Full-Waveform Regional Moment Tensor Inversion Algorithm and Its Applications in the Taiwan Area, *Bull. Seismol. Soc. Am.*

2.1 Abstract

A new algorithm is developed in this study to automatically determine regional moment tensor (MT) and its centroid depth with real-time waveforms in 2-4 minutes after the Central Weather Bureau (CWB) issues an earthquake notice. The program selects 3-7 BATS (Broadband Array for Taiwan Seismology) stations under three criteria: best azimuthal distribution, highest signal-to-noise ratio, and shortest distances. It then inverts MT solutions in parallel with various settings including Moho depth of velocity models, frequency bands, and isotropic constraints. The optimal solution is determined by searching for the best waveform-fit with an acceptable non-double-couple component from the results of combinations of these inversion settings. Our new rapid MT report system greatly reduces computational resources and avoids human judgments. By applying this full-scanning approach on BATS (named AutoBATS), we re-determine the MTs for over 3000 regional earthquakes from 1996 to 2016 to provide the most up-to-date MT catalog for the Taiwan area. The AutoBATS MTs are overall consistent with the Global Centroid Moment Tensors with a mean difference in Kagan angle of $22.0 \pm 16.6^\circ$ and M_w of -0.08 ± 0.10 . Those focal mechanisms better illuminate the tectonic structures owing to the much improved

resolving ability for shallow (<10 km) and deep (>140 km) earthquakes. With the new regional MT catalog, we refine the relationship between moment and local magnitudes:

$M_W = 0.87 M_L + 0.23$ for the Taiwan region.



2.2 Introduction

Fast determination of source parameters of regional large earthquakes are crucial for government agencies to properly and quickly respond to cases of serious seismic hazards. Reliable estimates of the seismic moment and focal mechanism are particularly important because these two parameters are directly related to the extent and severity of the seismic damage caused by earthquakes. For long-term evaluation of the seismic hazard of seismically active regions, a robust regional moment tensor catalog is the most fundamental information for advanced studies like regional tectonics, strain-stress monitoring of the lithosphere, and strong motion simulation for hazard evaluations.

For moderate-to-large earthquakes with M_W above ~5.5 worldwide, moment tensor (MT) solutions are available freely from agencies/organizations such as the Global Centroid Moment Tensor (CMT) project (Ekström et al., 2012), the United States Geological Survey (Spikin, 1986), GEOFON (Bormann, 2012), and GEOSCOPE (Vallée et al., 2011). In theory, both the centroid moment tensor (CMT) and point source parameters (centroid position and origin time) are determined by inverting very long-period seismic waveforms recorded at tele-seismic distances (Dziewonski et al., 1981). Over the past two decades, regional MT inversion has also

become a routine process to release MT or CMT local catalogs for small-to-moderate earthquakes since regional seismic networks have built up in many seismically active areas (Dreger and Helmberger, 1993; Sileny et al., 1996; Kao et al., 1998a; Fukuyama and Dreger, 2000; Braunmiller et al., 2002; Kubo et al., 2002; Pondrelli et al., 2002; Stich et al., 2003; Bernardi et al., 2004; Ito et al., 2006; Cambaz and Mutlu, 2016).

With increasingly dense regional networks developing worldwide, near real-time automatic MT inversion systems are becoming possible due to the large improvements in data transmission and computational capability in the last decade (Bernardi et al., 2004; Rueda and Mezcua, 2005; Ito et al., 2006; Nakano et al., 2008; Scognamiglio et al., 2009; Lee et al., 2011). On a regional scale, genuine CMT solutions can be inverted based on local long-period waveforms with the centroid position often obtained by grid-search approaches (Ito et al., 2006; Lee et al., 2014).

Taiwan, an extremely seismically active area in the western Pacific, was one of the earliest countries to have a regional MT reporting system. Kao et al. (1998a) established the moment tensor inversion algorithm using long-period waveforms recorded by the local network BATS (Broadband Array in Taiwan for Seismology) operating under the Institute of Earth Sciences (IES) of Academia Sinica, Taiwan. Since 1995, the Data Management Center of IES has routinely inverted and published over 2000 moment tensor solutions for regional earthquakes with M_L above 4.0. The MTs released by IES BATS (so-called BATS CMT) have been widely adopted by research communities for further investigations in the Taiwan area on earthquake rupture characteristics (Huang et al., 2008; Lee et al., 2008), seismotectonic studies (Kao et al., 1998a; Kao and Jian, 1999, 2001; Kao and Chen, 2000; Lallemand et al., 2001; Angelier et al., 2009; Chen et al., 2009; Huang and Lin, 2017), seismic moment

magnitudes, and seismic hazard evaluations e.g., (Chen et al., 2008).

To achieve fast estimates of MTs for Taiwan earthquakes, IES BATS currently performs moment tensor inversion with a set of fixed parameters after receiving alarms issued by the Central Weather Bureau (CWB) of Taiwan. However, data selection and quality examination on inversion results are still performed manually. Usually, the MT reports can be provided within a few hours. From a different perspective, Lee et al. (2014) developed a real-time MT system that reports the centroid hypocenter location with a 10-km spatial resolution and the corresponding MT within 2 minutes by calculating MTs of a continuous data stream recurrently recorded by a fixed subset of BATS stations. The drawback is that this state-of-the-art system requires significant computational resources to approach a truly real-time solution that is independent of the CWB report.

No matter which frameworks are chosen, it is unquestionable that the reliability of the MT solution requires the inversion itself to be performed with suitable parameters and settings. In particular, lateral changes in velocity structure are apparent in Taiwan e.g. (Rau and Wu, 1995; Huang et al., 2014), and a fixed one-dimensional (1D) model cannot be perfect for each event analyzed. The MT solutions may be improved by adjusting 1D velocity models for each event-station pair, selecting alternative stations, and trying different frequency bands for each station. In the past, for BATS MT, further fine-tuning was also manually processed (Kao et al., 2002; Liang et al., 2004). However, this traditional approach is too tedious and inefficient to satisfy current demand, leading to the desire for a compromise. In addition, it is important to explore how large the variances can be if the solutions are inverted with different parameters or settings.



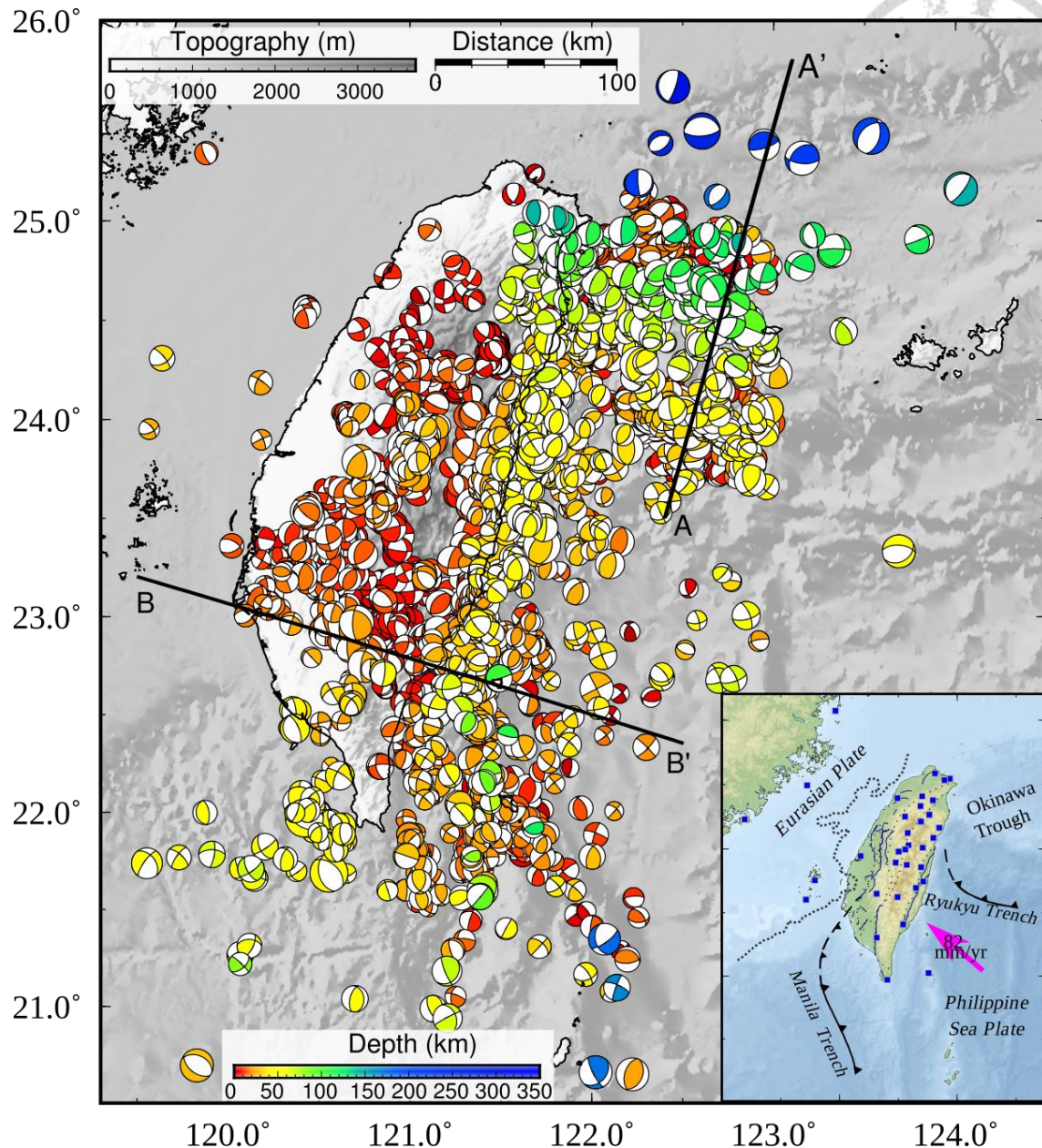
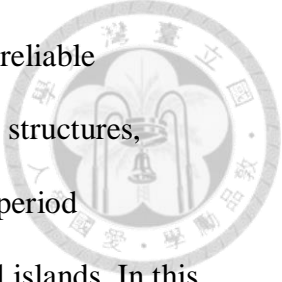


Figure 2.1 AutoBATS MT solutions for earthquakes from May 1996 to April 2016.

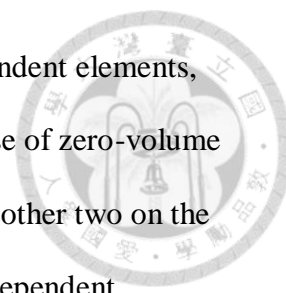
The beach ball colors represent the centroid depth determined by MT inversion. The beach ball size is scaled with the moment magnitude. The lower right inset shows the tectonic setting in the Taiwan area. The pink thick arrow indicates the direction of the converging Philippine Sea plate relative to the Eurasian plate. BATS broadband stations are denoted by blue squares (excluding stations in the South China Sea). The dotted line delineates the 2000 m isopach of Cenozoic sediments.



In Taiwan, reporting MT solutions while satisfying both fast and reliable obligations is a great challenge due to strong heterogeneity in velocity structures, possible mislocation of off-island earthquakes, and unavoidable long-period background noises for those stations located close to shore or on small islands. In this study, we develop a new automatic approach to achieve the goal of retrieving highly reliable regional MT solutions in near real-time for small-to-moderate earthquakes in Taiwan. We are not attempting to fully determine the centroid hypocenters. Instead, we take advantage of the overall efficiently and precisely determined epicenter origins from CWB. Therefore, only the centroid depth and MT of the events are constrained in our MT report. To reduce the manual efforts on searching suitable inversion settings for each earthquake, we determine the final MT solution among the inversion results by systematically exploring various key settings or parameters, including different frequency bands, station-selection strategies, and 1D velocity models. Then, we can demonstrate the variability of the solutions and discuss which factors are more influential on the MTs for each event. Finally, we provide 20 years of well-determined focal mechanisms for the Taiwan region that exhibit details of tectonic features.

2.3 Moment tensor inversion and regional waveform data

Linear moment tensor inversion is based upon the representation theorems in which the observed displacement waveforms are the combined effects of the earthquake source and Green's functions (Aki and Richards, 1980). In principle, Green's functions contain propagation effects in a layered Earth's structure from



earthquake to station, whereas a moment tensor, a matrix of 6 independent elements, gives the equivalent radiation of faulting on a point source. In the case of zero-volume change, the third isotropic element is compensated by the sum of the other two on the diagonal of the matrix (Jost and Herrmann, 1989), leading to five independent variables to solve. With a properly derived velocity model and quality waveforms, the moment tensor can be directly inverted by minimizing the overall differences between the observed and simulated three-component waveforms in a least squares sense (Stump and Johnson, 1977). The fault parameters are then derived from the double-couple (DC) component of the moment tensor.

In the current CMT inversion algorithm of BATS, Kao et al. (1998a) used a reflectivity-based method of Yao and Harkrider (1983) to calculate Green's functions. In this study, we employ the frequency-wavenumber integration technique as an alternative which is capable of calculating both static and dynamic surface displacement (Zhu and Rivera, 2002). For the goodness of waveform fitting in the inversion, we principally follow the definition of a cross-correlated, similarity-sensitive misfit function (introduced by (Mellman et al., 1975; Kao et al., 1998a), which emphasizes the coherence between the observed and synthetic waveforms more than the absolute amplitudes (Wallace et al., 1981). To further account for the differences in relative amplitude, we adopt the misfit equation for each component as follows: $E = 1 - \frac{\min(f_i(t)_{max}, g_i(t)_{max})}{\max(f_i(t)_{max}, g_i(t)_{max})} \frac{\int f_i(t) * g_i(t) dt}{\sqrt{\int f_i(t)^2 dt \int g_i(t)^2 dt}}$, where $f_i(t)$ and $g_i(t)$ are observed and synthetic waveforms in displacement, respectively; $f_i(t)_{max}$ and $g_i(t)_{max}$ are the maximum amplitude of observation and synthetic waveforms, respectively (Kao and Jian, 1999; Huang et al., 2017).

In this study, all broadband waveforms come from BATS, a local network currently consisting of a total of 36 broadband stations in the Taiwan area (Figure 2.1, inset) who have provided high-quality continuous seismic data since 1996 (Institute of Earth Sciences, Academia Sinica, Taiwan, 1996). The initial information of earthquakes, including epicenter, focal depth, and origin time, are taken from CWB. To reduce the effects of mislocation errors on inversion results, we only use well-determined hypocenters of earthquakes that are verified manually with the quality-checked data by CWB. The centroid depth of the MT solution is estimated together with the MT inversion by a grid-search approach as in many CMT studies (Dreger and Helmberger, 1993; Zhu and Helmberger, 1996), as well as the previous BATS inversion (Kao et al., 1998a). Here, we perform MT inversion at a 1 km interval for a depth range ± 12 km with respect to the initial focal depth, and the centroid depth is determined from the smallest misfit among the 25 solutions.

Although the moment tensor inversion itself is a linearized problem through Green's functions and seismic displacement waveforms, non-uniqueness or large variances of inversion results are common because of non-linear effects/bias from the different 1D velocity model assumptions for Green's functions, the frequency band used for data processing, and the method of selecting stations. Therefore, our approach is to retrieve stable MT solutions by systematically scanning the solutions from all combinations of station-choosing strategies, varied velocity models, and different frequency bands. The scanning parameters and setting criteria are introduced in the next section.

2.4 Automatic determination of the optimal MT solution with thoroughly scanned parameters



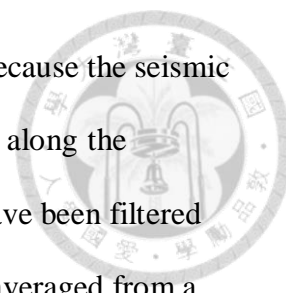
To efficiently achieve stable and reliable results for moment tensor inversion, the first important and necessary step is to avoid manual data selection before the inversion. In this study, we only consider stations whose average signal-to-noise (S/N) ratios of three-component waveforms are greater than 2.0 in the desired frequency band (0.01~0.09 Hz). We take 150 s time windows before and after the P arrival to estimate the spectra and calculate average point-by-point S/N with 5-point moving time-window smoothing. We exclude stations with epicentral distances smaller than 30 km to reduce the mislocation effect. Since many studies typically use three or more three-component broadband stations for regional moment tensor inversion (Dreger and Helmberger, 1993; Zhu and Helmberger, 1996; Kubo et al., 2002; Pondrelli et al., 2002; Rueda and Mezcua, 2005; Clinton et al., 2006; Ristau, 2008), we selected a minimum of 3 to a maximum of 7 S/N-qualified stations to start the inversion based on three different criteria: (1) the best azimuthal coverage, (2) the highest S/N, and (3) the shortest epicentral distances. For earthquakes inside a homogeneous network, the most logical and easiest approach for criterion (1) is to divide stations evenly into 8 half quadrants according to azimuth and pick at least one S/N-qualified station in each sector. Unfortunately, this simple method is not appropriate for Taiwan due to restricted azimuthal coverage in most cases since the majority of earthquakes occur near the coast and eastern offshore region. To accommodate this natural condition, we retain the stations at the minimum and maximum azimuth, and use these two azimuths as boundaries to divide the remaining stations into three even sectors. We then pick one

to three stations randomly in each sector so that criterion (1) is fulfilled. For criteria (2) and (3), stations are chosen according solely to their mean S/N and epicentral distances.

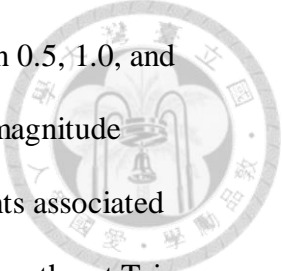
It is normally expected that better azimuthal coverage improves reliability of MT solutions. The problem of selecting stations solely based on azimuthal coverage in the Taiwan area is that the selected stations near the coast or on small islands are occasionally contaminated by long-period ambient noises even though the average S/N might be slightly better than threshold value. Criteria (2) and (3) not only provide other possible choices of stations, but the consistencies among resulting solutions can further ensure the MT solutions are insignificantly biased by those stations with notable noises near the shore or at far distances. Note that the quality (S/N) of regional waveforms is usually site-dependent and unrelated to epicentral distances; therefore, the three different criteria are complementary.

Once stations are selected, we perform the inversions with different parameter settings. To accommodate the velocity variations in the Taiwan region and to improve the stability of inversion with the longest possible periods, we apply three different frequency bands and four velocity models for all selected stations in the inversions. For each earthquake, three consecutive passbands are applied from the followings 5 standard frequency ranges: 0.01~0.04 Hz (25~100 s), 0.02~0.06 Hz (16~50 s), 0.03~0.08 Hz (12~33 s), 0.04~0.09 Hz (10~25 s), and 0.05~0.15 Hz (7~20 s). The choice depends on the local magnitude reported by CWB. For earthquakes with a local magnitude above 5, within 3.5 to 5, and below 3.5, the lowest corner frequency starts from 0.01, 0.02, and 0.03 Hz, respectively.

For the velocity models, it is unrealistic to create a high-resolution 1D velocity



model which reflects all the path effects for each event-station pair because the seismic waves usually travel through distinct structures in Taiwan (especially along the east-west direction). Considering the waveforms for MT inversion have been filtered for relatively long periods, we start with a simple three-layer model averaged from a 3D tomography model of Taiwan (Rau and Wu, 1995) as a reference. This model, with Moho depth set at 40 km, has been used for 20 years by the current BATS MT inversion, and simulations in waveforms are reasonably good (Kao et al., 1998a, 2002; Kao and Jian, 1999; Kao and Chen, 2000; Liang et al., 2004). We then further consider the effect of regional variations of Moho depths from 20 to 50 km under different geologic units that were revealed by receiver-function and tomography studies (Wang et al., 2010; Kuo-Chen et al., 2012; Huang et al., 2014). Since the dominant periods used are more sensitive to structure deeper than 20 km relative to the shallow crust within 10 km (Dahlen and Tromp, 1998), we create a series of velocity models by changing the Moho at 5 different depths ranging from 25 to 45 km with intervals of 5 km. Each candidate potentially represents the average/pseudo structure under the paths covered by the event. Moho depths between 30 and 45 km are used for inland earthquakes, while a shallower range from 25 to 40 km is considered for offshore cases. After carefully examining the inversion results, we confirmed that trying different Moho-depth models can effectively reduce misfit and the compensated linear vector dipole (CLVD) component. Following Dreger (2003), we allow Green's functions to shift by ± 2 seconds for each station to lower the misfit due to the possible mislocation and the imperfectness of the velocity model. For fast moment tensor inversion, the Green's functions of each 1D model are pre-calculated and stored in the databases with a 1 km grid size in distance and focal depth.



For a more realistic simulation of synthetic waveforms, we assign 0.5, 1.0, and 2.0 seconds as duration of source time function for earthquakes with magnitude smaller than 4, between 4 and 6, and above 6, respectively. Since events associated with volcanic activities have been reported in the Okinawa Trough in northeast Taiwan (Lin et al., 2007), our newly developed MT inversion method includes three different isotropic conditions: free-constrained, limited ($\leq 10\%$), and zero isotropic components. For the free-constrained or zero isotropic component, we simply invert either 6 or 5 independent elements of the moment tensor. For limited isotropic constrained inversion, we compose a weighting vector inside the kernel matrix, in which the sum of three isotropic elements equals 0, as shown in following

form: $\begin{bmatrix} d \\ 0 \end{bmatrix} = \begin{pmatrix} G \\ w & w & w & 0 & 0 & 0 \end{pmatrix} (m_{11} \ m_{22} \ m_{33} \ \cdots)^T$. The inversion is performed iteratively with an initial weighting factor (w) 1, and then adjusted by increments of 1 until the isotropic component of the moment tensor is reduced to 10% or lower.

The AutoBATS MT inversion starts with auto picking of the first P arrivals for each station (Allen, 1978). The system then performs all inversion processes concurrently with different combinations of settings/parameters mentioned above using the GNU parallel tool (Tange, 2011). Among those inversion results, the one with the minimum misfit and applicable non-double-couple (non-DC) component is reported as the final/preferred MT solution (see Table 2.1 for classifications). Generally, we expect both the CLVD and isotropic components of the tensor to be low for small- to moderate-size tectonic earthquakes associated with shear faulting and relatively uncomplicated ruptures. According to Kagan (2002), an additional non-DC component can be introduced due to the data contamination of background noises, an over

simplified velocity model, or the mislocation of earthquakes; therefore, we set up rigorous criteria for non-DC. Only solutions with an isotropic component $\leq 20\%$, CLVD $\leq 30\%$, and non-DC $\leq 40\%$ are accepted for reporting. For each resultant MT solution, we assign a quality factor (QF) according to the waveform misfit and non-DC component (Table 1). Although the MT solutions with limited non-DC components were reported, the AutoBATS parameter-scanning algorithm is capable of searching for the non-tectonic seismic events if the non-DC criterion is removed.

In this study, we applied the procedure of AutoBATS MT inversion to determine a total of 3058 solutions for earthquakes with a M_L greater than 3.5 between May 1996 and April 2016 in the Taiwan region (Figure 2.1). Figure 2.2 and Figure 2.3 demonstrate how well the focal mechanisms are constrained by the AutoBATS inversion for a shallow earthquake ($M_L=4.9$) inland and another intermediate-depth event ($M_L=6.7$) offshore, respectively. In each event, the best solution of focal mechanism and the corresponding stations used are highlighted (Figure 2.2a, and Figure 2.3a). Inversion results from different combined settings (such as Moho depth of models, frequency bands, and centroid depths) are directly compared in terms of their misfits and non-DC components. For the 2015/05/25 inland earthquake, the distribution of misfit and non-DC contours shows that filtering at a lower frequency band (0.02~0.06 Hz) and a model with a deeper Moho of 40 km yields the smallest misfit for this normal faulting event with a centroid depth of 10 km (Figure 2.2b). Most inverted tensors are close to pure normal-faulting as indicated by the triangle diagram of focal mechanism (Figure 2.2d). The triangle diagram, developed by Frohlich (2001), is an effective way to demonstrate the fault-type partitioning and the frequency distribution of the focal mechanisms from the inversion results of all tested parameters.

Figure 2.2e further gives the distribution of the Kagan angles (Kagan, 2003), K-angle hereafter, the smallest 3D rotation angle measured between the best focal mechanism and other solutions. It can be shown that the differences between solutions are more sensitive to the focal depths than the frequency band or velocity model for this earthquake. The overall small misfit is also evident by the excellent agreements between the observed and synthetic waveforms calculated from the final solutions (Figure 2.2c). The uncertainties of moment magnitude, focal depth, and CLVD component are assessed through the standard deviation (S.D.) from all scanned resultant inversions. This example reveals that the non-DC component of the low misfit (<0.4) solutions can vary significantly with Moho depth and frequency band (Figure 2.2b). The variability of solutions also confirms the necessity of scanning various settings while performing a regional moment tensor inversion.

Table 2.1 Quality classifications of the misfit and non-DC component in the released AutoBATS MT catalog

Misfit	Category	Non-DC Comp. (%)	Class
<0.3	A	<10	1
$0.3\sim0.5$	B	$10\sim20$	2
$0.5\sim0.7$	C	$20\sim30$	3
$>0.7^*$	D	$>30^*$	4

* Program rejects solutions with non-DC component larger than 40% or misfit greater than 0.75.

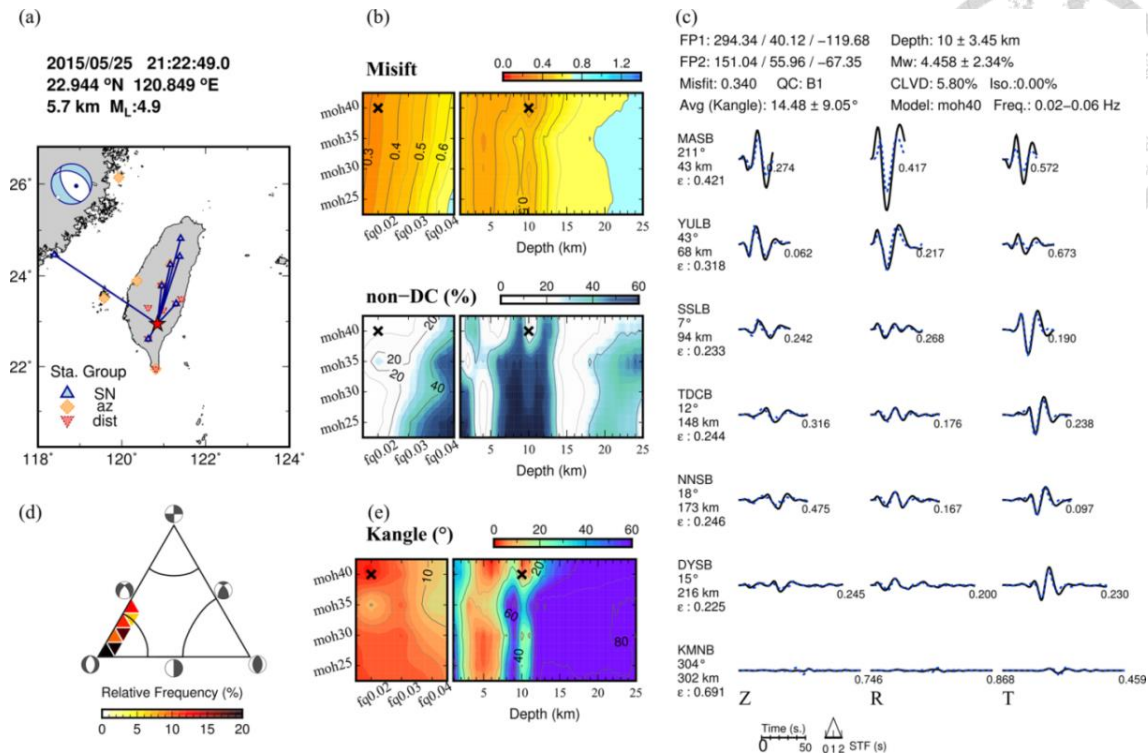


Figure 2.2 MT inversion results for the earthquake on 2015/05/25 ($M_L=4.9$) in southern Taiwan. (a) Map showing earthquake epicenter (star) and distribution of 3 station groups (dist: shortest distance, az: best azimuthal coverage, SN: highest S/N) considered in the inversion scanning scheme. The stations used for the final/best solution are highlighted with bolded outlines. The final MT solution is shown in the upper left corner. The original time, epicenter, focal depth and local magnitude reported by CWB are listed at the top. (b) Contour images of misfit (Top) and non-DC (Bottom) for four varied Moho-depth velocity models, three different frequency bands, and 25 scanned focal depths. The crosses mark the best suited combination of parameters used to produce the final MT solution. (c) The fitness between observations (solid black lines) and synthetic waveforms (blue dash lines) corresponding to the best solution. For each station, the name of stations, azimuth angles, epicentral distances, and the average misfits of three component waveforms are indicated on the left. The number beside each seismogram is the individual misfit. (d) The distribution of appearance (in percentage) on the focal mechanism triangular diagram from all inversion results with different inversion settings. The symbols are colored with the appearance frequency. (e) Contour images of the K-angle measured from the 3D rotation angle between the final focal mechanism and all other MT solutions. The explanations of axes and symbols are the same as in Figure 2.2b.

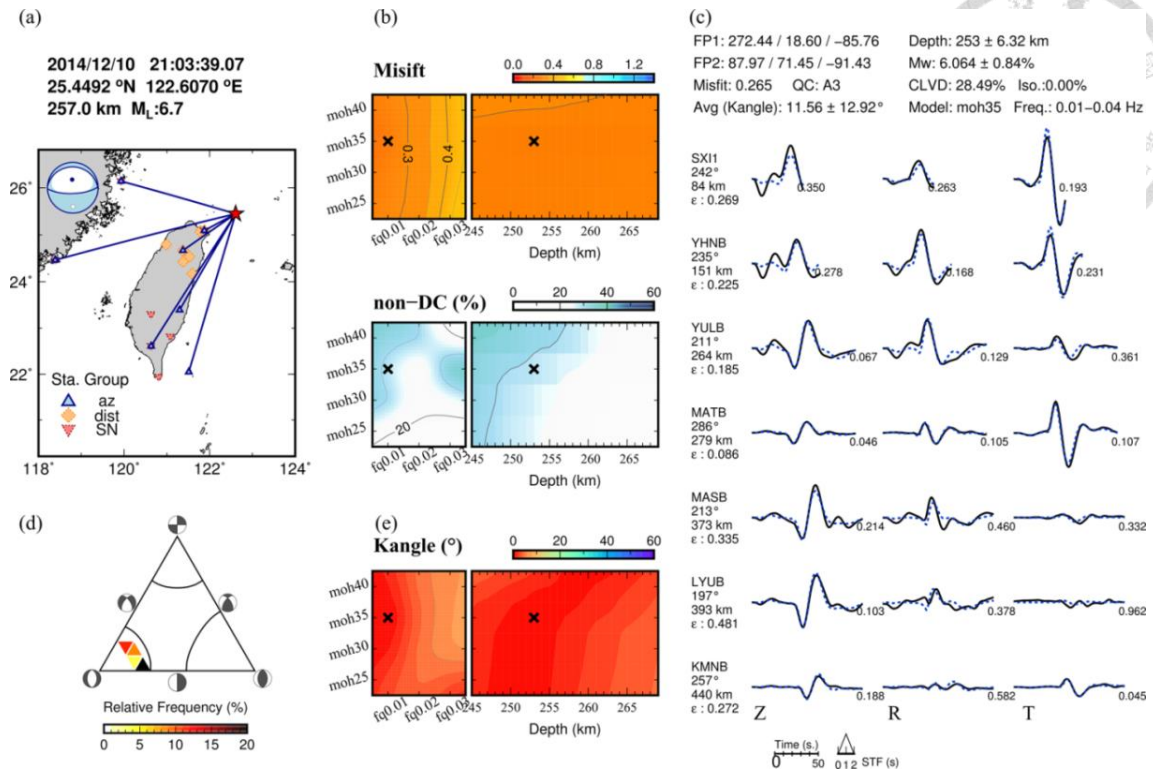
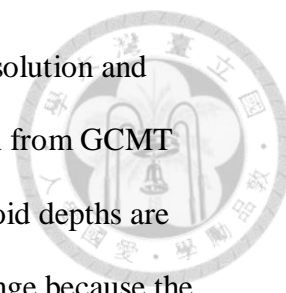


Figure 2.3 MT inversion results for the intermediate-depth earthquake on 2014/12/10 ($M_L=6.7$) beneath the Ryukyu subduction zone.

The layout is the same as in Figure 2.2

Figure 2.3 shows the result of an intermediate depth earthquake occurring in offshore Northeast Taiwan on 2014/12/10. This earthquake was excluded in the previous BATS MT catalog because the original depth reported by CWB exceeds the BATS MT calculation range. Our new AutoBATS inversion can provide more constraints to the subduction zone earthquakes. Unlike the shallow event shown in Figure 2, the misfit, non-DC component, and K-angle of this mid-focus offshore earthquake are relatively insensitive to velocity model, frequency bands, and focal depth, resulting in highly coherent focal mechanisms and less varied misfits (Figure 2.3). Because this earthquake is large in magnitude (M_w 6.0), filtering at a lower frequency band produces a smaller misfit as expected (Figure 2.3d). Although the



azimuthal coverage of stations is restricted in one quadrant, our MT solution and centroid depth estimation are both highly consistent with the solution from GCMT (Ekström et al., 2012). For intermediate depth earthquakes, the centroid depths are sometimes less well resolvable within our ± 12 km scanning depth range because the misfit values are comparably small (Figure 2.3b). In addition to a reliable initial location from the CWB catalog, it is always recommended to consider other independent constraints, such as the depth phases pP and sP observed at teleseismic distance, to further confirm the actual depth of the event.

The AutoBATS MT inversion scheme shows superior capability for determining focal mechanisms. This study successfully resolved 3058 MTs (about 56%) out of 5500 CWB-reported earthquakes with acceptable data quality. Moreover, among these MT solutions, 87% have misfit smaller than 0.7 (above Category C in quality) and 99% have non-DC below 30% (above Class 4). Some resolved earthquakes are as small as MW 3.0 (Figure 2.4a). With the new AutoBATS catalog, we can further investigate whether the mean misfit, value of the CLVD component, and consistency of MT solutions (as described by the K-angle) have any relation with earthquake magnitudes. Figure 2.4b shows that the average misfit decreases from 0.7 to 0.4 as the moment magnitude increases from 3.5 to 5.6. This can be simply explained by the higher data quality against background noise for larger events. For earthquakes with $M_w \geq 5.6$, the average misfit increases again. This phenomenon may relate to the complexity of earthquake rupture, which often involves source directivity and multiple fault segments with different slip vectors, particularly in large events. Waveforms excited by complex source ruptures cannot be well simulated by a single focal mechanism, and so larger misfits may exist. In this case, the results of MT inversion

represent the overall effect of averaged rupture for the earthquakes. Like the features observed for misfit, the mean K-angle shows almost exactly the same trend; the values first decrease and then increase with magnitude (Figure 2.4b). The similarity between mean misfit and K-angle suggests that the stability and consistency of MT inversion results are mainly affected by the waveform quality for small-medium earthquakes and rupture complexity for larger earthquakes.

Contrarily, the mean CLVD appear to be a constant, independent of the magnitude of events (see Figure 2.4c). This phenomenon agrees with Kagan (2002), who concluded that CLVDs are usually caused by artificial effects, except for well-examined events. As already demonstrated in Figure 2.2b, the CLVD component of a shallow earthquake is easily affected by different inversion settings. For Taiwan earthquakes, we believe that the strong heterogeneity in tectonic structures and the long-period ambient noises for some stations are mostly responsible for the observed high CLVDs. The lower limit of the average K-angle or CLVD (defined by mean value minus a S.D.) for each M_w bin represents those earthquakes having overall consistent MTs or small CLVDs among all scanning settings. On the other hand, the upper bound (mean value plus a S.D.) reveals that the MT solutions are affected tremendously by different inversion settings. Again, the deviations (error bars) of the average K-angle and CLVD highlight the importance and necessity of probing the best solutions through comprehensive scanning on different inversion settings or parameters.

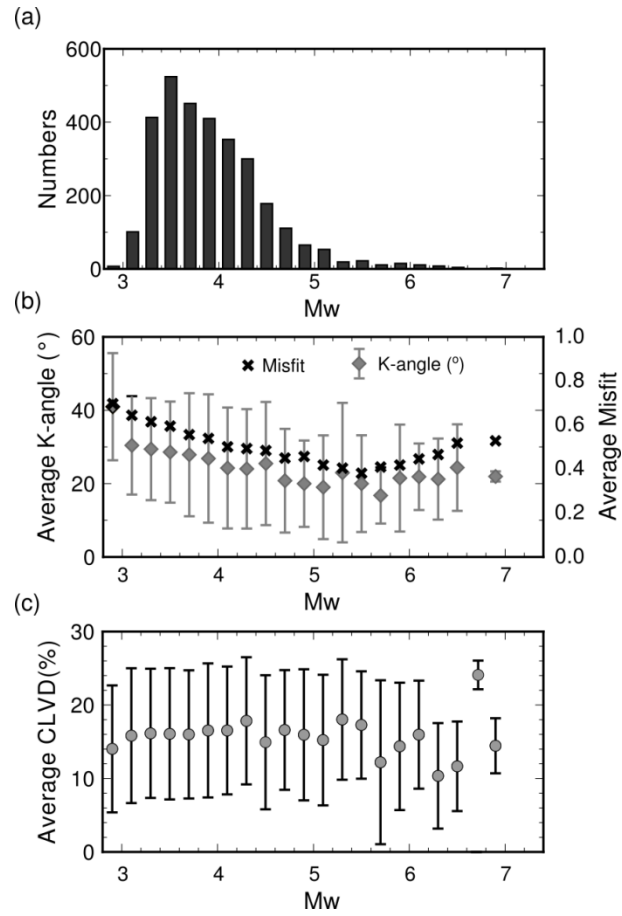
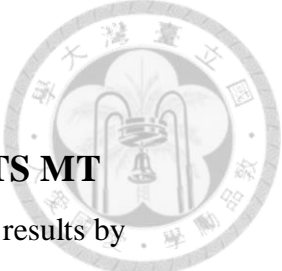


Figure 2.4 Number of events, Average K-angle and CLVD component with respect to M_w .

(a) Histogram showing the numbers of earthquakes with respect to M_w (bin size = 0.2). (b) The relation of average misfit and K-angle with respect to M_w based on all AutoBATS MT solutions. (c) The relation of average CLVD with respect to M_w . Both error bars in (b) and (c) correspond to a standard deviation.

2.5 Comparisons and discussions

2.5.1 Consistency between Global CMT and AutoBATS MT



It is indispensable to evaluate the stability of our AutoBATS MT results by comparing the solutions with those in the Global CMT catalog, which is considered the most complete and reliable CMT database for earthquakes with magnitude above ~5.5 since 1976 (Dziewonski et al., 1981; Ekström et al., 2012). We focus on the consistencies in MTs and centroid depths. Since the CMT inversion results can be significantly influenced by mislocation and focal depth, we consider the focal mechanisms only for the matched event (based on original time) that are reasonably close to each other. We first evaluate how close is close enough for an event pair. The histogram in Figure 2.5a indicates that the differences in epicenter locations for most matched event-pairs are smaller than 20 km, and the mean difference measured from all 200 pairs is 15.7 ± 12.9 km. Figure 2.5b further confirms that the centroid depths reported in AutoBATS and GCMT are consistent with each other when their locations are close. The discrepancy in centroid depth ($\Delta\text{depth} = d_{\text{ABATS}} - d_{\text{GCMT}}$) and their standard deviation, however, tend to grow much larger when the epicenter locations differ by 30+ km. Therefore, we use 28.6 km (the mean distance plus one S.D.) as the distance cutoff, and compare the MT solutions for pairs with an epicenter difference shorter than this value. There are 176 event pairs satisfying this criterion, and their MT solutions are further compared (Figure 2.5c and Figure 2.6).

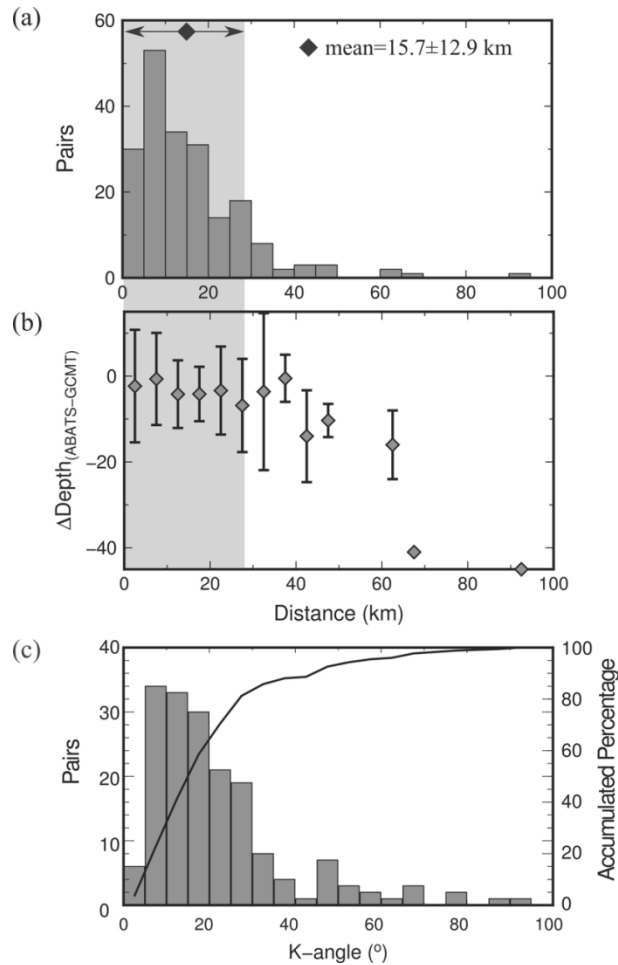
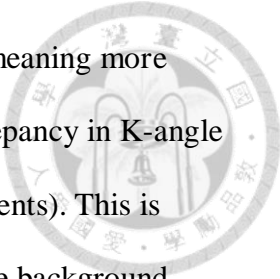


Figure 2.5 Diagram illustrating the consistency between AutoBATS MT and Global CMT.

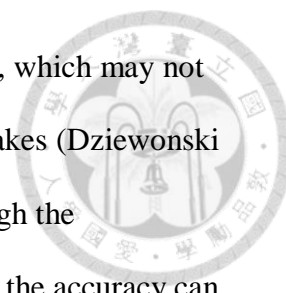
(a) Numbers of matched event pairs and (b) average depth differences between matched pairs in AutoBATS MT and GCMT catalogs with respect to the epicenter difference (bin size for distance is 5 km). Only the earthquakes within the cutoff epicentral distance (shaded area) are included in the MT comparison between GCMT and AutoBATS catalogs shown in (c) and Figure 2.6. (c) The K-angle distribution for 176 event pairs in the final comparison.

Overall, more than 80% of the matched event pairs have a K-angle smaller than 30° with a mean of $22.0 \pm 16.6^\circ$ (Figure 2.5c). The remarkable consistencies between AutoBATS and GCMT are also evidenced by the small difference in centroid depth (Δdepth) of -2.8 ± 9.8 km. We further investigate their correlations with magnitude, depth, and geographic locations (Figure 2.6). Apparently, most matched events are located in the ocean (Figure 2.6a). The relation of K-angle to MW demonstrates that



larger earthquakes tend to have smaller differences in MT solutions, meaning more consistency between the two catalogs (Figure 2.6b). The largest discrepancy in K-angle appears in the group with the smallest magnitude 4.4~4.6 (only six events). This is probably because teleseismic long-period records suffer more from the background noise for small earthquakes ($M_w \leq 4.6$) in GCMT. The negative mean Δdepth ($d_{\text{ABATS}} - d_{\text{GCMT}}$) indicates that GCMT tends to obtain deeper centroid depths compared to AutoBATS solutions (Figure 2.6c). The MT solutions can differ a lot (K-angle $> 60^\circ$) when focal depths are poorly constrained (like the case in Figure 2), especially for those located farther offshore from Taiwan and with poorer azimuthal coverage (Figure 2.6a and 6c). Except for the two events with focal depth differences exceeding 40 km, all other pairs from the two catalogs seem reasonably consistent for the focal mechanisms (i.e., smaller K-angles), particularly when Δdepth is negative (Figure 2.6c).

Statistically speaking, our AutoBATS MT solutions for $M_w > 4.6$ earthquakes agree well with the GCMT reports. The comparison results reveal several key reasons for differences and help identify advantages/disadvantages of AutoBATS. First, the azimuthal coverage of local BATS is quite limited for earthquakes in the ocean far offshore from Taiwan. Under this condition, GCMT can perform better than AutoBATS as long as the earthquakes are large enough for quality recordings at global seismic distances, since events potentially with large errors in hypocenters have been excluded in the comparison. For earthquakes in inland Taiwan, the regional MT inversion of AutoBATS can provide greater opportunities to solve reliable MT solutions. Second, the velocity models used are different. The global velocity model used by GCMT for all earthquakes worldwide is more suitable for fitting very



long-period teleseismic waveforms (above 40 s) of large earthquakes, which may not be ideal for accurately determining focal depth for moderate earthquakes (Dziewonski et al., 1981; Ekström et al., 2012). For regional MT inversion, although the heterogeneity of the velocity structure under the array is challenging, the accuracy can be improved in our AutoBATS MT inversion by exploring different Moho depths of the velocity models and grid-searching suitable focal depths. Third, different frequency bands used for GCMT and AutoBATS MT inversions are likely to yield systematic variance of focal mechanisms and centroid depths between the two catalogs. Appropriate frequency range for regional CMT inversion is around 10~50 s, but longer periods above 45 s are more typical for global studies. Kagan (2003) studied the difference between two global CMT catalogs (Global CMT and NEIC MT), and the resulting average K-angle was $25.3 \pm 16.5^\circ$ based on 1385 earthquakes with magnitude greater or equal to 6. This value is comparable to our mean difference ($22.0 \pm 16.6^\circ$) for Taiwan, suggesting that the AutoBATS MT inversion scheme developed in this study has the ability to retrieve reliable MT results. When more event pairs are accumulated, we can perform similar analysis on CLVD and focal depth, as in Kagan (2003), to fully evaluate the effects of mislocations on the focal mechanisms determined from AutoBATS and Global CMT catalogs.

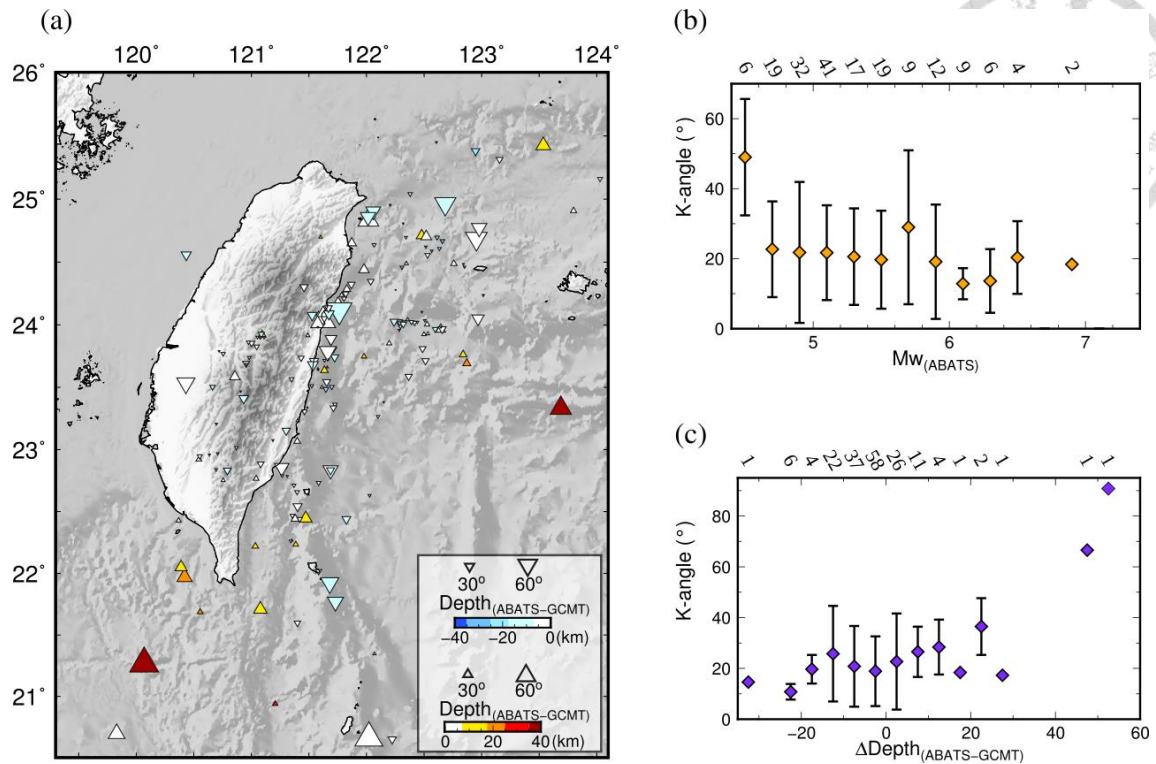



Figure 2.6 Comparisons of the focal mechanism and centroid depth between AutoBATS and Global CMT catalogs.

(a) Map showing the differences in MT (measured by K-angle) and depth for all matched event pairs. Locations of symbols (triangles) are plotted according to reported epicenters by CWB. Size of symbols is scaled with the K-angle and color represents the centroid depth of AutoBATS (denoted as ABATS in this figure) relative to GCMT (i.e., AutoBATS minus GCMT). Triangles and inverted triangles represent event pairs with AutoBATS depths that are deeper and shallower than GCMT's estimates, respectively. (b) The relation between average K-angle and magnitude (bin size of magnitude = 0.2). (c) The relation between average K-angle and $\Delta\text{Depth}_{(\text{ABATS}-\text{GCMT})}$ (bin size of depth = 5 km). The numbers of earthquakes in each bin are denoted above.

2.5.2 Comparisons between the original BATS and new AutoBATS MT solutions



There are 1176 event pairs matched from the original BATS and the new AutoBATS MT catalogs. Since both catalogs are based on the same local seismic network data and similar simple 3-layer velocity models, we expect the results to be more consistent than AutoBATS versus GCMT. To our surprise, the mean K-angle ($31.4 \pm 22.3^\circ$) was considerably higher, although the mean $\Delta\text{depth}_{(\text{ABATS-BATS})}$ (-1.8 ± 8.7 km) was reduced by 1 km with a comparable S.D. relative to $\Delta\text{depth}_{\text{ABATS-GCMT}}$. Large discrepancies on K-angles were found in northeast and southeast offshore areas where the Ryukyu subduction zone tends to have a relatively deeper centroid depth for AutoBATS, but the opposite situation exists beneath the Luzon Arc (Figure 2.7a). Some earthquakes in the Central Mountain Range also showed prominent K-angle differences. Unlike those events offshore, their $\Delta\text{depth}_{\text{ABATS-BATS}}$ were generally small and slightly negative (BATS deeper than AutoBATS). We believe this is because focal depths shallower than 10 km are not resolvable, and a fixed velocity model is used in the previous BATS inversion. Figure 2.7b shows that the K-angle basically remains a constant around 30° until M_w 5.0 and then gradually decreases to 20° as the magnitude increases to M_w around 6. The exceptions occur at extreme magnitudes, probably due to higher noise levels for small events and complex ruptures for large events. Another important finding is the strong dependency of the mean K-angle on the differences of centroid depth measured from BATS and AutoBATS MT catalogs. Figure 2.7c reveals a positive correlation between the mean K-angle and the depth differences. This pattern is appreciably different from Figure 2.6c for the comparisons between AutoBATS and Global CMT, which proves again the strong dependency of moment tensors on focal

depth for regional MT inversion. Overall, the centroid depths from the AutoBATS MT catalog is more consistent with the relocated focal depth in the CWB catalog, as indicated by the mean and S.D. of differential depth $|\Delta depth_{(ABATS-CWB)}| = 2.6 \pm 6.9$ vs. $|\Delta depth_{(BATS-CWB)}| = 4.4 \pm 8.4$.

We notice that there is no event with a centroid depth shallower than 10 km in the original BATS catalogs. After careful inspections and one-to-one comparisons on several shallow earthquakes, we believe the limited resolution on depth in the current BATS catalog is caused by insufficient resolution of the Green's Function calculation algorithm or the inversion process itself. In contrast, the new AutoBATS MT inversion is able to resolve centroid depth in the shallow crust without problems. In addition to the improvements on the focal depths, our new AutoBATS MT solutions are also relatively more consistent with Global CMT. This is clearly supported by larger $K\text{-angle}_{BATS-GCMTs}$ ($27.4 \pm 18.9^\circ$ from 204 event pairs) compared with $K\text{-angle}_{ABATS-GCMTs}$ ($22.0 \pm 16.6^\circ$ from 176 pairs).

The BATS data center used to release the so-called “final” MT solutions (FCMTs of BATS), which were obtained by fine-tuning the inversion settings manually after relocated earthquake bulletins of CWB were available (Kao and Jian, 1999, 2001). Due to the restriction on human resources, starting from November 2006, BATS only reports quick MT solutions (QCMTs) based on CWB's preliminary epicenters, a fixed frequency band (0.03 ~ 0.08 Hz), and a three-layer velocity model with Moho depth at 40 km. We divide BATS CMTs into two subsets, FCMTs and QCMTs, and compare them separately with AutoBATS MT solutions. By excluding those shallow events that might have the depth problems mentioned in the previous paragraph, we find that the mean $K\text{-angle}_{FCMT-ABATS}$ ($33.8 \pm 25.0^\circ$) is apparently larger than $K\text{-angle}_{QCMT-ABATS}$

($24.4 \pm 15.6^\circ$). Even though time-consuming efforts had been made to manually adjust the MT inversion parameters or settings, the greater deviation of FCMTs solutions from AutoBATS implies that the quality of inversion results strongly relies on the experiences of operators who produced FCMTs, and how many settings or parameters have been tried thoroughly for the MT inversion. It also supports that a comprehensive scanning is necessary and an effective way to produce a reliable MT catalog.

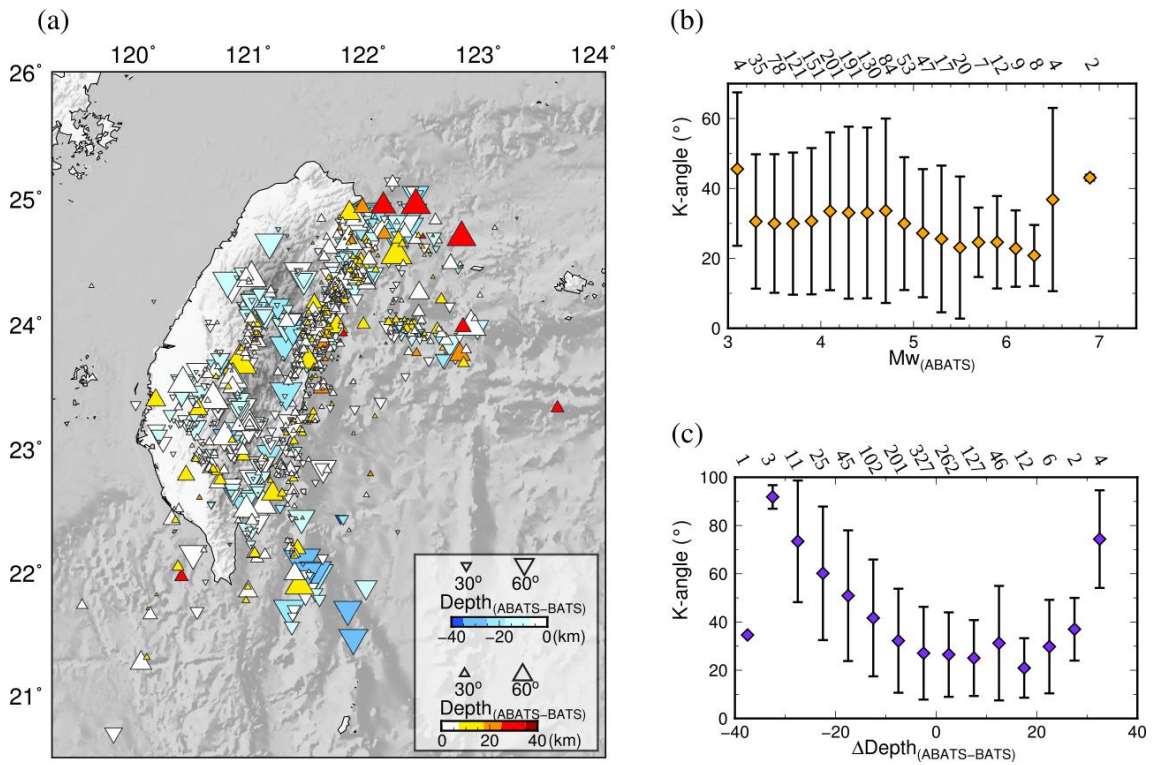


Figure 2.7 Comparisons of the focal mechanism and centroid depth between AutoBATS and BATS catalogs.

(a) Map showing the differences in MT (measured by K-angle) and depth for all matched event pairs. Sizes and colors of symbols are the same as in Figure 2.6a. AutoBATS is denoted as ABATS in this figure. (b) The relation between average K-angle and magnitude. (c) The relation between average K-angle and $\Delta\text{Depth}_{\text{ABATS-BATS}}$. The numbers of earthquakes in each bin are denoted above.

2.5.3 Moment magnitude and local magnitude relationship for Taiwan

It has been noted that the moment magnitude is usually underestimated for earthquakes determined from regional seismic networks relative to those obtained from global studies (Chen et al., 2008; Gasperini et al., 2012). Gasperini et al. (2012) found the mean difference of estimated M_W is negligibly small, only about 0.027, for earthquakes in the European-Mediterranean (MED) area. For the Taiwan region, Chen et al. (2008) compared the M_W of BATS MT/CMT catalog with Global CMT for 79 event pairs and found a significantly large mean offset of about 0.3. They proposed that the underestimation of M_W by BATS was caused by insufficient low-frequency signals used in the regional moment tensor inversion. This issue does not exist in our new AutoBATS MTs because the mean offset of M_W between the AutoBATS MT and Global CMT catalogs is very small (-0.08 ± 0.10). Accordingly, the reasoning suggested by Chen et al. (2008) can be ruled out. Compared to our AutoBATS MTs, the M_W from BATS is indeed smaller by 0.15 ± 0.18 on average, similar to the value recently reported by another regional MT study in Taiwan (Lee et al., 2014).

We further investigate whether the M_W differences between AutoBATS and Global CMT have any relation with the size of earthquakes. In Figure 2.8a, regression from all event pairs shows a straight line with positive slope defined by the equation $\Delta m = a_1(m - m_c) + a_0$, where m is the M_W from the AutoBATS; m_c is the minimum M_W of the compared event pairs from AutoBATS; Δm is the ABATS-GCMT magnitude difference; a_1 and a_0 are the slope and bias terms. When the regression coefficients, a_0 and a_1 , are close to zero, the differences in magnitude are likely caused by random errors rather than systematic errors (Kagan, 2003). This is

indeed the case ($a_1 = -0.017$ and $a_0 = 0.002$) for the M_W comparison between Global CMT and USGS-MT catalogs, whereas a systematic bias ($a_0 = 0.280$) and dependence of magnitude ($a_1 = 0.141$) between M_W (from Global CMT) and M_b (from PDE) are predictable (Kagan, 2003). Compared to our AutoBATS to Global CMT catalogs, the minor bias term ($a_0 = 0.14$) together with the small mean M_W offset (-0.080 ± 0.10) shows that the underestimations on M_W in the AutoBATS catalog are negligible. The small slope ($a_1 = 0.063$) also indicates that the difference in M_W between AutoBATS and GCMT is not significantly related to magnitude.

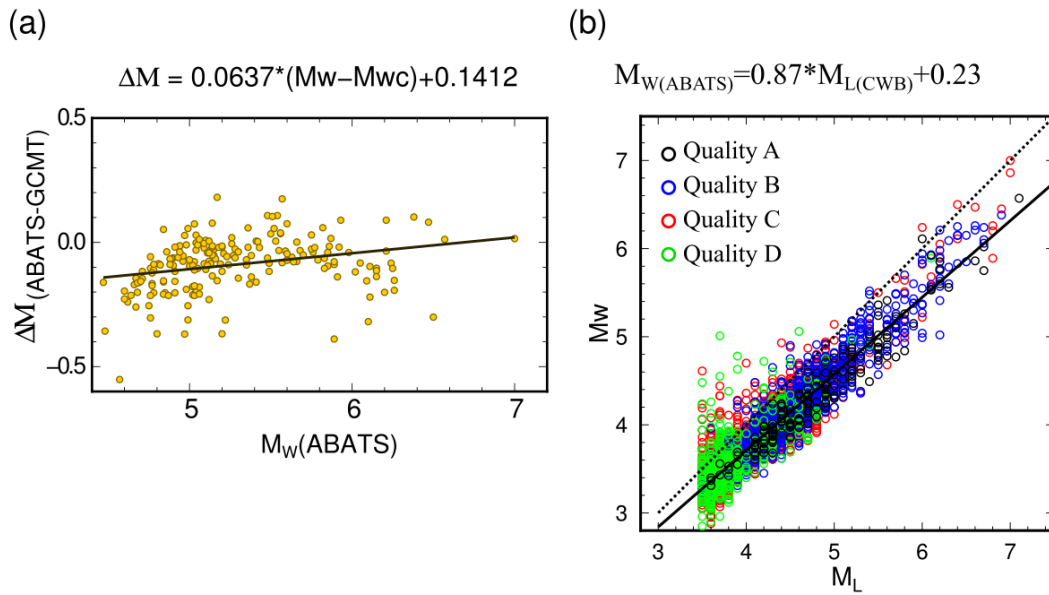
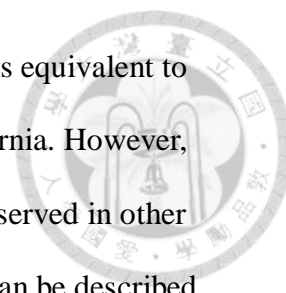


Figure 2.8 M_W differences between AutoBATS and Global CMT catalog and relation of $M_{W(ABATS)}$ and $M_{L(CWB)}$.

(a) Relation of M_W differences between AutoBATS (denoted ABATS) and GCMT with respect to $M_W(ABATS)$. M_{WC} in the regression relationship is the minimum M_W in the AutoBATS catalog. See main text for details. (b) The relation between $M_{L(CWB)}$ and $M_{W(ABATS)}$. The symbols are colored according to the inversion quality factor. The dashed line marks the 1 to 1 ratio. Regression is performed for earthquakes above quality C.

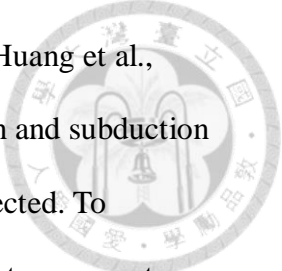


Hanks and Boore (1984) demonstrated that in principle the M_L is equivalent to M_W for the magnitude range from 3 to 5 using earthquakes in California. However, deviation from the 1:1 relation between M_W and M_L is commonly observed in other regions (Hanks and Boore, 1984; Deichmann, 2006). If the relation can be described by $M_W = aM_L + b$, the results usually varied widely depending on the geographical region (frequency-dependent attenuation), focal depth (Ristau, 2009), magnitude range, formulations of the empirical distance correction used for calculating M_L e.g. (Shin, 1993; Ristau, 2009), and the algorithm for deriving M_W (Bethmann et al., 2011). Over/under estimating M_L can seriously influence the calculation of magnitude recurrence relations (b-values), which are related to seismic hazard. With many reliably estimated M_W from AutoBATS MT catalog, we determine a new linear regression relation of seismic moment and local magnitude for the Taiwan area. As Figure 2.8b shows, M_W and M_L are correlated linearly for a large range of magnitudes from M_L 3.5 to 7. Because data with quality level D is dominant in small events and relatively scattered, we use quality A-C (total of 2667 pairs) to estimate the relation:

$$M_W(ABATS) = 0.87M_L(CWB) + 0.23 \quad (\text{or equivalently})$$

$$M_L(CWB) = 1.01M_W(ABATS) + 0.28).$$

The result is comparable to $M_L(CWB) = 1.05M_W + 0.25$ estimated using 3 years of real-time CMTs (Lee et al., 2014). Basically, an earthquake reported with M_L 7.0 would correspond to a much smaller M_W of only about 6.3. The size of moment and local magnitudes are more comparable for small events. Based on the properties of scaling relation modeled in Switzerland (Edwards et al., 2010), we speculate that the increase of M_W - M_L differences with respect to magnitude is controlled by attenuation, and the continuation of linearity to magnitude 6+ implies stress drop at the order of 10 MPa or more. High stress drop is



consistent with the reported values for major earthquakes in Taiwan (Huang et al., 2001; Yen and Ma, 2011). Note that our dataset includes both collision and subduction zones covering inland and offshore Taiwan. Regional variation is expected. To understand the first-order changes in property, we attempt to calculate two separate regressions for 2396 shallower ($\text{depth} \leq 40\text{km}$) and 271 deeper ($\text{depth} > 40\text{km}$) events with a quality above C. Then, we find their differences are minor: $M_w = 0.90M_L + 0.13$ (or $M_L = 0.97M_w + 0.38$) for shallow vs. $M_w = 0.87M_L + 0.11$ (or $M_L = 1.03M_w + 0.40$) for deep. High quality data for offshore deep events in the subduction zones are yet to be accumulated for better estimates of M_L - M_w relations and the structure dependency should be further investigated in future research.

2.5.4 Seismotectonic features revealed by AutoBATS MTs

A complete, well-constrained regional MT/CMT catalog is the key to understanding the relation of regional tectonic stress and strain (Kao and Jian, 2001; Zhu et al., 2006; Hsu et al., 2009; Martin et al., 2015; Tseng et al., 2016; Huang et al., 2017). In Figure 2.9, we highlight two profiles with cross-sections of the background seismicity from CWB and focal mechanisms determined from AutoBATS. The profile AA' cuts through the Ryukyu subduction zone northeast of Taiwan (Figure 2.1). The cross-section clearly delineates the Wadati-Benioff Zone (WBZ) of the northward subducting Philippine Sea plate underneath the Eurasian Plate, down to a depth of around 300 km (Figure 2.9a). In the past, the focal mechanisms of intermediate-depth earthquakes near Taiwan have mostly been constrained from tele-seismic studies for large events only (Kao et al., 1998b, 2000). Based on regional data, our new

AutoBATS MT catalog provides many solutions that are reasonably robust and has the potential to reveal details of features in the subduction zones (Figure 2.9), although the sensitivity in focal depth is somewhat less than ideal due to the simple half-space model below Moho (Figure 2.3). The cross-section reveals that shallow normal faulting events are dominant under the Okinawa Trough north of the Ryukyu Trench. It is remarkable to see the continuation of the focal mechanisms determined from shallow to the intermediate-focus earthquakes, which can be used to understand the stress along the subducting slab.

Figure 2.9b shows another cross-section in NW-SE direction passing through the Tainan Basin, southern Central Mountain Range, southernmost Longitudinal Valley, and Luzon Arc on the Pacific Ocean. We can identify those mid-crust events (including the 2010 Jiashian and the 2016 Meinong M6+ earthquakes) at a depth ~20 km near the Western Foothills of Taiwan. The focal mechanisms are consistent with former studies (Huang et al., 2011; Lee et al., 2016; Kanamori et al., 2017). A cluster of normal faulting events is also clearly observed at shallow depths (<10 km) near the southern range of the Central Mountains. In the eastern end of the profile, the background seismicity depicts the subduction to a depth of approximately 200 km. Compared with the Ryukyu subduction zone in Figure 2.9a, the resolvable focal mechanisms here are far fewer mainly because the earthquake activity is weaker. However, overall, the WBZ is clear, and the pattern of focal mechanisms is similar to the study of Kao et al. (2000). There seems to be another group of earthquakes near the eastern end of BB' slightly dipping east under the Pacific to a depth of approximately 40 km in the mantle, which has not been observed before.

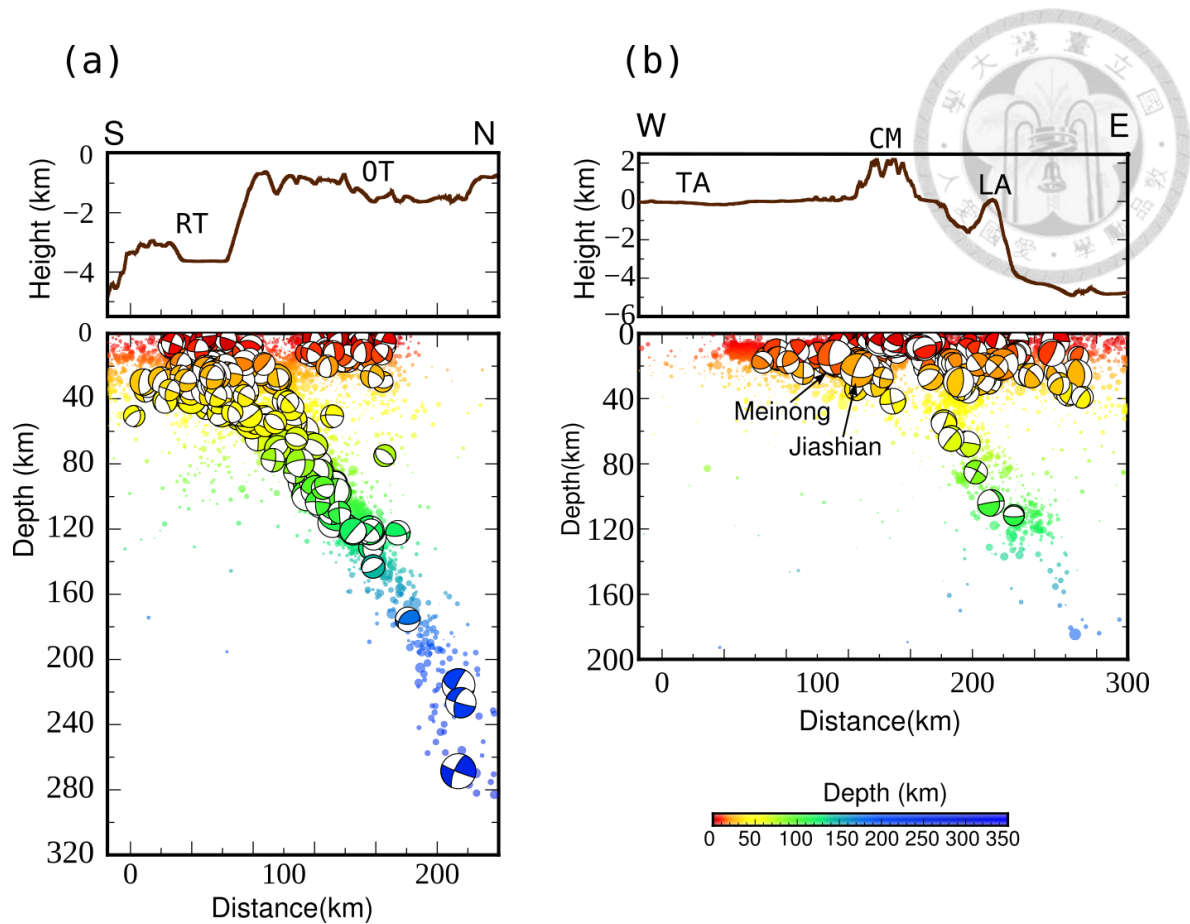



Figure 2.9 Cross-sections of focal mechanisms from AutoBATS catalog.

Cross-sections of focal mechanisms overlapped with the background seismicity for profiles (a) AA' and (b) BB' indicated in Figure 2.1. The seismicity (circles) with $M_L \geq 2.5$ from CWB and all focal mechanisms (beach balls) with $M_W \geq 4.0$ determined by our study are colored according to focal depth. The cross-sections are plotted with one-to-one scale. Exaggerated topography is shown on the top of each profile. Abbreviated terms of tectonic units: RT, Ryukyu trench; OT, Okinawa Trough; TB, Tainan Basin; CM, Central Mountain Range; LA: Luzon Arc. The focal mechanisms of 2010 Jiashian and 2016 Meinong earthquakes are also denoted in profile BB'.

2.6 Conclusions



In this study, we presented a new automatic regional MT inversion algorithm, which we applied to determine over 3000 CMT solutions from May 1996 to April 2016 in the Taiwan area. The final focal mechanism of each earthquake was chosen from all the results with scanned settings including three station-selection groups, four velocity models, three frequency bands, and three isotropic component constrained strategies. Both the focal mechanism and moment magnitude from AutoBATS show better consistency with GCMT solutions than the current BATS catalog. Compared to the current BATS catalog, the AutoBATS also advances remarkably in the capability of resolving the focal mechanisms for earthquakes at a broader depth range (from 1 to 300 km). The fast and reliable AutoBATS inversion system is now implemented in the Data Management Center of IES (DMC-IES). Once triggered by the CWB's earthquake alarm system, it only takes a short time (as fast as 2 minutes) for the AutoBATS to publish a MT solution automatically on the Taiwan Earthquake Scientific Information System (Liang et al., 2017) (TESIS). The DMC-IES also updates the final MT solutions monthly with the relocated earthquake catalog provided by CWB. The updated AutoBATS solutions will be online soon at the BATS website. The real-time triggered AutoBATS inversion algorithm together with the earthquake alarm system from CWB deliver fast and reliable basic earthquake information, including epicenter location, focal mechanism, and moment magnitude. The reliable AutoBATS MT catalog with relocated hypocenters can be used to improve our understanding of the seismotectonic background, seismic hazard, and regional stresses for the Taiwan area.



Chapter 3 3D MUSIC back projection rupture images of the 2013 great Okhotsk deep earthquake sequence



3.1 Abstract

On May 24, 2013, the largest deep earthquake ever seismically recorded struck 609 km beneath the Sea of Okhotsk off the southwest coast of Kamchatka Peninsula. Previous multiple point-source inversion results have shown that the earthquake might not rupture along the subhorizontal fault plane as presumed in the finite-fault inversion. Here we employ a three-dimensional (3-D) high-resolution MUSIC BP method to revisit the spatiotemporal characteristics of the rupture processes for this great event and its two largest aftershocks. The multitaper cross-spectrum estimator and MUSIC (MUltiple SIgnal Classification) Back Projection method are combined to first obtain robust data covariance matrix for each sliding time window of seismic waveforms recorded by dense array and back project them to retrieve the space-time energy distribution. We apply such array-processing procedures to P waves filtered at the two frequency bands of 0.5-2.0 Hz and 0.2-1.0 Hz recorded by the seismic networks across the US and Europe. The low frequency P- and pP wave BP images are combined to diminish the spatial uncertainties of 3D BP images. All the BP results are inspected jointly to characterize resolved features, with the aid of synthetic tests performed to assess the recovery capability of the 3D complex rupture scenario. Our results corroborate that the mainshock occurred as the en echelon-like fault ruptures along the two nearly parallel, N-S striking subhorizontal planes but in the opposite direction of propagation with the depth separation of 10~15 km. The rupture began propagating

NNE-wards during the first 8~12 s; afterwards it concurrently shifted downward and reversed to Southward lasting for about 18~20 s. The lengths of these two ruptures are estimated to be about 27~40 and 80~85 km with the average propagation speeds of 3.3 and 4.25 km/s, respectively. Two M_w 6.7 aftershocks have similar rupture properties as indicated by the similarity of simple, short-duration P waveforms. The 3D BP images resolved with the European data delineate rupturing along subvertical fault planes that may reach supershear rupture speeds.

3.2 Introduction

The great May 24, 2013 Sea of Okhotsk earthquake struck very deep about 608 km below the seafloor, where the Pacific Plate is being subducted beneath the Okhotsk microplate at the Kuril-Kamchatka Trench. Peculiarly enough, it occurred within the deep slab of the relative seismic quiescence but activation recently in close proximity of the northern terminus of the Pacific slab penetrating over 500 km (Figure 3.1). This deep earthquake has drawn much attention in that it is the largest ever-recorded deep event with a moment magnitude (M_w) of 8.3 being well observed by modern dense seismograph networks distributed globally. The high-quality seismic recordings provide an unprecedented opportunity to explore and distinguish the physical origin of deep earthquakes in much detail from a number of existing and still debated mechanisms. Among them, there are three main competitive models as follows: (1) dehydration of hydrous minerals within subducted lithospheric mantle causing local weakening and shear failure (Meade and Jeanloz, 1991; Silver et al., 1995; Kirby et al.,

1996; Peacock, 2001), (2) thermal runaway instability facilitated by positive feedback between viscous heating and thermal weakening in ductile shear zones (Ogawa, 1987; Kanamori et al., 1998; Karato et al., 2001; John et al., 2009), and (3) transformational faulting caused by the nucleation and growth of anticracks filled with spinel transformed from the metastable olivine within cold slabs (metasable olivine wedge) (Green II and Burnley, 1989; Green II and Houston, 1995).

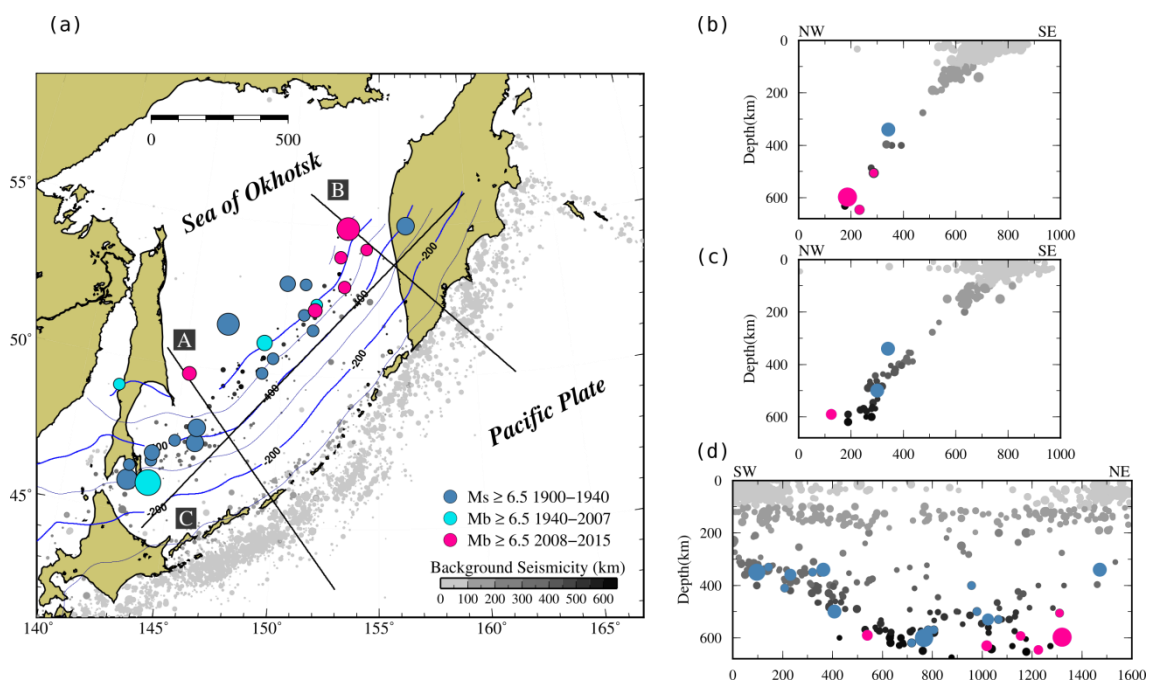
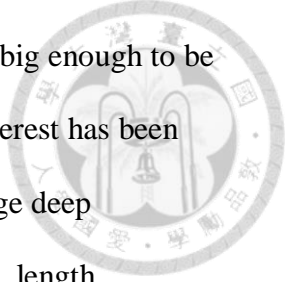


Figure 3.1 Historical deep-focus seismicity of Kuril subduction zone since 1900.

The circles representing the background seismicity ($M > 3.5$) are colored by the focal depth and scaled with magnitude. Earthquakes with magnitude larger than 6.5 are enlarge and colored by three different periods: blue for 1900 to 1940; light blue for 1940 to 2007 and purple for after 2008. The light gray lines show the slab contour from slab 1.0 model (Hayes et al., 2012). The cross-sections of seismicity shown in (b)-(d) are for profiles A, B and C, respectively.



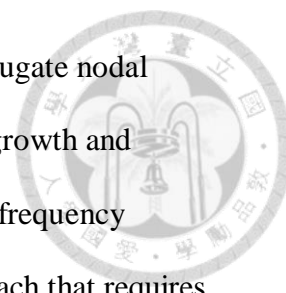
Since the 1994 Bolivia and Tonga deep earthquakes which were big enough to be recorded well by modern digital broadband instrumentation; much interest has been devoted to seismological investigation of the rupture properties of large deep earthquakes including the fault-plane orientation, the rupture duration, length, propagation speed and directivity, stress drop, radiation efficiency, and etc. (Houston and Vidale, 1994; Chen, 1995; Wiens and McGuire, 1995; Heaton, 1998; Warren and Shearer, 2006; Suzuki and Yagi, 2011). Detailed studies of the spatiotemporal distribution and source characteristics of deep earthquake aftershock sequences (Wiens et al., 1994) and repeating deep earthquakes (Wiens and Snider, 2001; Yu and Wen, 2012) have also been conducted to help unravel the main shock rupture behavior and fault reactivation mechanism at great depth. Though these seismic constraints have greatly improved our comprehension of the nature of deep earthquakes, both the uncertainty and variability of resolution in the estimated source parameters still remain, making it challenging to verify which postulated scenario is most plausibly involved in the nucleation, growth and coalescence of deep-earthquake rupture faulting (Frohlich, 2006).

On the other hand, the thermal structure of subducted slabs has long been considered critical for the generation of deep earthquakes (Isacks et al., 1968; McKenzie, 1969), as indicated by the increase of the maximum depth of deep earthquakes with the thermal parameter, the product of the vertical descent rate and age of the plate entering the trench (Molnar et al., 1979; Kirby et al., 1991). Gorbatov and Kostoglodov (1997) re-examined the maximum earthquake depth as a function of thermal parameter from the seismicity distribution in the subduction zones with no bathymetric features being subducted as well as reliable plate age estimates. The result

shows an abrupt increase from 260 km to 700 km for the slabs with the thermal parameters of 3500-5000 km. However, considerable uncertainties of slab age and vertical descent rate cause large varieties in thermal parameter determinations. The thermal parameter of the Kuril-Kamchatka subduction zone is estimated about 4000-4400 km (Gorbatov et al., 1997) or 6000 km (Frohlich, 2006), the cutoff depth of deep earthquake is expected to exceed 600 km.

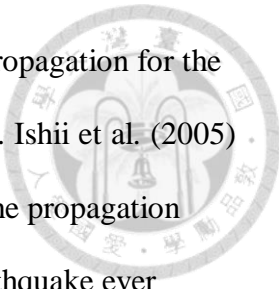
From 1900 to 1940, a group of large deep earthquakes ($M \geq 6.5$) occurred in the central-northern segment between 48°N and 53°N, which became inactive afterwards (Figure 3.1). Further north, the seismicity below 400 km depth under the southwest of the Kamchatka peninsula had remained quiescent until 2008. A series of large-to-great deep events occurred in the depth range of 450-660 km between 52°N and 54°N, including the 2013 M8.3 Okhotsk earthquake. The deep seismic activity appears to cease north of 54.5°N, coinciding with the increase of surface heat flow resulting from the subduction of the Meiji seamounts and abrupt shallowing of slab seismicity and dip angle (Davaille and Lees, 2004b). The region is adjacent to the Kamchatka-Aleutian corner where the west-dipping, trench-normal subduction of the Pacific plate along the Kuril-Kamchatka trench suddenly turns to the transcurrent motion along the western Aleutian trench. Davaille and Lees (2004b) suggested that the subducted Pacific lithosphere thinned previously on passage through the Meiji-Emperor-Hawaiian hotspot track has been torn to accommodate the deformation at the corner.

The Global CMT solution (Ekström et al., 2012) indicates that the 2013 Okhotsk deep earthquake ruptured on the nearly N-S striking, either subhorizontal or subvertical plane (Figure 3.3). Unlike shallow mega earthquakes which often produce surface ruptures and numerous aftershocks to facilitate the identification of the fault plane,



there usually exists an ambiguity to distinguish between the two conjugate nodal planes resulting equally fitting observed waveforms. With the rapid growth and availability of dense seismic networks, back projection (BP) of high-frequency coherent body waves has been demonstrated to be an effective approach that requires little a priori knowledge of the fault plane to track the spatiotemporal evolution of the rupture propagation for both shallow and deep great earthquakes (Ishii et al., 2005; Meng et al., 2011; Ye et al., 2013). The BP images constructed from the conventional time-domain beamforming (Kiser and Ishii, 2012; Ye et al., 2013) or frequency-domain subspace methods (Meng et al., 2014) all favor a subhorizontal rupture plane for the Okhotsk event. Ye et al. (2013) also performed the finite fault inversion and found no preference of either nodal planes because they both yield very similar waveform fits. Zhan et al. (2014) preferred the subhorizontal fault plane based on the results of the sub-event method which is based on the directivity effect. However, Chen et al. (2014) attributed its occurrence to a cascading failure on the subvertical fault plane as manifested by the time-space distribution of the subevents composing the main shock from multiple point-source waveform inversion and relocated aftershocks. In addition, the 2D MUSIC BP image on the subhorizontal fault plane reveals a bilateral rupture toward NE and SSE (Meng et al., 2014), while the space-time distribution of the subevent locations resulting from the directivity method suggests the rupture mostly propagating unilaterally along the strike direction (SSE) (Zhan et al., 2014). In spite of some discrepancies between these results, all of them confirm the rupture complexity and enigmatic occurrence of this peculiar deep event.

Motivated by the different conclusions on the rupture plane and characteristics drawn in previous studies, we carry out a 3-D, high-resolution BP source imaging

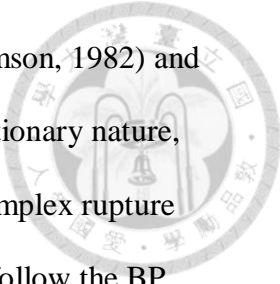


study to reappraise the spatial extent and time history of the rupture propagation for the main shock and its two largest aftershocks of the Okhotsk earthquake. Ishii et al. (2005) first demonstrated the efficacy of the BP method applied to imaging the propagation history of the longest fault rupture of the 2004 Sumatra-Andaman earthquake ever recorded using the dense Hi-net array data in Japan. Since then, a number of improved BP methods including the hybrid stacking (Yagi et al., 2012), compressive sensing (Yao et al., 2011), and MUSIC subspace projection method (Meng et al., 2011) have been developed contributing to exploring the diverse and complex rupture behaviors of subduction zone mega earthquakes. They offer the main advantage that there is no need for a priori knowledge of the fault geometry, source parameters and details of earth structure. Although not directly the measure of the moment rate function with time, the BP image can be interpreted physically as the rupture slip motion as long as the displacement response to a unit impulse slip at the source point, namely the Green's function, is approximately equal to a delta function (Fukahata et al., 2014). This approximation is more appropriate for the simpler P waves of deep earthquakes because they undergo less scattering and attenuation in crust and upper mantle structures. Besides, since the depth-phase arrivals are separated enough in time from direct P waves, they can be also used to image the rupture propagation and combined with that obtained with the P waves to enhance the spatial resolution of the 3-D BP source image (Kiser et al., 2011b).

3.3 Method and data

Back projection source imaging relies on the fundamental time-reversal property inherent to seismic waves. In principle, the waveforms of certain body-wave phases after proper amplitude normalization observed at a distant seismic network are propagated backwards in time through a 1D Earth model to a grid of discrete subfaults for the potential locations of time-evolving seismic radiation. The processing procedures start with calibrating the polarity and aligning the initial parts of phase arrivals. For each candidate source grid, the waveforms are shifted according to the deviation of the grid relative to the hypocenter. Details of the spatiotemporal rupture process are then illuminated by the distributions of the amplitude of stacked waveforms (Ishii et al., 2005; Kiser and Ishii, 2012).

The conventional beamforming technique performs the linear delay-and-sum or Nth-root stack of the waveforms (Rost and Thomas, 2002), inter-station waveform correlation coefficients (Fletcher et al., 2006), and cross correlation functions of the observed seismograms with theoretical Green's functions (Yagi et al., 2012) in the time domain. Alternatively, the frequency-domain MUSIC (Multiple Signal Classification) method employs the eigen-decomposition of the data covariance matrix in each time slice across the array into the signal and noise subspaces; it then locates the corresponding source radiation by finding the steering vector associated with the direction of arrival (DOA) that yields the minimum projection onto the noise subspace; namely, the largest peak of the MUSIC pseudo-spectrum which is defined as the inverse of the projection of the steering vector onto the noise subspace (Schmidt, 1986; Goldstein and Archuleta, 1987).



Combining the robust multitaper cross-spectrum estimator (Thomson, 1982) and “reference window” strategy for transient seismic signals with nonstationary nature, Meng et al. (2011) first applied the MUSIC method to imaging the complex rupture process of the 2011 Tohoku megathrust earthquake. In this study, we follow the BP approach similar to that outlined in their paper and extend to the 3D. Instead of restricting the rupture of the deep event on a single fault plane, we parameterize the potential rupture region into a 3-D grid of source points centered at the hypocenter and spanning 200 km in latitude, longitude and depth directions. The grid space is set to 2 km in each dimension.

In addition to direct P wavetrains typically used in the BP source imaging, other major phases, such as PP and PKIKP can be also useful and provide complementary information on the rupture process (Koper et al., 2012). However, combining the BP images obtained with different phase arrivals at different seismic arrays to jointly characterize the rupture properties may not be so straightforward because the rupture directivity effects are azimuth and distance dependent (Koper et al., 2012). For intermediate-depth and deep earthquakes, the surface-reflected depth phases, pP and sP, share the same source-receiver geometry and similar rupture directivity effects. It is thus straightforward to combine the BP results obtained from direct P and depth phases with the opposite directions of take-off angles to improve the depth resolution of the 3-D rupture image (Kiser et al., 2011b). Therefore, we incorporate the pP wavetrains in our 3D BP analysis to jointly investigate the kinematic rupture properties of the 2013 Okhotsk deep earthquake sequence.

We select vertical velocity seismograms recorded by two dense seismic networks in North America (US) and Europe (EU) (Figure 3.2). We first apply an automatic

detection and picking algorithm (Allen, 1978) to approximately determine the phase arrivals. A waveform cross correlation algorithm (Vandecar and Crosson, 1990) is further employed to fine-tune the phase alignment. The two-step alignment approach improves the quality of coherency of aligned data and the sharpness of the resulting BP images. To ensure both the robustness and resolution of the resulting rupture image and explore any apparent frequency-dependent rupture behavior, we perform the BP of the P waves bandpass filtered in two frequency bands, 0.5-2.0 Hz and 0.125-1.0 Hz. The BP of the pP phases is, however, conducted only in the frequency band of 0.125-1.0 Hz, the highest achievable to perform the BP. The length of the sliding window is adjusted to be at least twice the longest period for each analyzing frequency band with sliding time step of 1 s for high and 2 s for low frequency band BP imaging.

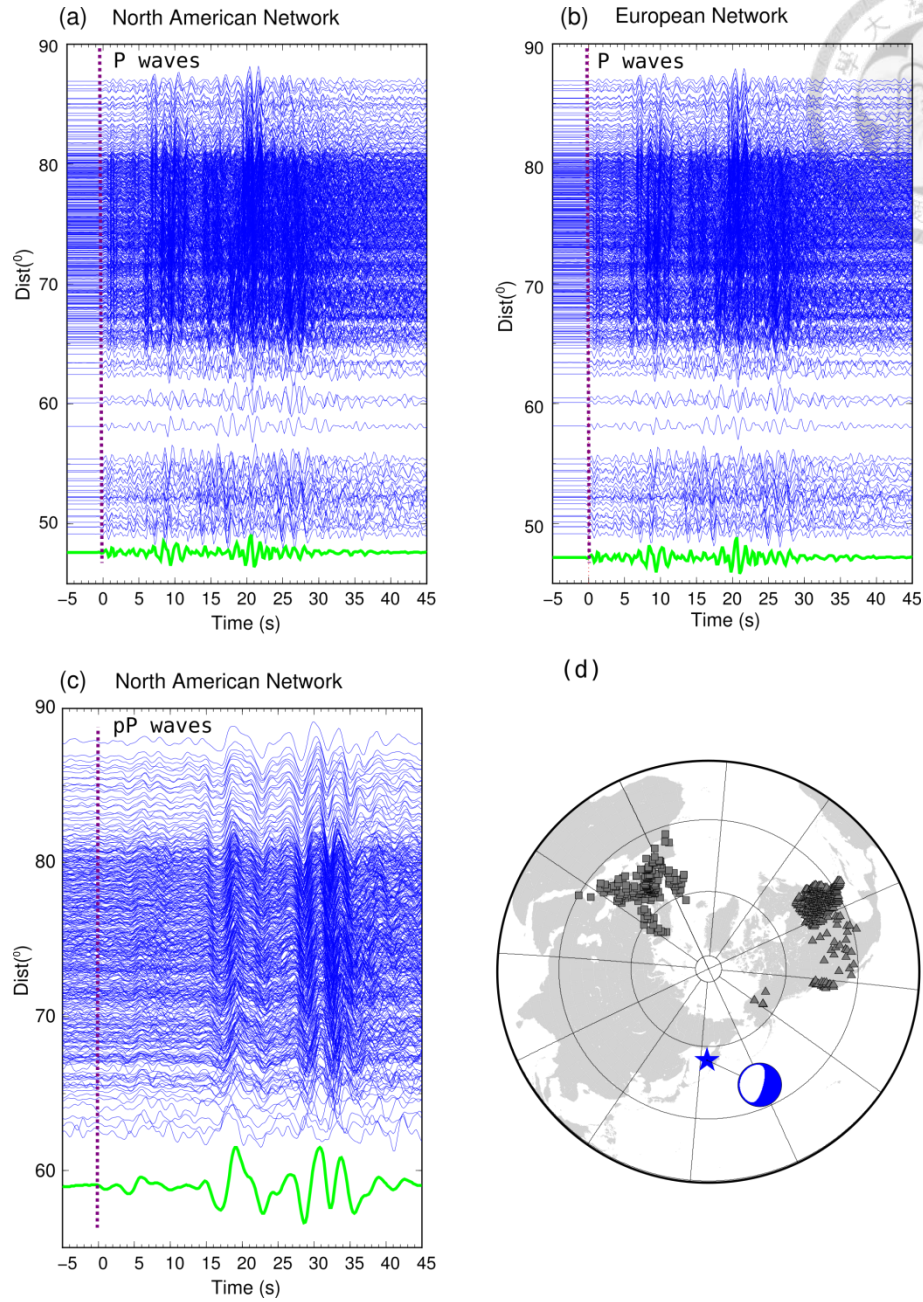


Figure 3.2 Coherently aligned vertical seismograms and seismic networks used for BP images. (a)-(b) The P waves filtered in frequency band of 0.5-2.0 Hz recorded at North American (NA) and the European (EU) seismic arrays. (c) The aligned pP waveforms filtered frequency band of 0.125-1.0 Hz recorded at NA array. Purple dash lines show the onset time of the P and pP waveforms. (d) The seismic stations from NA (triangle) and European (square) arrays used in this study.

3.4 3D BP rupture image of the 2013 Okhotsk earthquake sequence

3.4.1 Two-stage antiparallel subhorizontal rupture

In Figure 3.3, we show the map views and cross-sections of the time-space evolution of the mainshock rupture resulting from the 3D BP of P waves in high frequency range of 0.5-2 Hz recorded by the US and EU seismic network. Snapshots of the rupture propagation illuminated by the strongest seismic radiation associated with the largest peaks of the MUSIC pseudospectrum. The maximum amplitude of pseudospectrum with respect to time (Pseudospectrum Source Time Function, PSTF for short) reflects the temporal rupture evolution and the total duration time of the earthquake, although the MUSIC pseudospectrum is govern by both the relative source strength and the coherency of wavefield. The color-shaded regions corresponding to the source emitters with the pseudospectrum power greater than 95% of its maximum value are used for a crude measure of the uncertainties. The spatial uncertainties are majorly conducted by the smearing effect (Ishii et al., 2007) which usually forms an ellipse with long axis parallel to the ray-to-array path.

The PTSFs of NA and EU arrays reveal the complex temporal rupture history. For NA seismic array, the PSTF (Figure 3.3c) shows two-stage of energy bursts both lasting for about 16 s. The map view of 3D BP image of NA array indicating that two-stage of ruptures propagating in opposite direction. In first 16 s, the rupture stands at the epicenter for ~4 s and then propagates toward N45°E direction for about 30 km. Later, the second rupture starts at 16 s and turns to S-ward for at least 70 km. If looking further at the profiles along two opposite ruptures (Figure 3.3b), we notice that the two ruptures propagate horizontally but at different focal depth. The initial

NE-rupture occurred at depth of ~610 km, however, the Southward-rupture is about 20 km deeper than the initial rupture stage. The profile across two rupture, CC', highlight the vertical aperture between two antiparallel ruptures (Figure 3.3b).

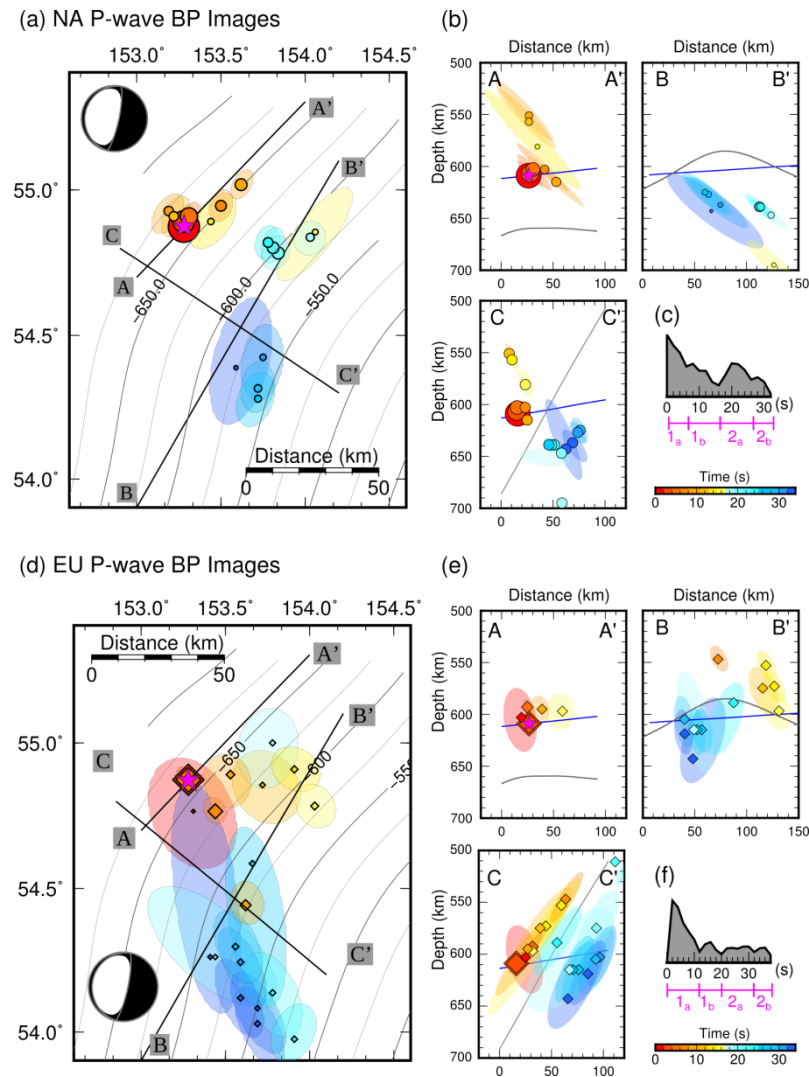
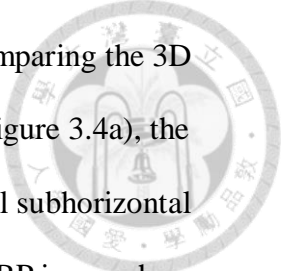


Figure 3.3 High frequency P-wave (0.5~2.0 Hz) 3D BP imaging snapshots for the mainshock. Map and cross-sections showing the 3D BP imaging results from NA (a)-(c) and EU (d)-(f) networks. The colored circles (NA) or diamonds (EU) mark the location with maximum pseudospectrum power of each time window with the corresponding elapsed time after the onset of P wave. The symbols are also scaled with the pseudospectrum power. The colored shadows representing the spatial uncertainties are illustrated by the 95% iso-power with the corresponding maximum pseudospectrum power of each time window. The slab contours from slab 1.0 model are shown by gray lines. (b)&(e) The cross-sections parallel (AA' & BB') and perpendicular (CC') to the rupture direction. The blue lines mark the westward

dipping fault plane. (c)&(f) The pseudospectrum power source time function (PSTF) of 3D BP images.

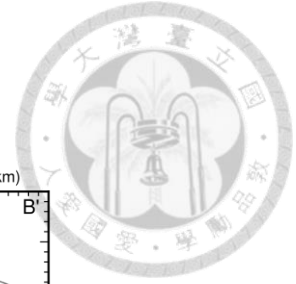
The BP images obtained from EU seismic array as shown in Figure 3.3d suffered much stronger smearing effects than that from US array which result in non-negligible large spatial uncertainties. Considering the ray path of P-wave traveling to EU network, the P waves may be interfered with the subducting slab and the local velocity anomaly of the slab not taken into account for the travel time correction may aggravate the smearing effect of EU BP images. The PSTF (Figure 3.3f) shows the initial strong source rupture amplitude followed by three weak energy bursts. During the first 16 s, the rupture initiates strongly and goes toward ENE-direction for ~ 25 km which is corresponding to the initial strong and first minor energy bursts in PSTF. After 18 s, during the 2nd and 3rd minor energy bursts period, the rupture turns to Southeast and propagates for at last 80 km. Taking average depth of BP results for the first 18s and later 20s, we also notice a ~15 km vertical difference between the ENE-ward and SE-ward ruptures. In view of much larger spatial uncertainty of BP images from EU array, we prefer the results revealed by NA array. Even though with notable spatial uncertainty of 3D BP images especially the EU array, two-stage anti-parallel ruptures propagating at different focal depth are observed from both seismic arrays.

The P-wave 3D BP images of NA seismic array reveal that 2013 great Okhotsk deep earthquake involve two stage antiparallel subhorizontal ruptures, the first NE-ward and the second S-ward deeper ones. The depth difference between two planar ruptures is about 15 ~ 20 km. In order to further clarify the depth difference, we try to diminish the smearing effect by adding the depth phases BP image to P-wave ones in the same filtering frequency band. However, only the pP waves recorded in the NA seismic array is capable to perform BP within the long period of 1~8s. Figure 3.4a&b

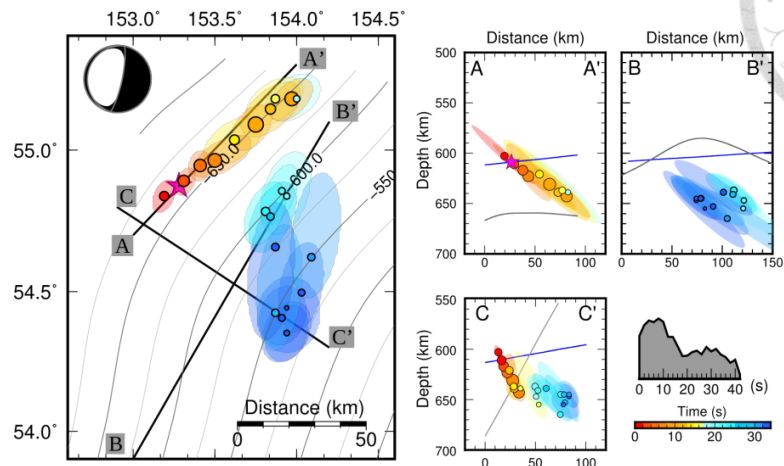


show the long period BP results of P- and pP-waves, respectively. Comparing the 3D P-wave BP images in high and low frequency bands (Figure 3.3a & Figure 3.4a), the BP results are roughly consistent with each other showing anti-parallel subhorizontal rupture within two rupture stages. Not surprisingly, the longer period BP images have more severe smearing effects than the short period ones do. As the pP-wave, the 3D BP image also show great uncertainties not only in horizontal but also along the vertical direction, which is also predictable since the depth phases going up to free surface then to distant receivers typically suffer much more interfering and energy decaying from the local velocity structures above the hypocenter than the P-waves do. In Figure 3.4b, we observe consistent initial NE-ward rupture for first 10 s. After that, the 3D BP results become unstable because of the strong smearing effect. Even though, when we simply sum the BP images of P- and pP waves directly with equal weighting, the smearing effects represented by the colored shadow zones are effectively diminished (Figure 3.4). The 3D integrated BP images showing similar spatiotemporal rupture propagation with the high frequency BP results of P-wave in NA array (Figure 3.3a) ascertain the 10~15 km vertical aperture between two-stage anti-parallel ruptures.

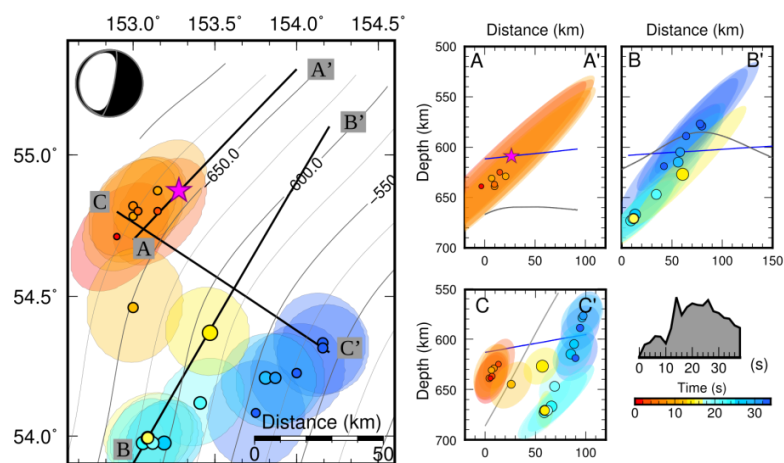
Our 3D BP results reveal an en echelon like anti-parallel rupture behavior of 2013 Okhotsk deep earthquake: two stages of ruptures propagating horizontally in opposite direction with a 10~15 aperture of depth (Figure 3.3 & 3.4). Figure 3.5 summarizes the kinematic rupture properties of rupture length and time revealed by 4 BP imaging results from Figure 3.3 & 3.4. The 1st rupture initiates slowly and propagates NE-ward 30~40 km for 8~12s which leads to average rupture speed of 3.0~3.3 km/s. Later, the 2nd rupture initiates at the east of the original epicenter with focal depth 10~15 km deeper and propagates in much higher speed of 4.25~4.80 km/s for at least 80 km.



(a) P-wave BP Images



(b) pP-wave BP Images



(c) P- + pP-waves BP Images

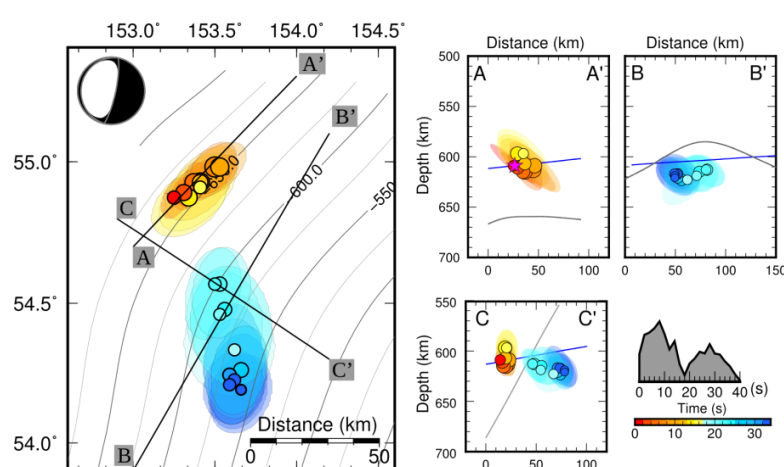


Figure 3.4 Low frequency (0.125~1.0 Hz) 3D BP imaging snapshots for mainshock.

Map and cross-sections showing the 3D BP results of using (a) P-wave (b) pP waves and (c) the

integrated P and pP 3D BP images from NA array. The layout configurations and symbol explanations are the same as in Figure 3.3.

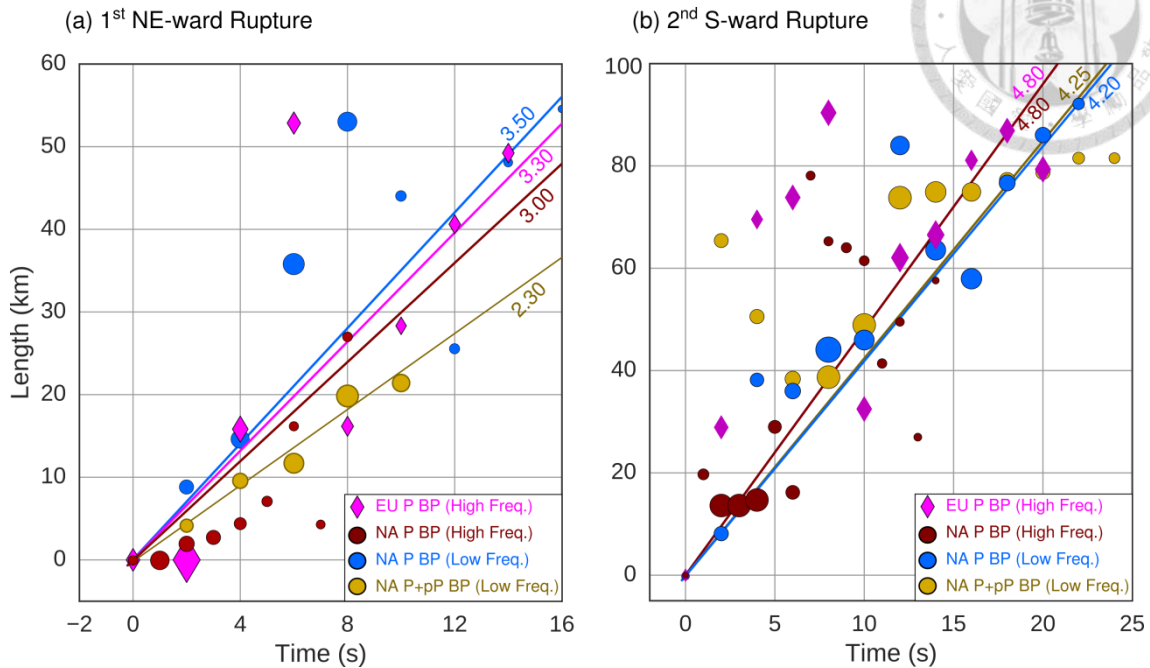
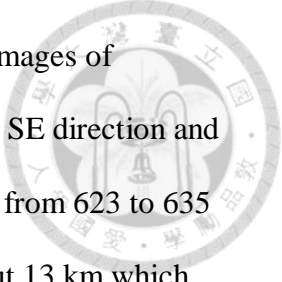


Figure 3.5 3D BP imaging results summaries for the mainshock.

The relation of rupture length respect to time for the (a) 1st NE-ward rupture and (b) 2nd S-ward rupture from the BP results of high frequency P wave at NA or EU array, low frequency pP wave at NA array and low frequency integrated BP results of P- and pP-wave at NA array. The number on each line represents the average rupture speed estimation based on each BP result.

3.4.2 Super shear ruptures of two aftershocks

Few aftershocks induced by the 2013 Okhotsk deep earthquake distributed along N-S direction which is consistent with the 2nd rupture direction. Among them, two larger normal-faulting aftershocks with magnitude greater 6.5 occurred. The first one (abbr. as “2013AS1”) locating at least ~300 km away from the mainshock occurred just 9 hours later. After 130 days, the second delayed one (abbr. as “2013AS2”) fell into the middle of the mainshock and 2013AS1. We perform high frequency BP for two aftershocks and we also notice that the waveforms from both events recorded at



EU array are showing short P-wave pulse (Figure 3.6). In the 3D BP images of 2013AS1 (Figure 3.7a), we see short horizontal movement (~4 km) to SE direction and the cross-section shows that the rupture mainly propagates downward from 623 to 635 km in just 2~3 s (inset of Figure 3.7a). The total rupture length is about 13 km which leads to a potential super shear rupture speed of 4.3~6.0 km/sec (left top inset of Figure 3.7a). Zhan et al. (2014) also concluded a super shear rupture speed reaching 8 km/sec which is much higher than our estimation. Based on the 3D BP result and the focal mechanism reported from Global CMT, this aftershock doesn't rupture along the strike but mainly downward on the SW-dipping fault plane. For the second normal-faulting aftershock "2013AS2", we also perform the BP with P-waves recorded at EU array in high frequency band (1.0~2.0 Hz). As shown in Figure 3.7b, the 3D BP image shows the seismic energy moves northward for ~4.4 km and downward for ~8 km within 2 seconds. The cross-section indicates that the rupture of 2013AS2 earthquake propagates along the N-ward dipping fault plane with super shear rupture speed of 4.5 km/s (bottom inset of Figure 3.7b).

In this section, we revealed the spatiotemporal rupture properties of the 2013 Okhotsk earthquakes sequence including the mainshock and two aftershocks by 3D MUSIC BP imaging. Summarizing these 3D BP results, we found all the earthquakes comprising the vertical ruptures. The later S-ward rupture of mainshock is about 10~15 km deeper than the initial NE-ward stage and two aftershocks both ruptured down-dip along the fault planes. In next section, we intent to comprehend the reliability and resolution of 3D MUSIC BP images on resolving the rupture propagation especially in vertical direction. We design several rupture scenarios and examine the recovery ability of 3D MUSIC BP images by using P-, pP-only and combined P+pP waves

respectively.

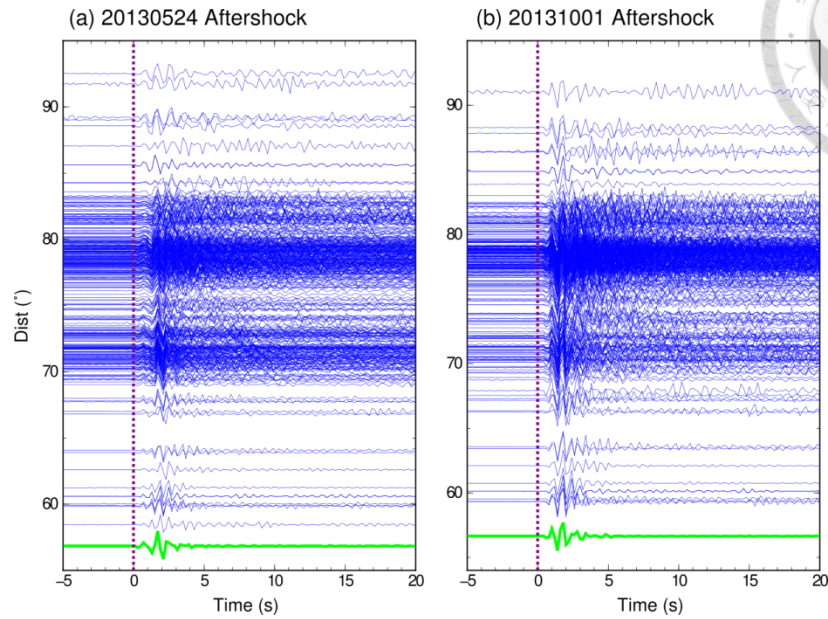


Figure 3.6 Coherently aligned vertical seismograms of two aftershocks from EU seismic network. The waveforms in frequency band of 1.0~2.0 Hz are from aftershocks (a) 2013/05/24 and (b) 2013/10/10. The solid green lines show the stacking waveforms. The purple lines mark the onset time of P waves.

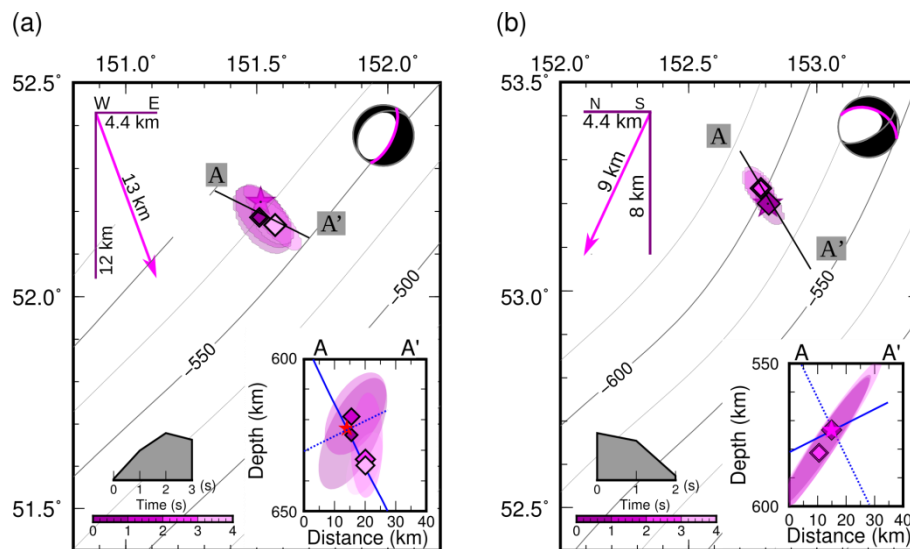
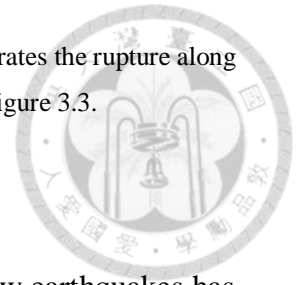


Figure 3.7 High frequency P-wave 3D BP images of two aftershocks by using EU array data. The BP images of (a) 2013/05/24 (1.5~2.0 Hz) and (b) 2013/10/01 (1.0~2.0 Hz) aftershocks. On the beach ball, the magenta thick line highlights the rupture fault plane. Insets: the cross-section along the rupture direction of profile AA'. The rupture fault plane and the conjugate one reported by Global CMT

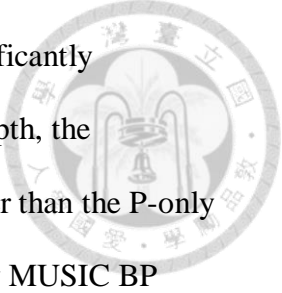
are denoted by solid and dash blue lines, respectively. Top left: the sketch demonstrates the rupture along the horizontal and vertical direction. The symbol explanations are the same as in Figure 3.3.



3.5 Synthetic examination

The superior resolution of the 2D MUSIC BP applying to shallow earthquakes has already been demonstrated by (Meng et al., 2011, 2012a, 2012b). In this section, we further evaluate the reliability of 3D MUSIC BP imaging on several rupture propagation scenarios inspired by the BP results of 2013 Okhotsk deep earthquake sequence. Each hypothetical earthquake source model consists of several subevents to simulate the rupture propagation with presumed rupture speed ranging from 3 to 4.5 km/sec. The NA and EU seismic stations shown in Figure 3.2d are taken as our test arrays. The synthetic waveforms are calculated by the FK method (Zhu and Rivera, 2002) which includes all seismic phases with all ranges of slowness excited by the velocity structure and has better simulation on the nonstationary seismic wave properties than the synthetic waveforms from ray tracing method of WKBJ.

Our first vertical resolution experiment is motivated by the depth difference between two rupture stages of mainshock and fast downward ruptures of two aftershocks. We set up two rupture scenarios which both consist of 6 subevents at the same epicenters with focal depths and gradually move upward or downward. To have more realistic simulation, we set later subevents having much smaller magnitudes which can imitate the poorer coherency of the waveforms and push this examination more difficult to recover. The focal depth is set from 600 to 645 km. Figure 3.8 shows the recovered 3D BP images of vertical rupture experiments. The combined P- and pP-waves 3D BP images retrieve the epicenters of subevents precisely for both upward and downward rupture tests. The cross-sections (insets of Figure 3.8) demonstrate the



spatial uncertainty of the combined BP images which is reduced significantly comparing with those from P- or pP-wave BP images. As the focal depth, the combined BP images apparently recover the rupture propagation better than the P-only or pP-only BP images do. Whereas, in overall, the P- or pP-wave only MUSIC BP images seem obtain more reliable subevent hypocenters when the propagation direction is against the ray path (Figure 3.8b&f). In other words, the rupture propagating close to the ray path tends to result in stronger smearing effects and less reliability of BP images (Figure 3.8c&e). In more realistic circumstance, it is typical that we only have P-wave to perform BP imaging (Figure 3.8b&e), hence the P-wave BP results achieve acceptable resolution for recovering both the epicenters and focal depths although we will see larger spatial uncertainty for the downward rupture scenario. For the pP-wave BP image, as we expected, it's more un-reliable than the P-wave BP image. Because of more energy decaying in high frequency, the pP-waves holding more lower frequency contents and longer period signals usually suffer stronger swimming and smearing effects (Meng et al., 2012b) which also explains the great uncertainty of pP-wave BP results for the 2013 Okhotsk deep earthquake (Figure 3.4b).

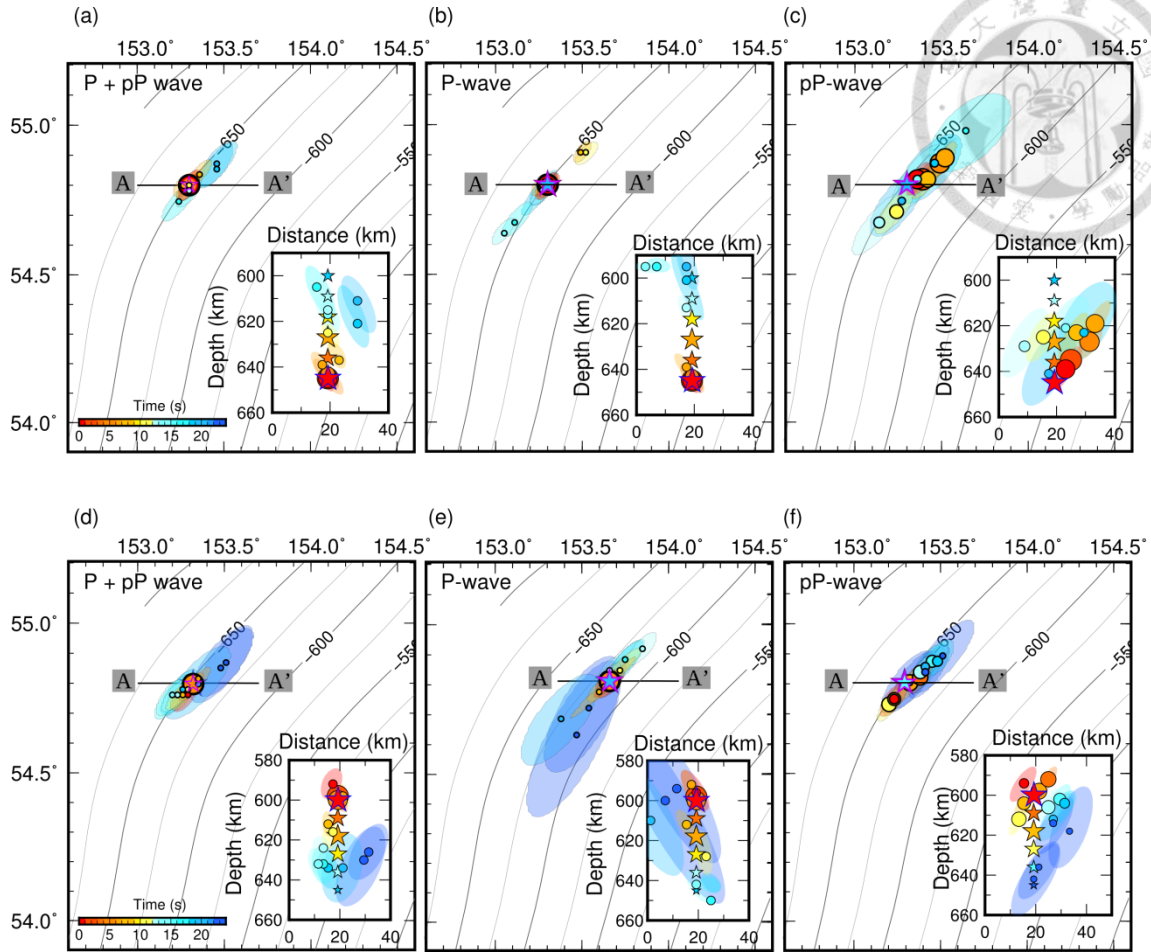
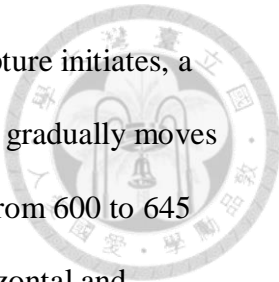


Figure 3.8 Synthetic tests of vertical rupture scenarios.

Map and cross-sections showing the 3D BP results for (a)-(c) downward and (d)-(f) upward rupture scenarios. (a) & (d) show the resultant BP images by combining those obtained by P- and pP-waves, respectively. (b) & (e) are the BP images of P-wave. (c) & (f) are the BP images of pP-wave. The stars showing the subevent hypocenters are colored and scaled by the hypothetical occurrence time after the 1st subevent and with corresponding magnitude. The inset in each figure shows the cross-section along the latitude. The resultant BP images are shown with the symbols the same with those in Figure 3.3.

The second experiment is an overall Southwestern-dipping scenario which is inspired by the high-frequency 3D BP imaging result from EU seismic array (Figure 3.3b). We like to examine whether the NA seismic array is capable to recover this rupture scenario if this is the true 1st rupture propagation of the mainshock. This testing model includes 5 subevents with a rupture speed of 4 km/s. In order to set up more



sophisticated rupture experiment, as shown in Figure 3.9, after the rupture initiates, a smaller subevent located at the north of the epicenter, then the rupture gradually moves to SE-ward direction and the focal depths of subevents also increase from 600 to 645 km at the same time. Figure 3.9a shows great agreements in both horizontal and vertical direction between the presumed and recovered subevents from the combined BP images of P- and pP-waves. As the result from pP-wave only shown in Figure 3.9c, the BP imaging only retrieves reliable initial NE-ward rupture (subevent 1 & 2). The P-wave BP result is overall consistent with the input rupture model although there are few unrealistic source radiators which falls to the range parallel to the source-to-array path. This unavoidable bias accompany with large smearing zone occurs because the BP tends to project those subsequently low coherent wavetrains inside the smearing area which has long axis parallel to the source-to-array path. Similar biases are also observed in the vertical rupture experiment at the end of the rupture (Figure 3.8). In general, disregarding those weak source radiators accompany with large spatial uncertainties, the P-wave BP result retrieves the hypocenters of input subevents correctly including the focal depths (Figure 3.9b). After briefly summery this synthetic test results with the BP imaging of the mainshock from two arrays that we believe NA seismic array should also observe the SE-ward propagation as EU array does if the 2013 Okhotsk deep earthquake do rupture toward SE direction during the 1st rupture stage.

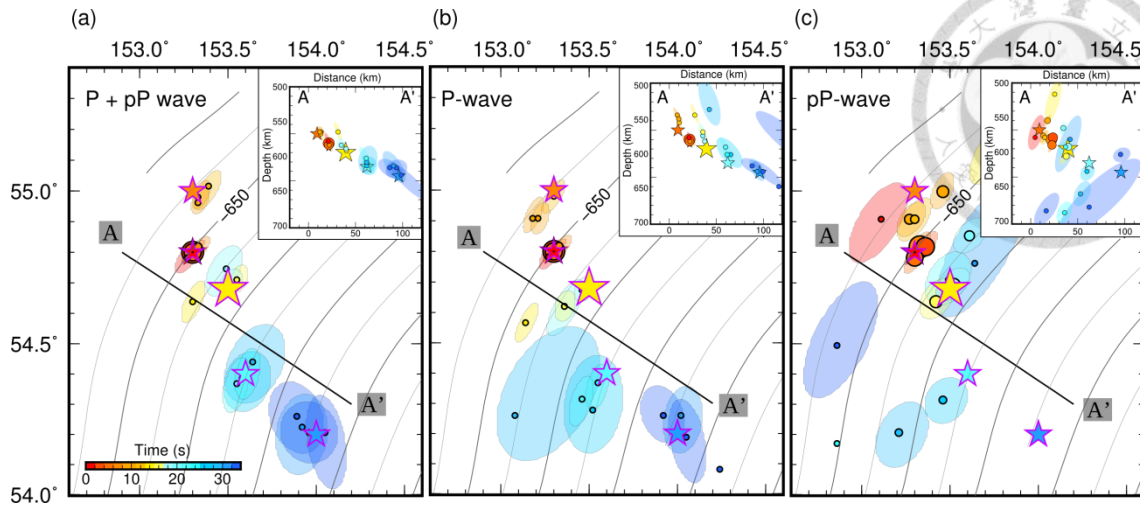


Figure 3.9 Synthetic tests of SE-ward dipping rupture scenario.

The recovered BP image snapshots by (a) combined, (b) P-wave and (c) pP-wave BP images. Insets: the cross-section along the Profile AA'. The symbol configurations are the same as Figure 3.8.

The last synthetic experiment, based on the 3D BP results of the mainshock from NA seismic array, is a complex rupture scenario having total 13 subevents comprising two subhorizontal ruptures against to each other. Figure 3.10a-c shows the BP imaging results from NA seismic array. The first one goes to NE-direction at depth of 609 km and the SSW-ward one propagates at depth of 645 km. As expected, the P-wave BP is capable to recover the input subevent hypocenters well (Figure 3.10b) even though we notice some errors on estimating the focal depth for the initial NE-ward rupture. It's also not surprise to see the BP results of pP-wave having biased radiators recovery for the second SSW-ward rupture (Figure 3.10c) because of strong swimming and smearing effects as discussed earlier. Nevertheless, the integrated BP images of P- and pP-wave (Figure 3.10a) recovered scenario precisely and approved the reliability and stability of the 3D BP images likewise.

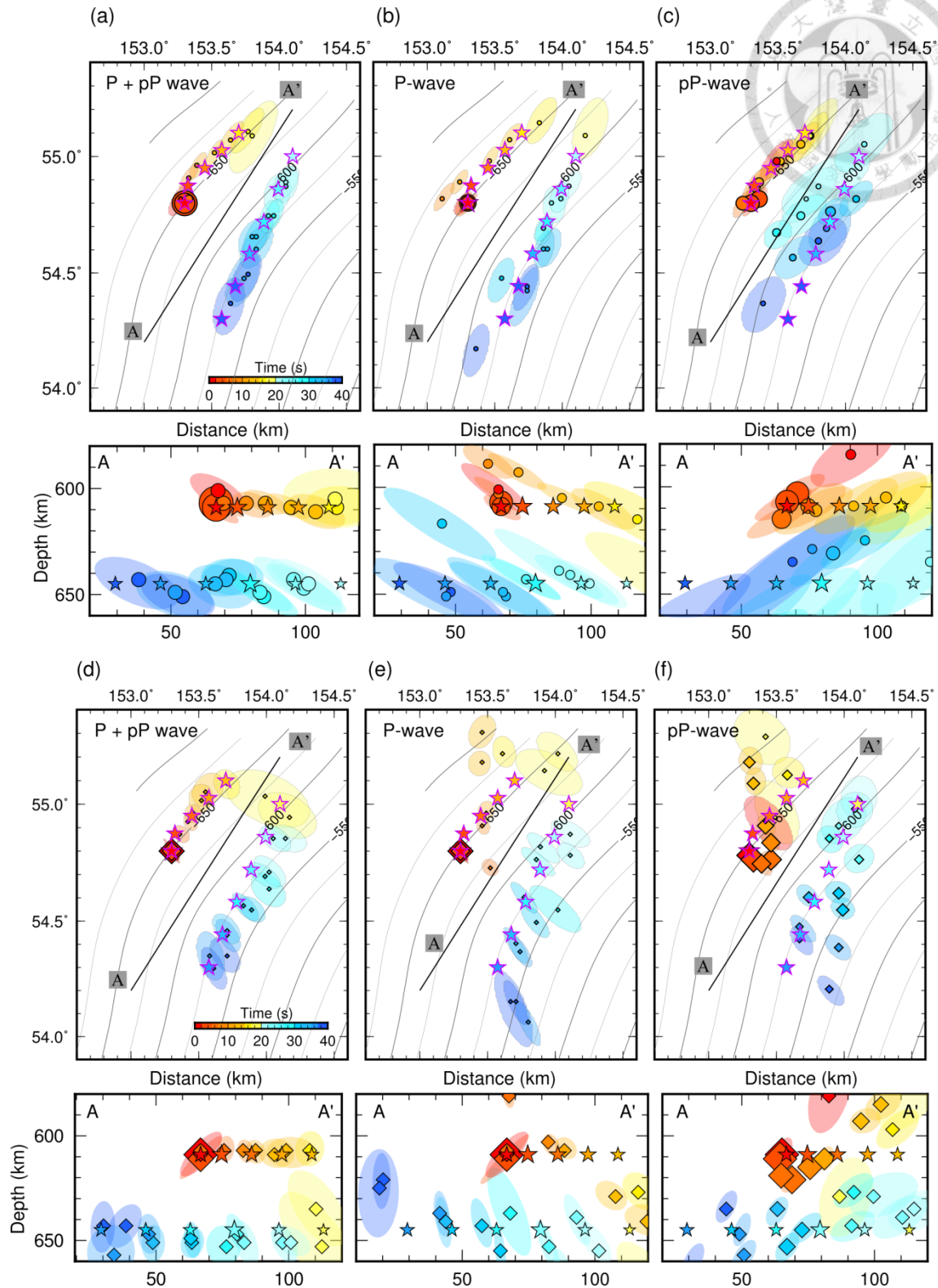


Figure 3.10 Synthetic tests of two-stage anti-parallel rupture scenarios.

Map and cross-sections showing the 3D BP results with circles and diamonds are obtained from the (a)-(c) NA and (d)-(e) EU seismic arrays, respectively. Insets: the cross-section along the Profile AA'.

The layout and symbol configurations are the same as Figure 3.8 & Figure 3.7.

To have cross-reference, we also examine whether the EU seismic array is capable to resolve this anti-parallel rupture scenario (Figure 3.10d-f). Instead of getting the NE-direction propagation of 1st rupture stage, the EU seismic array projects the wavetrains to an East-ward propagation rupture which is literally parallel to the source-to-array (EU) direction. Summarizing the BP results shown in Figure 3.9b and Figure 3.10e, we found one of the disadvantages of BP imaging is the near perpendicular geometry between source-to-array path and rupture propagation. The undesirable geometry perfectly explains the inconsistent 1st rupture stage of 2013 Okhotsk earthquake from NA and EU arrays (Figure 3.3). By our rupture scenario experiments, we are able to confirm that the East-ward propagation of 1st rupture stage observed by EU BP images is deviated from the true rupture propagation.

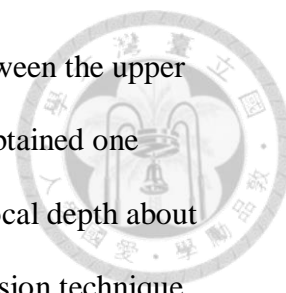
Taking a compressive view of above synthetic experiments (Figure 3.9b & Figure 3.10b), For the late arriving less coherent and weak wavetrains, the BP imaging becomes unstable and tends to back project the energy radiators along the source-to-array path rather than to the true propagation when the rupture direction is nearly perpendicular to the source-to-array path. We believe the biased BP result is related with the less coherent wavetrains, the stronger smearing and swimming effects which are contributed together to make the source energy been projected to the error locations along the ray path. This particular phenomenon could be treated as an important indicator for us to examine and verify the BP images carefully if the tempo-spatial distribution aligns parallel to the ray path. In practical, it's easy to encounter poor geometry of propagation with the ray path when performing the BP. Other than the instability of horizontal locations of subevents, the cross-sections of all

synthetic tests indicate that the focal depths of subevents recovered by combined MUSIC BP images of P- and pP-waves are reliable and stable. For the synthetic results from P-wave only BP images, we also approve the reliability on resolving the focal depth of subevents, even in the circumstance of undesirable geometry between the rupture direction and ray path (Figure 3.9b and Figure 3.10e).

Our synthetic experiments demonstrate the importance of combining P-wave and depth phases BP images to cope with the perpendicular geometry of rupture propagation with the ray path (Figure 3.8~Figure 3.10) and approve the depth difference of two-stage antiparallel subhorizontal ruptures of 2013 Okhotsk mainshock and fast subvertical ruptures of two aftershocks.

3.6 Discussions

The BP results of 2013 Okhotsk deep earthquake sequence are summarized in the Figure 3.11. As the mainshock, the integrated P- and pP-waves 3D BP images suggest that this most recent largest deep earthquake consisted of two subhorizontal ruptures toward the opposite directions. The en-echelon like anti-parallel ruptures separate at least 10~15 km in depth as the cross-sections show in Figure 3.12. Other than that, based on the focal depth of aftershocks collected from the ISC catalog (International Seismological Centre, 2015) and relocated by Chen et al. (2014) could be divided into two groups. The shallower aftershock group roughly has comparable focal depth of the mainshock; whereas there is another deeper group near the terminus of the 2nd S-ward rupture. The Figure 3.12 demonstrates the coincident distribution of the 3D BP results



of mainshock and the aftershocks. The depth aperture of ~15 km between the upper and lower rupture zone is also observed by Chen et al. (2014) who obtained one subevent starting at 12 s after the earthquake nucleated and having focal depth about 16.7 km deeper than hypocenter by using multiple point source inversion technique. The 3D BP results and the aftershocks distributions clarify that the rupture process of great 2013 Okhotsk deep earthquake consists two subhorizontal shear zones. The paired shear ruptures have been observed in other large deep earthquakes. For example, Chen et al. (1996) utilized the P and SH waveform inversion method and discovered the “en-chelon” rupture feature for several large deep earthquakes such as the 1994 great Bolivia earthquake and the 1994 Japan deep earthquake. Moreover, the deep earthquakes showing double rupture zones are also observed in Tonga, Izo-bonin subduction zones (Furukawa, 1994; Iidaka and Furukawa, 1994; Wiens et al., 1994).

For the 2013 Okhotsk mainshock, the 3D BP results also revealed different rupture speeds of two-stages of en-chelon like anti-parallel ruptures. The 1st NE-ward rupture almost reaches the northern edge of the Pacific slab and propagates in much slower velocity (~0.64Vs) than the 2nd S-ward rupture stage and two aftershocks (>0.82Vs). Varying rupture speeds along different section of the same subducting plate implies the importance of the slab temperature which might affect the earthquake rupture behaviors, because the northernmost slab edge is believed to be warmed by both the ambient mantle and corner asthenosphere flow (Peyton et al., 2001; Park et al., 2002; Davaille and Lees, 2004a). The shorter NE-ward rupture length also denotes the northern terminus of the seismogenic zone inside the subducting Pacific slab.

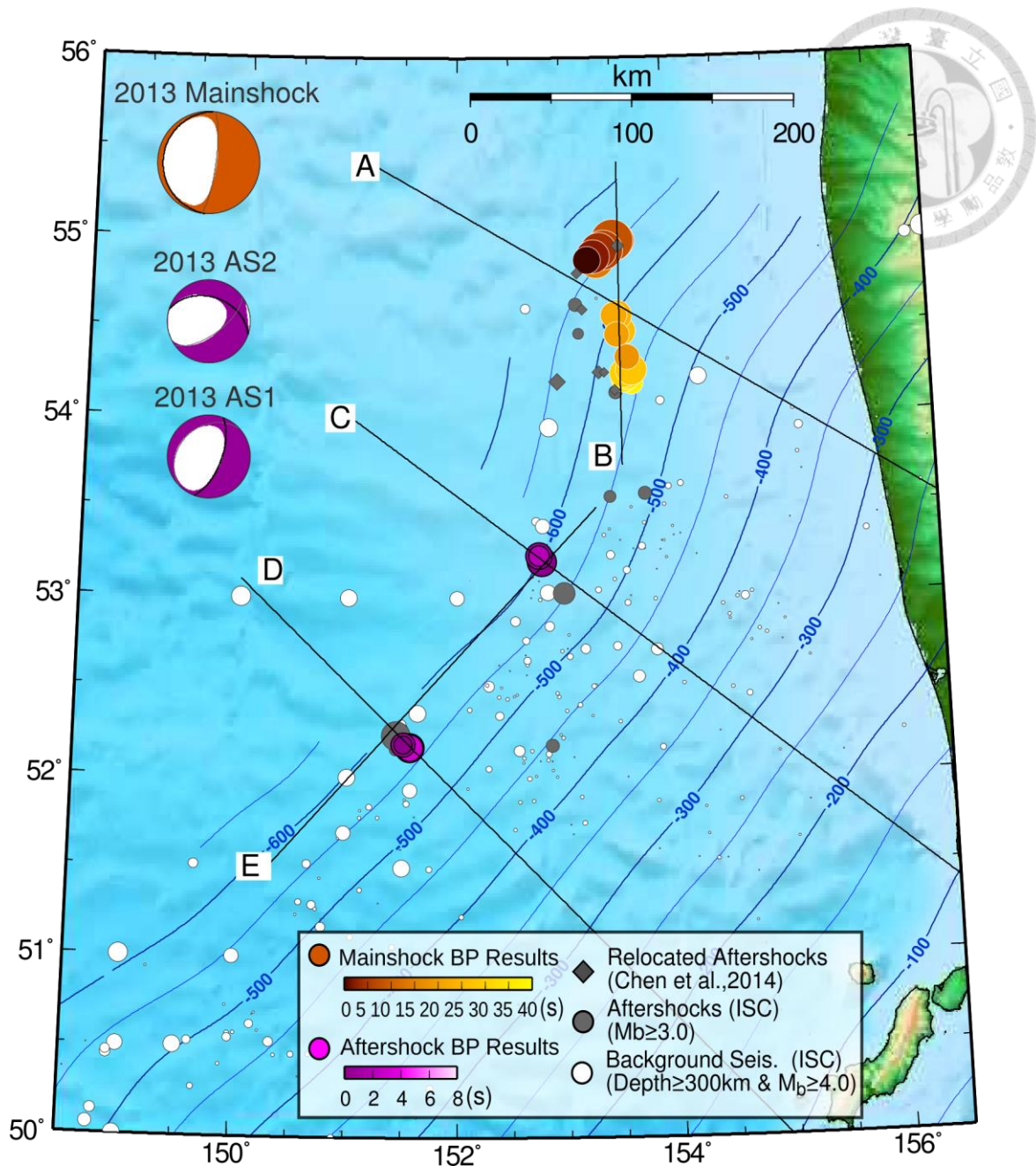


Figure 3.11 The tectonic setting of northern Kuril subduction zone and the BP imaging results of 2013 great Okhotsk deep earthquake sequence, including the mainshock and two largest aftershocks.

The rupture propagations for mainshock and two aftershocks are shown in circles with brownish and purplish color-bars. The colors and sizes of the circles represent the elapsed time after the onset of P-wave and the pseudo-spectrum power of BP images. The rupture fault planes of mainshock and aftershocks are highlighted by thick lines in beach balls reported by the Global CMT solutions. Gray circles are the aftershocks in 6 month after mainshock. Gray diamonds show the relocated aftershocks done by Chen et al., 2014. The white circles show the background seismicity since 1900. The blue contours are the slab contours of the subducting Pacific Sea Plate from slab 1.0 model.

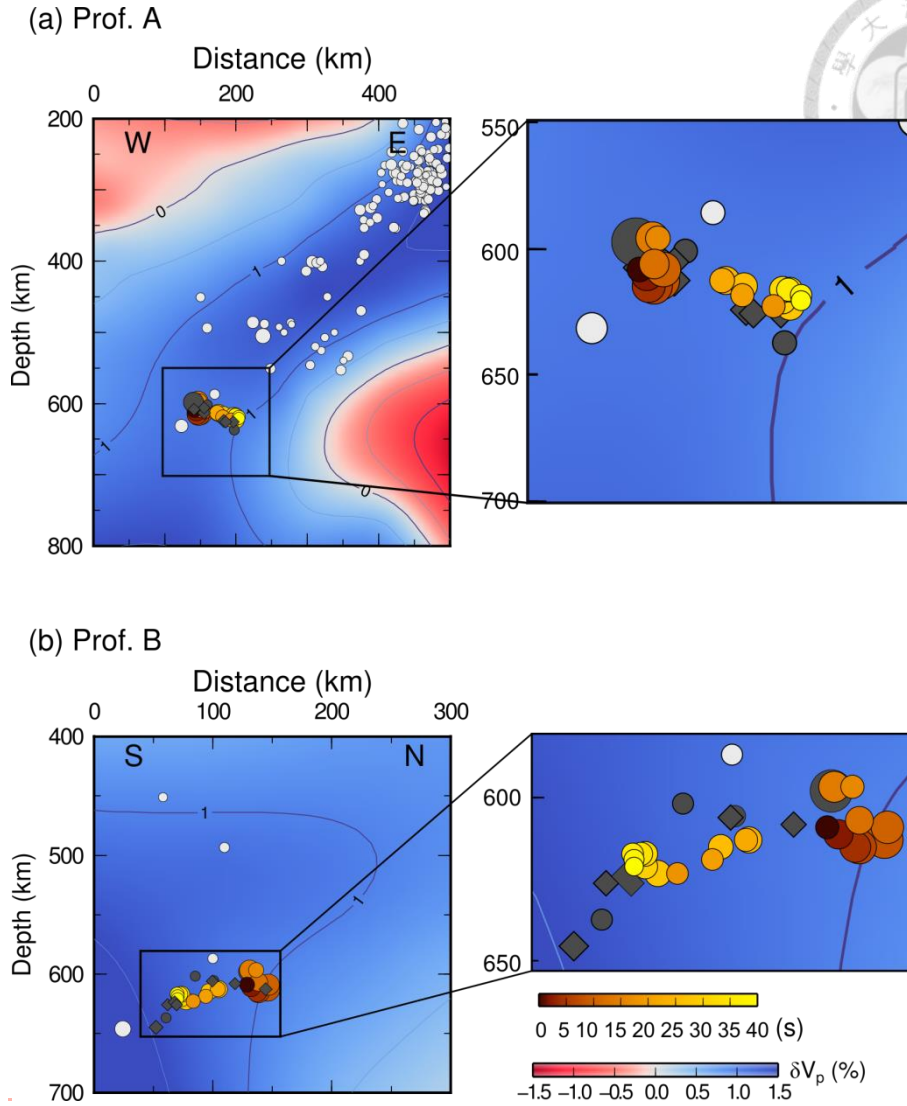
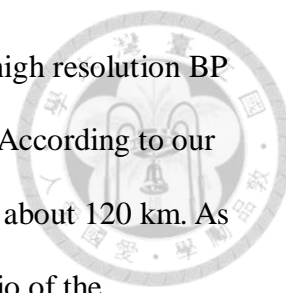


Figure 3.12 Cross-sections of the 3D BP results of 2013 Okhotsk mainshock.

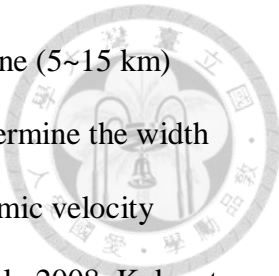
Cross-sections along the profiles parallel to the (a) subduction direction (AA') and (b) slab contour (BB') as indicated in Figure 3.11. Right panels show the enlarge part of the cross-sections. The background image are the P wave tomography from Fukao and Obayashi (2013). The symbols configurations are the same with those in Figure 3.11.

When an earthquake occurred, the static stress drop could be estimated directly with the confidential rupture length, width of the rupture plane and seismic moment. According to Starr (1928), the stress drop of a buried dip slip fault is given by $\Delta\sigma = 16M_0/(3\pi SW)$, where M_0 , S and W are the seismic moment, fault area and rupture width respectively. The BP imaging represents the spatiotemporal slip



distribution on the fault plane (Fukahata et al., 2014). Therefore the high resolution BP imaging has confidential estimation on the minimum rupture length. According to our 3D BP results, the total rupture length of two anti-parallel ruptures is about 120 km. As the rupture width, it can be roughly assumed by setting the aspect ratio of the rectangular fault plane from 0.1 to 1.0 to obtain the exaggerated range of stress drop estimations. For aspect ratio of 0.1 and 1; the stress drop are 344 and 3.44 MPa, respectively. By taking the seismogenic width of 40~60 km simulated by numerical modeling of rheological structure of subducted oceanic plate (Karato et al., 2001) as the rupture width approximation, then the static stress drop ranges from 31 to 13 MPa for width. Further compare with the result from teleseismic frequency spectrum analysis, Ye et al. (2013) suggested the stress drop is about 12~15 MPa which is close to the estimation by setting the rupture width of 60 km.

The global slab geometry model, the slab 1.0 (Hayes et al., 2012), optimized by the seismicity may have some uncertainties on sketching the slab geometry for the regions having rare deep-focus seismicity, such as the northern part of Kuril subduction zone. As shown in the cross-sections of Figure 3.3 and Figure 3.12, the 2013 Okhotsk mainshock nucleated outside the slab boundary of slab1.0 model. The high P-wave speed anomaly from the tomographic images by Fukao and Obayashi (2013) illuminates the colder subducted Pacific plate (Figure 3.12) clearly. Due to the limited resolution of the tomography image, the metastable olivine wedge inside the slab could not be discernible here. According to the thermo-kinetic subduction models proposed by Mosenfelder et al. (2001), the maximum depth of the olivine metastable tip should be less than 600 km if the subducting plate having thermal parameters of 4000 to 6000 K. Moreover, the numerical modeling for olivine-spinel transformation



(Marone and Liu, 1997) suggested an extreme narrow seismogenic zone (5~15 km) outside the olivine metastable wedge. Several studies also tried to determine the width and extension depth of metastable olivine wedge by detecting the seismic velocity anomalies (Koper and Wiens, 2000; Kaneshima et al., 2007; Jiang et al., 2008; Kubo et al., 2009; Kawakatsu and Yoshioka, 2011). However, the rupture area estimated by our 3D BP images indicates that 2013 Okhotsk mainshock ruptures beyond the entire metastable wedge and implies that thermal shear instability remains the most plausible mechanism of 2013 Okhotsk deep earthquake.

The triggering of deep earthquakes at great distances has been observed in several subduction systems including Tonga, Japan and Bolivia (Myers et al., 1995; Tibi et al., 2003a, 2003b). The first aftershock “2013AS1” was also dynamic-triggered because of the static stress decreases to only 0.08 MPa by the assumption that two-stage ruptures have equal moment magnitude. Dynamic stress triggering induced by maximum passing seismic wavefields has been proposed to explain the triggered earthquake at great distance for both shallow and deep earthquakes (Kilb et al., 2000; Tibi et al., 2003a). The dynamic stress disturbance may supply the extra stress or pressure at the region facilitating the nucleation of earthquakes. However, much longer delay times of the triggered events do not accommodate with the travel times of the passing seismic wavefields. The first M_w 6.7 aftershock, “2013AS1”, located 300 km away in south was triggered in only 9 hours; however the second one half way close to the mainshock occurred after 4 months. We suspect great different time delays responding to the dynamic stress disturbance of two aftershocks is more related to the ambient seismogenic circumstance than the distance to mainshock or the stress changes inherited from the mainshock. As the cross-sections shown in Figure 3.13, the

background seismicity in the north (prof. C) is higher than in the south (prof. D). The event “2013AS1” locates in the vicinity with lower seismicity where may have accumulated vulnerable stress and closed to a more critical circumstance to nucleate earthquake as soon as the area inherits the stress disturbance. Other than the background seismicity, the variation of thermal structure along the deepest part of the subducting slab may also affect the response time to the stress; however more seismological observations, dynamic rupture models and slab geodynamic simulations are necessary for further examinations.

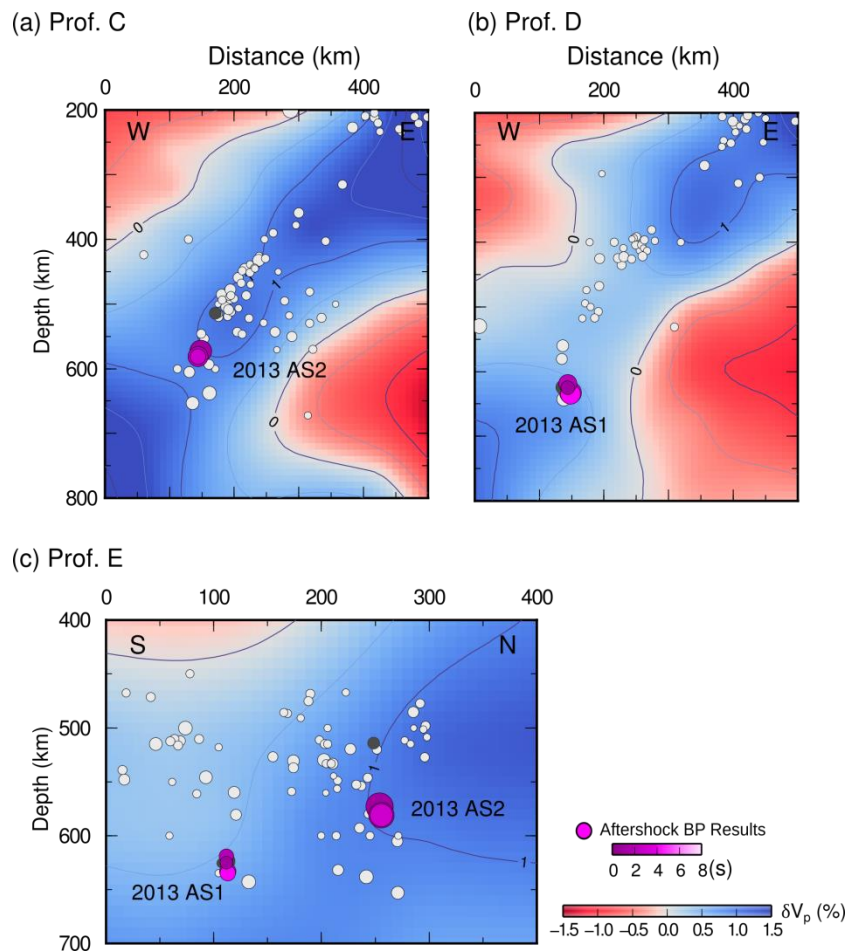


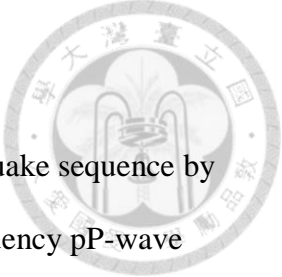
Figure 3.13 Cross-sections of the 3D BP results of two aftershocks.

Cross-sections along the profiles of (a) C, (b) D and (c) E as shown in Figure 3.11. The background

image and symbol configurations are the same with those in Figure 3.11 and Figure 3.12.



3.7 Conclusions

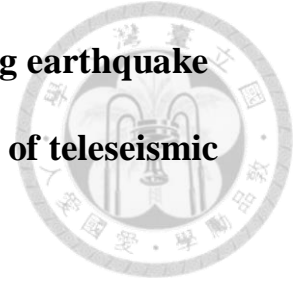


We revealed the rupture properties of 2013 Okhotsk deep earthquake sequence by applying the 3D MUSIC BP method. As the mainshock, the low-frequency pP-wave BP image is integrated to the P-wave BP images to ascertain the focal depth difference between two-stage en-echelon rupture feature. We also found both largest aftershock rupture downward in fast rupture speed. In summary, along the same subduction plate, we observe two different rupture speeds: the slow NE-ward rupture of mainshock and the fast 2nd rupture stage of mainshock and two aftershocks. The significant variation of rupture speeds in the subducting Pacific slab suggests the difference of thermal structure along deepest part of the slab. Also the NE-ward rupture may reach the terminus of the seismogenic zone of the norther tip of the slab which is warmed by the ambient mantle and asthenosphere corner flow.

We also perform a suit of earthquake rupture model tests to assure the reliability of the 3D BP images and approve the capability on diminishing the smearing effects by adding the P-wave and pP-wave BP images.

Despite of the fact that aftershock 2013AS1 located far from the mainshock in the central part of Kuril, it is triggered much faster than the other closed aftershock 2013AS2. The response time to the dynamic stress perturbation induced by the mainshock seems related with the backgrounds seismicity around two aftershocks or the pressure-temperature distribution inside the slab which need to be examined further by geodynamic or earthquake rupture dynamic simulations.

Chapter 4 Rupture characteristics of the 2016 Meinong earthquake revealed by the back-projection and directivity analysis of teleseismic broadband waveforms

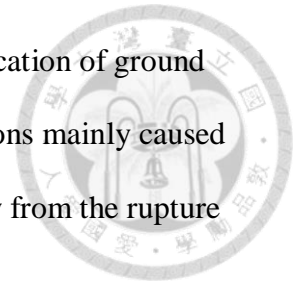


Originally published in Jian, P.-R., S.-H. Hung, L. Meng, and D. Sun (2017). Rupture characteristics of the 2016 Meinong earthquake revealed by the back projection and directivity analysis of teleseismic broadband waveforms, *Geophys. Res. Lett.*, **44**,no.8, 3545–3553, doi: 10.1002/2017gl072552.

4.1 Abstract

The 2016 Mw 6.4 Meinong earthquake struck a previously unrecognized fault zone in mid crust beneath south Taiwan and inflicted heavy casualties in the populated Tainan City about 30 km northwest of the epicenter. Because of its relatively short rupture duration and P wave trains contaminated by large-amplitude depth phases and reverberations generated in the source region, accurate characterization of the rupture process and source properties for such a shallow strong earthquake remains challenging. Here we present a first high-resolution MUSIC back-projection source image using both P and depth-phase sP waves recorded at two large and dense arrays to understand the source behavior and consequent hazards of this peculiar catastrophic event. The results further corroborated by the directivity analysis indicate a unilateral rupture propagating northwestward and slightly downward on the shallow NE-dipping fault plane. The source radiation process is primarily characterized by one single-peak, ~7 s duration, with a total rupture length of ~17 km and average rupture speed of 2.4 km/s. The rupture terminated immediately east of the prominent off-fault aftershock

cluster about 20 km northwest of the hypocenter. Synergistic amplification of ground shaking by the directivity and strong excitation of sP and reverberations mainly caused the destruction concentrated in the area further to the northwest away from the rupture zone.



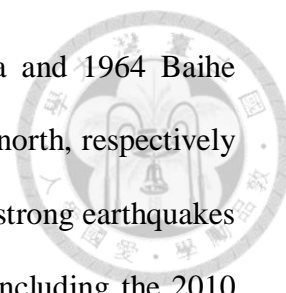
4.2 Introduction

On Feb. 5, 2016, a strong devastating earthquake with a moment magnitude (M_w) 6.4 struck the Meinong District of Kaohsiung City in southern Taiwan. The Central Weather Bureau (CWB) of Taiwan located the earthquake hypocenter at a mid-crust depth of 16.7 km beneath the northern tip of the Pingtung plain, the region covered with the Quaternary alluvial deposits and bounded by the two major faults, the N-S striking Chaochou fault to the east and the NE-SW striking Chishan fault to the west (

Figure 4.1). The USGS CMT (centroid moment tensor) solution of the main shock and distribution of its aftershocks reported by the CWB suggest that the earthquake slipped on a shallow NE-dipping fault plane striking $N61^\circ W$ with both left-lateral strike-slip and thrust motions (

Figure 4.1). Amplification of ground motion by sediment reverberations coupled with local site effects have been blamed for partly causing the collapse of high-rise buildings and severe fatalities in Tainan City, about 20 km northwest of the epicenter.

For the last nearly three centuries, several historically-documented events with similar or larger magnitudes had rattled the Tainan area which also resulted in substantial damages and casualties. The two recent ones occurring in very close



proximity to the 2016 Meinong earthquake are the 1946 Hsinhua and 1964 Baihe earthquake located about 40 km to the northwest and 30 km to the north, respectively (Cheng and Yeh, 1989). After about 45 years of seismic quiescence, strong earthquakes with magnitude greater than 6 started to reactivate in the vicinity, including the 2010 Mw 6.2 Jiashian and 2012 Mw 6.3 Wutai earthquake that struck 25-30 km deep east and southeast of Meinong on the blind faults beneath the southern Central Mountain Range (Hsu et al., 2011a; Chan and Wu, 2012; Lee et al., 2013). As revealed by the earthquakes in 1990-2015 from the CWB catalog, the Meinong event occurred in a NW-SE trending linear zone of background seismicity with no clear link to any known faults. This linear feature delineates the boundary between the seismically active, rugged hilly terrain to the north and east and the Pingtung Plain to the south with extremely low seismicity. Two prominent aftershock clusters were triggered near the source region within hours to days after the main shock. The one nearest to the hypocenter was distributed at 10-20 km depth along the linear background seismic zone as mentioned above and the other more concentrated deeper at 20-30 km depth to the WNW about 20-30 km from the source. These two clusters appear to be aligned on a NW-SE trend parallel to the strike of one of the nodal planes inferred from the CMT of the main shock, but separated by a seismic gap in between. Additionally, fewer aftershocks, in spite of being quite sparse and scattered, seem to run roughly parallel to the strike of the other nodal plane (N174°E) and steep topographic front.

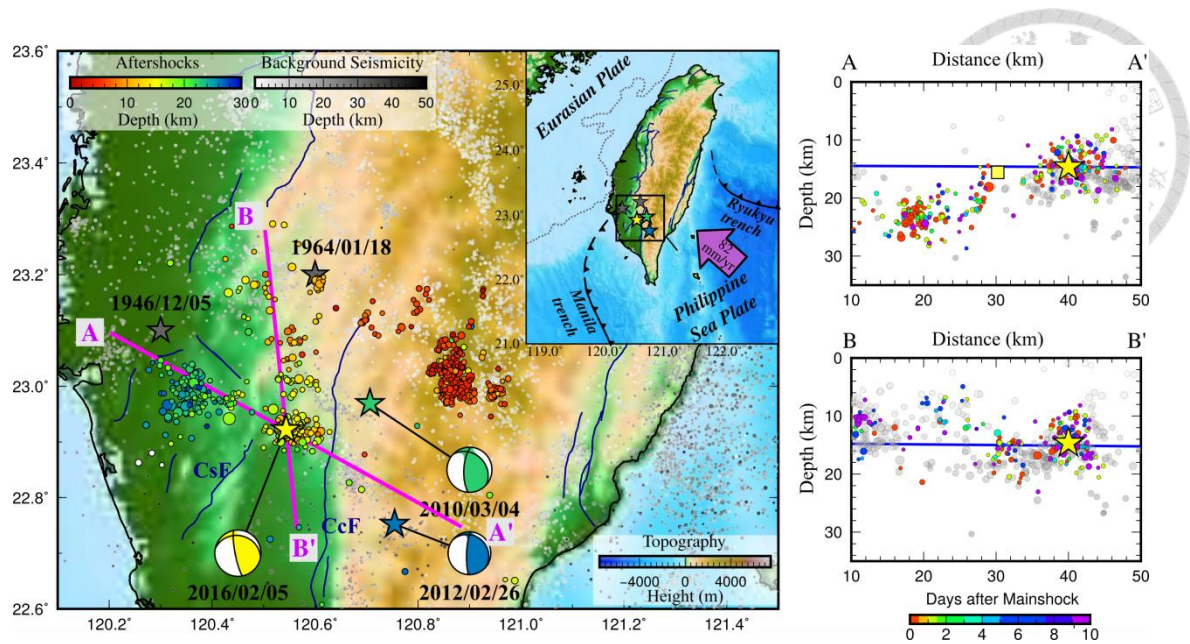


Figure 4.1 Tectonic settings of Meinong earthquake and the profiles showing BP results and aftershock distributions.

(a) Tectonic setting of the Meinong earthquake outlined by a black box in the inset map showing the plate configuration around Taiwan. Stars show earthquakes with $M_w > 6.0$ recorded in this area during the instrumentation era, with the focal mechanisms from the BATS database. Color and gray circles denote the aftershocks within 10 days after the mainshock and background seismicity with $M_L > 2.0$ from the CWB catalog, with size and color scaled by magnitude and depth, respectively. (c) Projection of all the earthquakes located within 5 km on either side of the AA' and BB' cross sections parallel to the strikes of the two nodal planes shown in (a), where yellow star and square mark the hypocenter and terminus of the rupture from our BP image.

In spite that the fault plane orientation, average slip vector, and rupture area of an earthquake can be crudely determined from the CMT mechanism, aftershocks, and surface field observations, tracking the details of the rupture process is of essential importance for comprehensively understanding the source characteristics and consequent impacts of a destructive event. A back-projection (BP) method using high-frequency (HF) teleseismic body waves recorded at large-aperture dense arrays is well suited for this purpose, as it has been demonstrated effective in imaging the space-time evolution of radiated energy with no need of much a priori knowledge

about source parameters (Ishii et al., 2007). Here, we employ the multitaper-MUSIC BP technique (Meng et al., 2011) to illuminate coherent radiation sources through time for tracking the rupture process of the Meinong earthquake. The obtained image would facilitate the identification of the asperity on the previously unknown fault zone and estimation of important source parameters such as rupture speed, length, and direction. Using broadband waveforms recorded globally and modelled synthetics, we further verify our BP results through the directivity and source radiation analyses.

4.3 Methods and data

In principle, the BP method tracks the rupture front of an earthquake by extracting coherent seismic arrivals radiated from common source points and propagating them backward in time to the positions of the respective radiators (Ishii et al., 2007; Koper et al., 2011). Practically, there are various ways to perform the reverse-time source imaging, such as the time-domain stacking (Ishii et al., 2007), frequency-domain compressive sensing (Yao et al., 2011) and MUSIC (Multiple Signal Classification) (Meng et al., 2011). Because a seismic signal is inherently nonstationary and there exists a tradeoff between its arrival time and traveling distance, the drift of the stacked energy over time toward the direction to the array is inevitable for the BP results (Ishii et al., 2007; Koper et al., 2011; Yao et al., 2011). This so-called swimming artifact can be much mitigated by the MUSIC to enhance the image resolution (Meng et al., 2012b). The method estimates the covariance matrix of waveforms for every sliding time window and sampling frequency by a multitaper approach (Thomson, 1982) and

project it into the signal and noise subspace (Schmidt, 1986). The steering vector consists of the frequency-domain phase shifts at each station to correct for the arrival-time shifts of the signals from each candidate source relative to the hypocenter. The direction of arrival (DOA) associated with the strongest radiator is determined by the maximum amplitude of the frequency-average MUSIC pseudospectrum, defined as the inverse of the projection of the steering vector onto the noise subspace (Meng et al., 2011).

In this study, we combine the high-resolution MUSIC BP and directivity analysis to explore the rupture process of the Meinong earthquake in details using global teleseismic broadband records. The vertical velocity waveforms filtered at 0.5-1.5 Hz from two large and dense seismic networks in Europe (EU) and Australia (AU) are first aligned on the initial P arrivals as the onset (zero time) of the rupture (Figure A1). By choosing overlapping sliding windows of appropriate length, we perform the multitaper cross-spectral estimation of the windowed signals for the subspace projection analysis. Nodes of a $50 \times 50 \text{ km}^2$ grid mesh centered at the hypocenter with a 2-km spacing along the strike and dip of the presumed fault plane are specified as candidate source radiators. We test two plausible scenarios of the rupture propagating on either one of two conjugate nodal planes derived from the USGS CMT. The results favor the shallow NE-dipping one striking $N61^\circ W$ as the rupture plane.

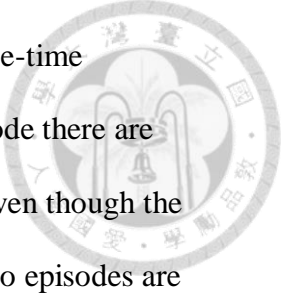
4.4 Back projection source image

Figure 4.2 summaries our BP results using P and depth phase sP wave trains from

the AU and EU array. We test different lengths of the sliding window shifted in every second and choose 3 s, about twice of the dominant period of the filtered P pulses, to achieve both the optimal time resolution and stability of the BP images. The rupture process is illuminated by the strongest radiators in every 2 s projected on the map. The respective peak amplitude of the MUSIC pseudospectrum varying with time is also shown as the apparent source time function, similar to the maximum amplitude of the stacked energy obtained in the time-domain BP method.

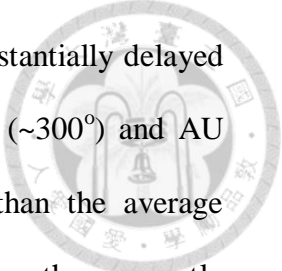
In Figure 4.2 (a), we show the BP results obtained with ~20-s long wave trains starting from the aligned P arrivals. The MUSIC pseudospectrum observed at the AU and EU array grossly resembles the displacement waveforms shown in Figure 4.3(b), indicating two major episodes of source energy release. Each episode begins with a ~5-7 s long, stronger radiation burst followed by a rapid decay afterwards, but the peak and duration observed from the AU array appear later and longer by about 2 s than those from the EU array. In the first episode, except for the last 2-3 s during which the normalized amplitude of the MUSIC pseudospectrum at the EU drops rapidly to very small values (<-3 dB), the radiators seen by both the arrays show the predominance of a unilateral rupture propagating primarily toward the NW and slightly down-dip. Though the AU compared to the EU array has a less dense station coverage, the shorter epicentral distance and favorable azimuth opposite to the rupture direction lead to the recorded waveforms having longer duration and higher coherence and signal-to-noise ratios. The AU image thus gives preferable spatiotemporal resolution for more robust estimates of the rupture length, speed, direction and duration. The following investigation of the main rupture features mostly rely on the AU results.

Despite some minute differences probably due to the source radiation pattern and



directivity effect, the overall HF radiators reveal fairly consistent space-time distributions during the first 5-8 s. In contrast, during the second episode there are large discrepancies in the radiator locations between the two arrays, even though the apparent source time functions and displacement waveforms of the two episodes are similar. The EU radiators emitted between 10 and 14 s are found to move further northwest about 20 km from the epicenter and ~5-10 km above the deeper off-fault aftershock cluster, while the AU radiators are shifted eastward in the reverse direction to the previously ruptured area. We notice that these inconsistent radiators are mainly back projected from the second major pulses which have the arrival-time moveouts and amplitudes comparable to the first ones (Figure 4.3b). Considering the hypocentral depth of ~16 km and relative short rupture duration typical for the Mw6.4 event, we speculate these late-arriving pulses originate from the surface-reflected depth phases, pP and sP.

To corroborate this speculation, we manually pick the onset times and peak amplitudes of the pP and sP phases on the vertical velocity seismograms filtered at 0.01-2 Hz (Figure 4.3a). The corresponding 1-D synthetic seismograms are calculated by the frequency-wavenumber (FK) method (Zhu and Rivera, 2002) assuming a point source with the USGS CMT focal mechanism and CWB located hypocenter (Figure A2). The observed differential sP-P and pP-P times and amplitude sP/pP ratios are then compared with those predicted by the synthetics. As long as the ratio of P to S velocity does not vary significantly, the traveltime difference between sP and pP with similar ray paths is not susceptible to shallow velocity structures near the source and can be used to constrain the focal depth. The average differential sP-pP time from our picking is 2.27 s consistent with the reported depth of ~17 km. Compared to those predicted by



the global IASP91 model, the observed sP-P and pP-P times are substantially delayed by 2-2.4 s. Besides, the sP phases observed at the azimuth of EU ($\sim 300^\circ$) and AU ($\sim 140^\circ$) stations persistently arrive earlier and later respectively than the average picked time of ~ 10 s after P. These arrival-time changes with azimuth are mostly ascribed to lateral velocity heterogeneity around the hypocenter. The 3-D local tomography model (Huang et al., 2014) indicates that the earthquake occurs in the mid crust overlain by a 10-15 km thick sedimentary layer with low P- and S-wave velocities and in transition to a relatively faster upper crust to the east beneath the southcentral mountain range (Figure A3). To reconcile the average ~ 2 -s delay of the observed depth phase arrivals, we replace the crustal velocity model in IASP91 by the layer-averaged tomography model and vary the velocities in the upper and middle crustal layers. We find the average P and S velocities have to be respectively reduced by $16 \pm 4\%$ and $7 \pm 7\%$ relative to the 1-D local model (Figure 4.3c). The radiated seismic energy propagating through the shallow low-velocity layer generate strong reverberations seen at all the stations, with slowly decaying amplitude and long duration over 10 s emerging after the sP (Figure 4.3a). As the amplitudes of high-frequency waves are strongly influenced by scattering from heterogeneity, the observed sP/pP ratios exhibit considerable scattered variations with azimuth unmodelled by the 1-D synthetics. Despite this, the amplitudes estimated from the 1-D synthetics can properly predict the large, less scattered ratios observed in the NE and SE azimuths, where the pP and sP waves travel eastward through the upper crust covered with less sediments.

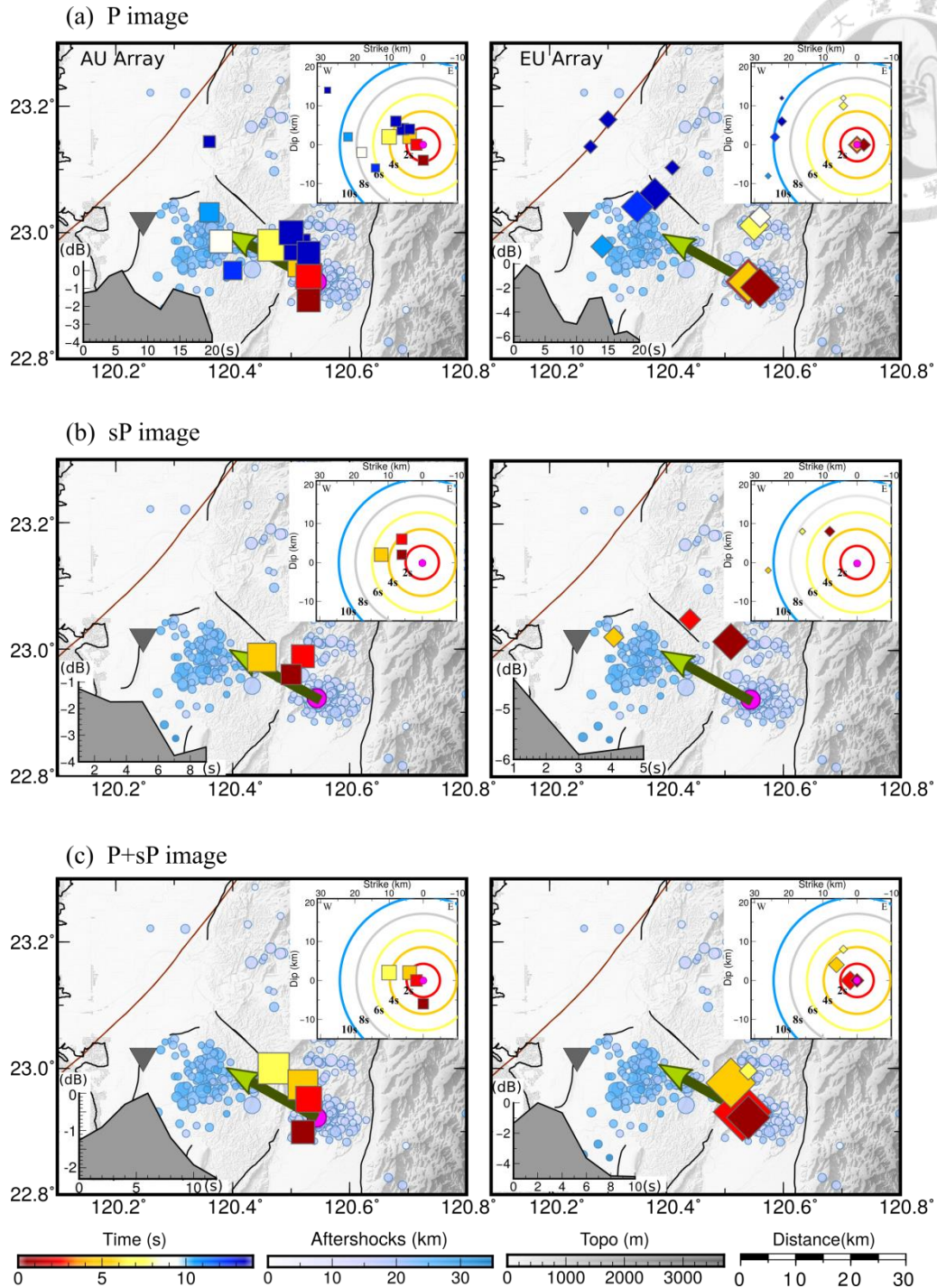


Figure 4.2 The resulting BP images from the AU and EU seismic array.

Spatiotemporal distributions of the strongest radiators imaged with the MUSIC BP using (a) ~20 s P, (b) ~6 s sP, and (c) both P and sP waves at the AU (square) and EU (diamond) array, with symbol size and color scaled by the radiation strength and time elapsed. Green arrows show the rupture direction and length from the directivity analysis, and inverted triangles the most damaged Tainan area. Upper inset shows the distances of the radiators from the hypocenter along the strike and dip, with concentric circles

for the rupture fronts at specific times assuming a rupture speed of 2.5 km/sec.

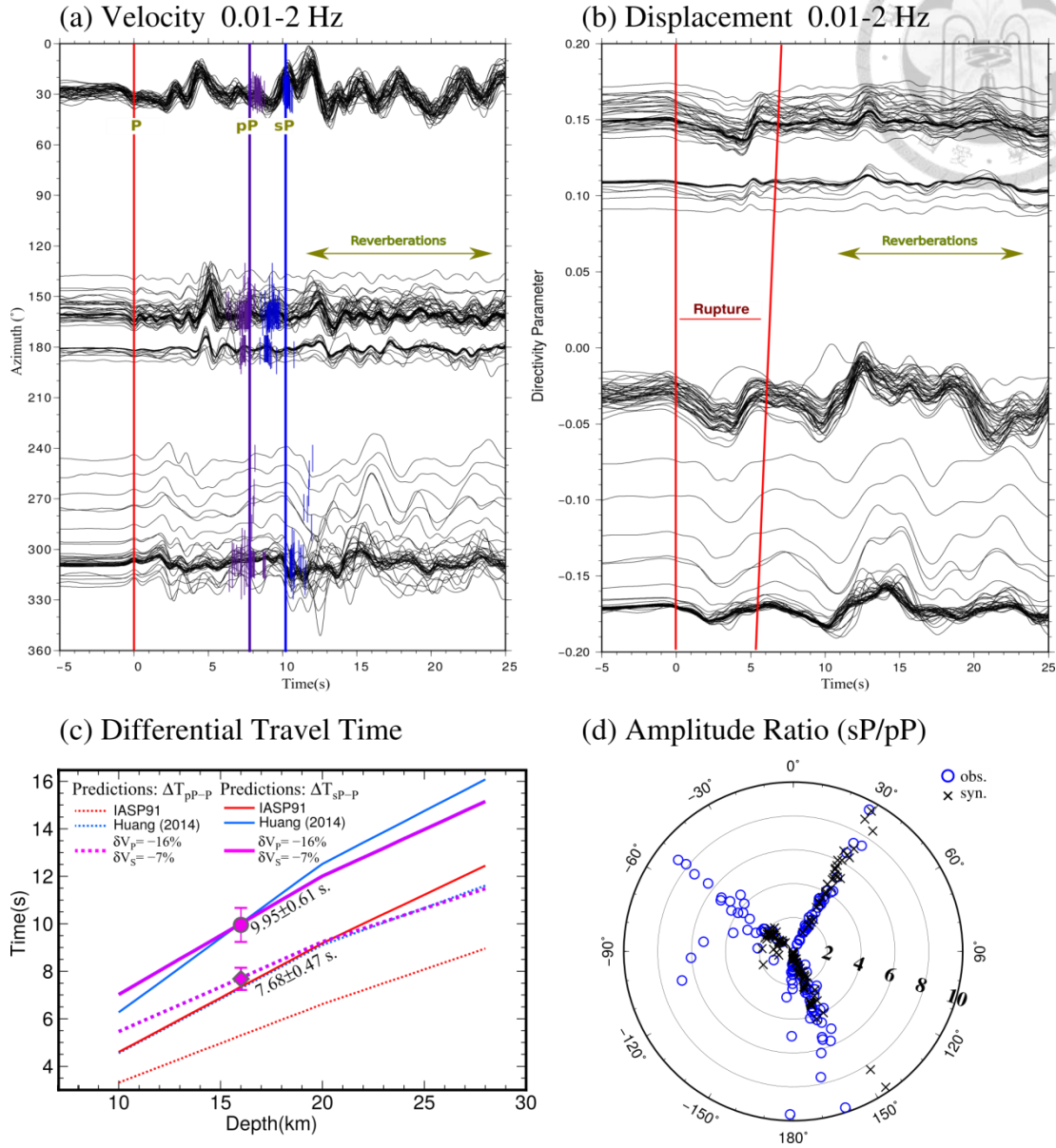


Figure 4.3 Teleseismic waveforms, travel time differences between depth phases and P arrivals and the amplitude ratio of pP/sP.

(a) Teleseismic velocity waveforms at 0.01-2 Hz varying with azimuth. The red, purple and blue lines mark the aligned P and average hand-picked pP and sP arrivals (thin bars), respectively. (b) Displacement waveforms varying with directivity parameter, with the rupture duration marked by red lines. Note that the positive P-wave polarity has been reversed. (c) Differential pP-P and sP-P traveltimes varying with focal depth. The red, blue, and pink lines indicate the pP-P and sP-P times predicted for three 1-D models from IASP91, the local tomography model (Huang et al., 2014), and our estimates that fit the observed differential times for a 16-km deep event. Circles with error bars show the averages and standard deviations of the picked pP-P and sP-P times. (d) Comparison of the observed

(circle) and predicted (cross) sP/pP amplitude ratios varying with azimuth.

As we confirm the phase arriving at ~10 s after P is mainly the sP, we separate these two phases and synchronize their respective onset times to conduct the BP imaging individually. The time-evolving radiators constrained from the P and sP waves at the AU array are consistent. The sP waves propagating northwest through the very thick low-velocity layer to the EU stations and more contaminated by reverberations are less coherent, resulting in the much weaker radiators. Even so, compared to those using the longer P wave trains mixed with the depth phases, the rupture patterns obtained with the sP only at the two arrays become more consistent with each other (Figure 4.2b).

From the previous study (Kiser et al., 2011a) and our exercises using both the observed and synthetic data, combining the BP results from multiple phases with different take-off angles can help improve the image resolution and reduce the uncertainties of the radiator locations for further evaluation of the rupture parameters (Figure A4). In Figure 4.2 (c), we integrate the P and sP obtained rupture images by summing linearly the amplitudes of the respective MUSIC pseudospectrum for each candidate source and given time interval. Those at which the summed amplitudes reach the maxima are identified as the strongest radiators and the corresponding peak amplitudes of the MUSIC pseudospectrum as the apparent source time function (Figure 4.2 c). The summed AU image indicates that the rupture is initially stagnant nearest the hypocenter at 0-2 s, then propagates toward the northwest and slightly downdip between 2 and 6 s, and turns more horizontally at 6-8 s. This rupture scenario agrees with the aftershock distribution in the vicinity of the hypocenter which forms a linear trend roughly parallel to the strike of the rupture plane (

Figure 4.1b). The rupture extent spans about 10 km along the strike and 7 km along the downdip direction and ends at the eastern periphery of the off-fault aftershock zone located ~20-25 km northwest of the epicenter. The average rupture speed is about 2.4 km/s by taking a total rupture length of ~17 km and duration of ~7 s.

4.5 Rupture directivity and source radiation analysis

To further verify our BP results, we conduct the directivity analysis using all the global teleseismic broadband records. Assuming a simple kinematic source model for an earthquake rupturing on a rectangular fault of finite length L , the apparent rupture duration, t_d , observed from a teleseismic P wave at azimuth, φ , is expressed as $t_d = \frac{L}{v} - \frac{L \cos(\varphi - \varphi_r) \sin i_h}{c}$, where c is the P-wave velocity, v the rupture speed, i_h the take-off angle, and φ_r the rupture azimuth. If the Meinong earthquake ruptured with multiple subevents, by arranging the waveforms as a function of directivity parameter defined as $-\frac{\cos(\varphi - \varphi_r)}{c}$ (Zhan et al., 2014), we would observe the multiple coherent arrivals aligned along the straight lines with different slopes. The rupture duration, $\frac{L}{v}$, for each subevent is equal to the intercept of the line crossing the zero directivity parameter. Considering the rupture propagates predominantly toward N61°W as seen in the BP image, we display the displacement waveforms aligned on the onset P arrivals as a function of directivity parameter (Figure 4.3b). The rupture directivity toward the NW is clearly evidenced by the time duration of the first pulse linearly increasing with the directivity parameter. Besides, the onset times of the second pulses seem to be

aligned on the same moveout as the P. Though the amplitudes of these two pulses vary differently with the directivity parameter, the overall waveform shapes are very similar with one single dominant peak, further implying that these two seismic pulses originate from the same rupture process.

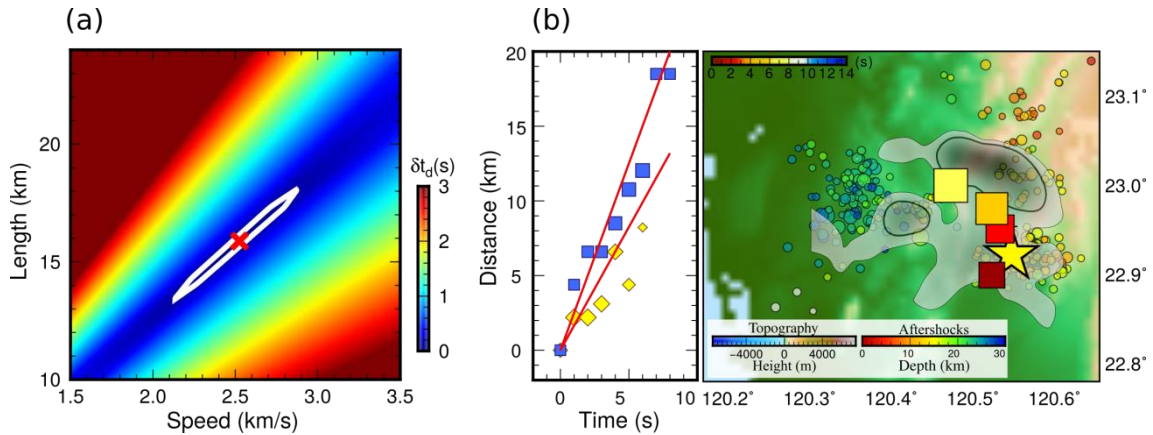



Figure 4.4 Directivity analysis result, the rupture distances and times at EU and AU array and the comparison of BP result with finite fault inversion.

(a) The rupture speed (v) and length (L) (red cross) that best fit the observed rupture duration (t_d) at the AU, EU, and NA stations from the directivity analysis. Color image shows the RMS misfit between the observed and predicted t_d (white ellipse for RMS=0.1 s). (b) (Left) Propagation distance of the time-evolving radiators from the hypocenter at the AU (square) and EU (diamond) array. The average v estimated by the slope of each least-squares fit line is 2.5 and 1.6 km/s, respectively. (Right) Comparison between the radiator locations (square) from the AU image and cumulative slip distribution from the finite-fault model (Lee et al., 2016), with light and dark gray shaded areas showing the slip exceeding 15% and 30% of the maximum value. Star and circles denote the epicenters of the mainshock and aftershocks.

4.6 Discussions and conclusions



The finite-fault model of Lee et al. (2016) shows that the Meinong earthquake has two slip asperities with an overall area of $\sim 25 \times 25 \text{ km}^2$ and the moment release with a total duration of $\sim 16 \text{ s}$. However, our BP and directivity analyses yield the considerably shorter rupture length ($\sim 17 \text{ km}$) and duration ($\sim 7 \text{ s}$), with the strong directivity pointing more toward the northwest than the fault strike of $N79^\circ W$ assumed in their finite-source model. The rupture extent constrained by our AU image is partially overlapped with the first asperity which starts with a small patch near the hypocenter at 0-2 s, and during 2-8 s moves downdip about 18 km and then horizontally about 10 km to the west (Figure 4.4b). The resulting moment rate function has the prominent peaks at 3-5 s, similar to the strongest radiation burst which reaches the maximum amplitude of the MUSIC pseudospectrum in the AU image (Figure 4.2c).

The second asperity developed after 9 s is located immediately west of the first one but shifted to the shallower depth of $\sim 15 \text{ km}$ above the off-fault aftershock cluster. This smaller slip patch is collocated with the radiator emitted at 10 s in our AU image (Figure 4.4d), where the sP and reverberating wave trains are considered as part of the direct P in the BP imaging. It results in a continuously westerward-propagating rupture with a much longer rupture length and duration atypical for the $M_w 6.4$ event. We find the direct P and depth phases of the shallow Meinong event would overlap each other if the lowpass cutoff frequency chosen to filter the waveforms at the AU stations is too low at 1 Hz as that used for the finite-fault inversion. This may explain that the moment magnitude of several earthquakes with $M_w = 6.0 \sim 6.5$ in Taiwan tends to be

overestimated by the finite-fault models compared to the global CMT solutions, and so do the rupture area and source duration.

Combing the BP results with constraints from the directivity and source radiation pattern, we conclude that the rupture does not reach the depth shallower than 15 km nor beyond the off-fault aftershock cluster about 20-30 km northwest of the hypocenter. The Meinong earthquake happened to rupture toward the NW azimuth close to the maximum S-wave excitation. The radiated energy propagating through the very thick, low-velocity layer west of the epicenter generated strong reverberations. Synergistic amplification of ground motion by strong directivity and excitation of sP and reverberations mainly caused the destruction in Tainan further to the NW from the rupture zone. Our analysis demonstrates the source parameters such as the rupture extent and duration especially for strong shallow earthquakes with $M_w < 7$ can be overestimated if late-arriving P-wave energy included in the BP imaging and finite-fault inversion are dominated by depth phase and reverberant energy.

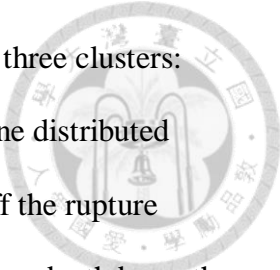
Chapter 5 The 2010 Jiashian and 2016 Meinong earthquakes:

doublet ruptures interact across two strong asperities



5.1 Abstract

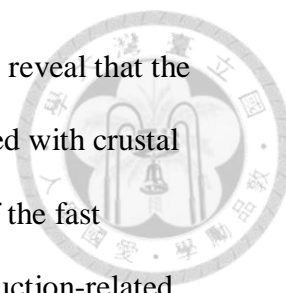
In the last decade after about 45 years of seismic quiescence, southwest Taiwan was imperiled by two strong earthquakes occurring in relatively close proximity, the 2010 M_w 6.2 Jiashian earthquake and the deadly 2016 M_w 6.4 Meinong earthquake. The focal mechanisms and aftershock distributions imply that both events had rupture along the NW-SE striking, shallow-dipping fault planes at the depths of 21 and 16 km, respectively, with their hypocenters horizontally separated by ~ 17 km. Here we present the Multiple Signal Classification (MUSIC) back projection (BP) images using high-frequency P- and sP-waves recorded by the European and Australian seismic networks, the directivity analysis using global teleseismic P waves, the distribution and predominant focal mechanisms of relocated aftershocks, and the temporal variation in the frequency-magnitude distribution (b-value) of regional seismicity to characterize the rupture characteristics of the two mainshocks and explore the potential connection between them. The results of the Meinong event indicate a unilateral, subhorizontal rupture propagating ~ 17 km northwestward and lasting for ~ 6 -7 s (Jian et al., 2017). The Jiashian earthquake nucleated ~ 5 km deeper and ruptured obliquely toward the NW and up-dip ($\sim 16^\circ$) direction with a shorter rupture length of ~ 10 km and a duration of ~ 4 -5 s. The up-dip propagation is corroborated by the 3-D directivity analysis. Moreover, the refined aftershock locations reveal that the Jiashian sequence is confined in an elongated zone extending 15 km in the NW-SE direction and located 0-3 km



shallower than the hypocenter. The Meinong aftershocks mainly form three clusters: the first one clustered around the mainshock hypocenter, the second one distributed deeper (>20 km) and ~ 20 km northwest of the mainshock epicenter off the rupture plane, and the third one occurring farther east of the epicenter at <10 km depth beneath the southern Central Mountain Range. As evidenced by similar magnitudes, focal mechanisms, rupture directions and propagation speeds of the two mainshocks as well as the spatial configuration of the rupture zones and aftershock distributions, we attribute their occurrence to the surface roughness and strength heterogeneity with the two relatively stronger and larger asperities on a buried oblique fault that have been recently reactivated and interacted with each other through static stress transfer, which consequently caused the ruinous destruction in SW Taiwan.

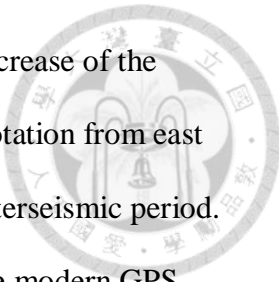
5.2 Introduction

The region of Taiwan, located at the junction of the Eurasian Plate (EP) and the Philippine Sea Plate (PSP) Plate, presently undergoes a fast convergence rate of 82 mm/yr in direction of $N310^{\circ}E$ obliquely to the northeast-trending Eurasian (EU) continental margin (Seno et al., 1993; Yu et al., 1997). The PSP subducting beneath the EP in the north but overriding the EP in the south of Taiwan is well depicted by seismicity down to at least a depth of about 200 km (Kao et al., 1998a, 2000; Kao and Rau, 1999). In between, the collision of the Luzon arc on the PSP with the EU continental margin has produced the highly-deformed, NNE-SSW striking orogenic belts with a very high rate of seismicity unevenly distributed in the Taiwan island



(Suppe, 1984). Numerous seismotectonic and geodetic investigations reveal that the earthquakes occurring with diverse faulting mechanisms are correlated with crustal deformation and stress patterns, largely controlled by the direction of the fast convergence of the PSP relative to the EP and the orogeny- and subduction-related structures (Kao and Jian, 1999; Hsu et al., 2010) (Figure 5.1). In the last century, most catastrophic earthquakes occurred in the two prominent thrust zones in the western and eastern side of the Central Mountain Range, including the tragic 1999 ChiChi earthquake with moment magnitude (M_w) of 7.6 that hit central western Taiwan. However, because of the relatively low seismicity in southwest (SW) Taiwan, comprehensive evaluations of the statistical and physical properties of the historical seismicity, the structures and behaviors of active faults, and seismic hazard potential are still insufficient in this region.

Within a decade, southwestern Taiwan was struck by two nearby large earthquakes: the 2010 M_w 6.2 Jiashian and the deadly 2016 M_w 6.4 Meinong. The epicenters of these two mid-to-lower crust events (with the focal depths of 22.6 and 16.7 km) were not located in any previously-known linear features but adjacent to two major faults, the N-S striking Chaochou fault (CcF) and the NE-SW striking Chishan fault (CF) which border the flat Pingtung Plain (PP) to the east with the Central Range (CR) and to the west with the southern Western Foothills (WF), respectively (Figure 5.1b). The Meinong and Jiashian earthquakes are found to lie in the northern boundary between the PP and the WF near the northern tip of the CF and east of the CcF in the CR, respectively. Despite very sparse and rare earthquake activities during the instrumental period and in historical records, Ching et al. (2007) and Hsu et al. (2009) speculated the presence of subsurface hidden shear or fault zones oblique to the



existing N-S and NE-SW striking active faults to accommodate the increase of the strain rate from the north to south Taiwan and the counterclockwise rotation from east to west of the GPS velocity across SW Taiwan observed during the interseismic period. In addition, many studies integrating multiple field observations of the modern GPS strain rates, paleostress, and tectonic-geomorphic features advocated that the PP has experienced the lateral extrusion toward the W and SW with the right-lateral shear deformation (Lacombe et al., 2001; Ching et al., 2007; Angelier et al., 2009; Hsu et al., 2009; Deffontaines et al., 2016). Prior to the 2010 Jiashian earthquake, it is noted that a 20-km long, NW-SE trending seismogenic zone is present in the depth range of ~10-20 km and almost juxtaposed with the transition boundary from the low-relief PP to the high-elevated WF. The inversion of regional stress (Michael, 1984) using the earthquake focal mechanism data from a recently-improved regional MT (moment tensor) catalog (Jian et al., 2018) indicates that the axis of the average principal stress is about 28° counterclockwise from the azimuth of the GPS velocity field. Such noticeable difference implies that there may be a transition in the deformation and stress distribution between the upper and lower crust controlled by various tectonic mechanisms. Studies of the source characteristics and linkage of the mainshocks and aftershocks of these two earthquake sequences would help unravel the important hidden structures in the transition boundary and further understand the principal tectonic processes that govern the seismogenic potential in SW Taiwan.

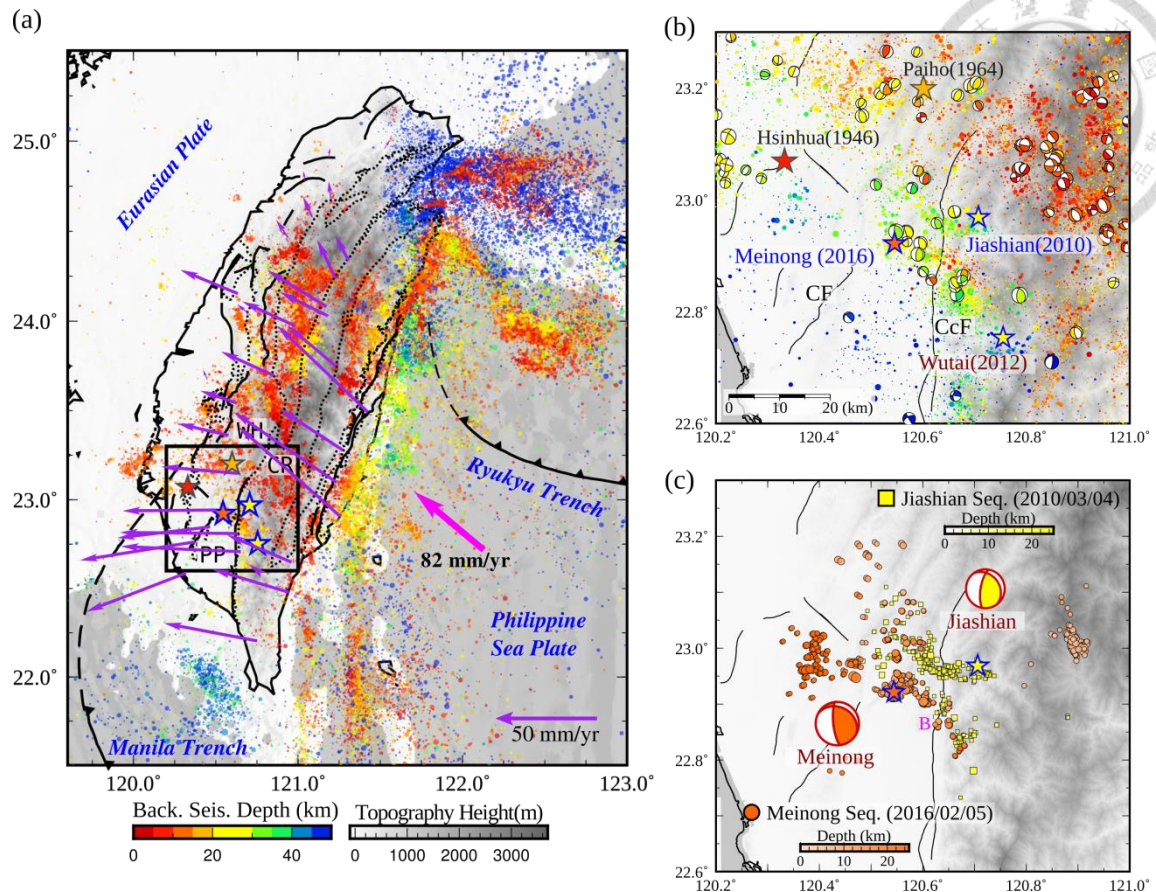
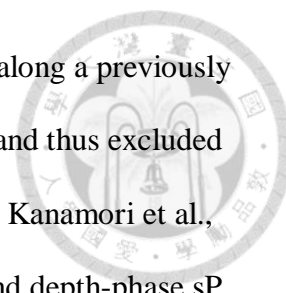


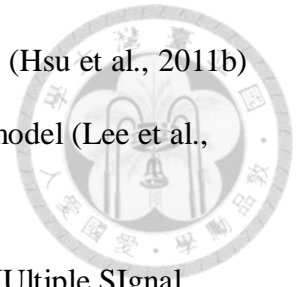
Figure 5.1 Map showing seismicity and tectonic settings in Taiwan

(a) The dots showing the earthquakes ($M_L \geq 2.5$) from CWB relocated catalog are colored by the focal depth. Pink thick arrow indicates the current convergent direction. Purple arrows show the some selected average GPS velocity field relative to station of Paisha, Penghu. (b) Enlarge map of the study area showing the background seismicity and regional focal mechanisms ($M_W \geq 3.0$) from AutoBATS catalog (Jian et al., 2018) before 2010 Jiashian earthquake. The stars mark the large earthquakes ($M_L \geq 6.0$) from 1900 to 2016. (c) The 2010 Jiashian and 2016 Meinong aftershock sequences are shown in circles colored by the focal depth in yellow and orange color-bars, respectively. The focal mechanisms of two mainshocks are from USGS. The abbr. on the map: WH: Western foothill; CR: Central Range; PP for Pintong Plain; CF: Chishan Fault and CcF: Chaochou fault.

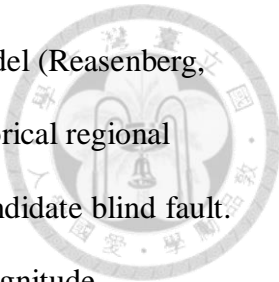


Previous studies verified that the Meinong earthquake ruptured along a previously unknown blind fault striking NW and gently dipping toward the NE and thus excluded the CcF or CsF as candidate faults (Lee et al., 2016; Jian et al., 2017; Kanamori et al., 2017). The rupture process revealed from BP of high-frequency P- and depth-phase sP waves further puts tight constraints on the spatial extent of the rupture area and kinematic rupture parameters which result in a predominantly unilateral rupture propagating toward the NW with the rupture length of ~17 km and a single-peak source radiation duration of ~7 s (Jian et al., 2017), in agreement with those estimated from the directivity analysis of global broadband teleseismic and local strong-motion records (Jian et al., 2017; Kanamori et al., 2017). On the other hand, the finite-fault model of the Meinong earthquake obtained from the inversion of combined teleseismic, strong motion and geodetic data suggests a two-stage rupture process with two peaks of slip over a larger area extending updip and further to the west and a total source-time or rupture duration of (~16 s) at least twice longer than that from the BP result (Lee et al., 2016). The finite-fault model of the Jiashian earthquake obtained in the same way also reveals the same source-time duration of ~16 s with two large slip areas corresponding to two peaks of moment release, for which the rupture initially propagates westward for a short distance inducing large slip in the deeper and larger asperity at 12-22 km depth and later moves upward to near surface with the second smaller slip patch distributed over the depth of 2-8 km (Lee et al., 2013). The resulting slip distribution and rupture extent are the finite fault inversion results from the postulated curved thrust fault segment between the CF and CcF, named the Chishan transfer fault zone, with a low angle dip at mid-crustal depths, and more steeply dipping at shallow depths toward the NE. However, neither the aftershocks nor the

coseismic slips determined from the inversion of GPS displacements (Hsu et al., 2011b) are found in the near-surface asperity as observed in the finite-fault model (Lee et al., 2013).



Jian et al. (2017) first applied a high resolution array method, Multiple Signal Classification (MUSIC) analysis (Meng et al., 2011) to BP imaging of the rupture process for the Meinong earthquake occurring in the structurally complex setting even with a moderate magnitude but causing severe damages in the vicinity of the metropolitan city. The results suggest that the finite-fault models may overestimate the rupture extent, duration, and moment release of moderate-sized earthquakes in Taiwan because of the lower-frequency waveform data and uncertainties in the assumed fault geometry, source parameters, and velocity structures through which seismic waves propagate used in the inversion (Jian et al., 2017). This motivates us to revisit the detailed rupture process for the Jiashian earthquake as well, since both the events have comparable moment magnitudes and focal mechanisms. Following the procedures of Jian et al. (2017), we determine the rupture process of the Jiashian earthquake by integrating the BP images obtained with direct P and depth-phase sP wavetrains. The resulting source properties including the rupture direction, length, and duration are also compared and cross-checked with those derived from the directivity analysis using global displacement waveforms. Our investigations support that the two events ruptured with similar propagation speeds on an unknown fault surface with the same geometry striking N40°W and dipping toward the NE, and the estimated rupture lengths and durations are of the same order but much shorter than those resulting from the finite-fault inversion. Despite no geological field observations to make a direct link with the hidden causative faults of the two events, we identify and relocate their



respective aftershock clusters based on the earthquake interaction model (Reasenber, 1985) and determine focal mechanisms of larger aftershocks and historical regional earthquakes (Figure 5.1c) to help characterize the geometry of the candidate blind fault. A recent study of the spatial variation of the earthquake frequency-magnitude distribution, i.e. b-value, in Taiwan indicates the change of the b-value is inversely correlated with the variation in the GPS-derived differential strain-rate or stress (Chen et al., 2017). We thus compare the b-values of seismicity in the vicinity of the rupture areas before and after the main shocks to understand the circumstance of stress accumulation for the impending large earthquakes. Finally, we define the geometry and dimension of the source and receiver faults based on focal mechanism and aftershock distributions and testify the possibility of the triggering of the Meinong mainshock by the preceding Jiashian earthquake through static stress transfer.

5.3 The MUSIC Back Projection and data

The back-projection (BP) method retrieves the coherent P wavefield recorded by a dense seismic array backward in time to the respective energy emitted positions during an earthquake rupture process. It requires minimal assumptions of the fault geometry and rupture kinematics plane and provides a high-resolution source radiation process using high-frequency seismic wave energy (Ishii et al., 2005; Kiser and Ishii, 2012). In our study, we adopt a frequency-domain BP approach which combines multitaper cross-spectral estimation and MUSIC (MUltiple SIgnal Classification) for identification of seismic source radiators of coherent signals orthogonal to the noise

subspace (Meng et al., 2011). The method is originally employed to image the rupture processes of great megathrust and deep-focus earthquakes using teleseismic array data (Meng et al., 2011, 2014) and major earthquakes recorded in regional distance (Meng et al., 2012a). We first demonstrated its capacity to resolve the rupture characteristics of the damaging Meinong earthquake with only a moderate magnitude ($M_w=6.4$) (Jian et al., 2017), providing that the waveforms of multiple phase arrivals are carefully identified and aligned prior to performing the back projection.

We follow the same procedure as that for the Meinong earthquake to explore the rupture process of the Jiashian earthquake. The vertical-component velocity waveforms obtained from the European (EU) and Australian (AU) seismic networks are first bandpass filtered between 0.5-1.5 Hz and aligned at the onset of initial P arrivals (Figure B1). Considering that the signals in each short-time window are emitted from a suite of candidate radiation points positioned at 2-km spaced grid nodes on a $50 \times 50 \text{ km}^2$ fault plane with a trial orientation derived from the centroid moment tensor solution, we estimate the corresponding MUSIC pseudospectrum defined as a measure of waveform coherence across the array.

As the trade-off between the traveling time and distance of the waveforms yielding smearing effects with certain spatial uncertainty can be largely reduced when combining the BP images resulting from multiple phase arrivals with various angles of incidence. For mid-crust earthquakes with moderate magnitude ($M_w \sim 6$), the rupture duration is sufficiently short such that the upgoing depth phases pP and sP are separated far enough in time from the downgoing P phase. As such, the wavetrains of these depth phases can be individually projected back in time to source radiation locations as long as they do not interfere substantially with the preceding long-lasting P

wavetrains or the following strong sediment reverberations (Jian et al., 2017). In the next section, we demonstrate that the pP and sP phases of the Jianshan earthquake are identified and picked through comparison with the corresponding synthetic waveforms. The same BP approach is employed to estimate the MUSIC pseudospectrum at all the candidate radiators associated with the sP wavetrains. The amplitudes of the obtained BP images then are summed linearly to locate the strongest radiators.

5.4 Rupture Characteristics of the Jianshan Earthquake

5.4.1 Back Projection Rupture Image

In Figure 5.2, we demonstrate our BP results for the Jianshan earthquake using the EU and AU array data, where each panel shows the spatiotemporal evolution of the strongest seismic radiation emitted during the rupture process determined by back projecting the P and sP wavetrains separately and combining the direct and depth-phase BP images. The pseudospectrum power time function (PSTF) shown in the lower-right inset displays the MUSIC pseudospectrum of the strongest radiator as a function of rupture time for each BP image. Considering the first 20-s P wavetrains as the radiated energy, the resulting PSTFs consist of two energy radiation bursts with comparable amplitude and duration, each of which lasts for about 6 s and 7 s in the EU and AU array, respectively (Figure 5.2a & d). During the first rupture stage, both the array data result in consistent spatiotemporal distributions of seismic radiation, suggesting a unilateral rupture propagating ~11 km along the strike azimuth (N60°W) and 3-5 km along the up-dip direction (see the upper-right insets of Figure 5.2).

However, the second-stage rupture processes resolved from the two arrays are distinctly different. The EU result reveals a continuously NW-ward progressive rupture from 8 to 16 s, whereas the energy radiators between 10 and 20 s observed in the AU image wander in the opposite direction toward the epicenter. Jian et al. (2017) found similar rupture scenarios for the Meinong earthquake if the later depth-phase energy were mistakenly treated as part of the P wavetrains and back projected to the candidate radiation points by using the P-wave travel times.

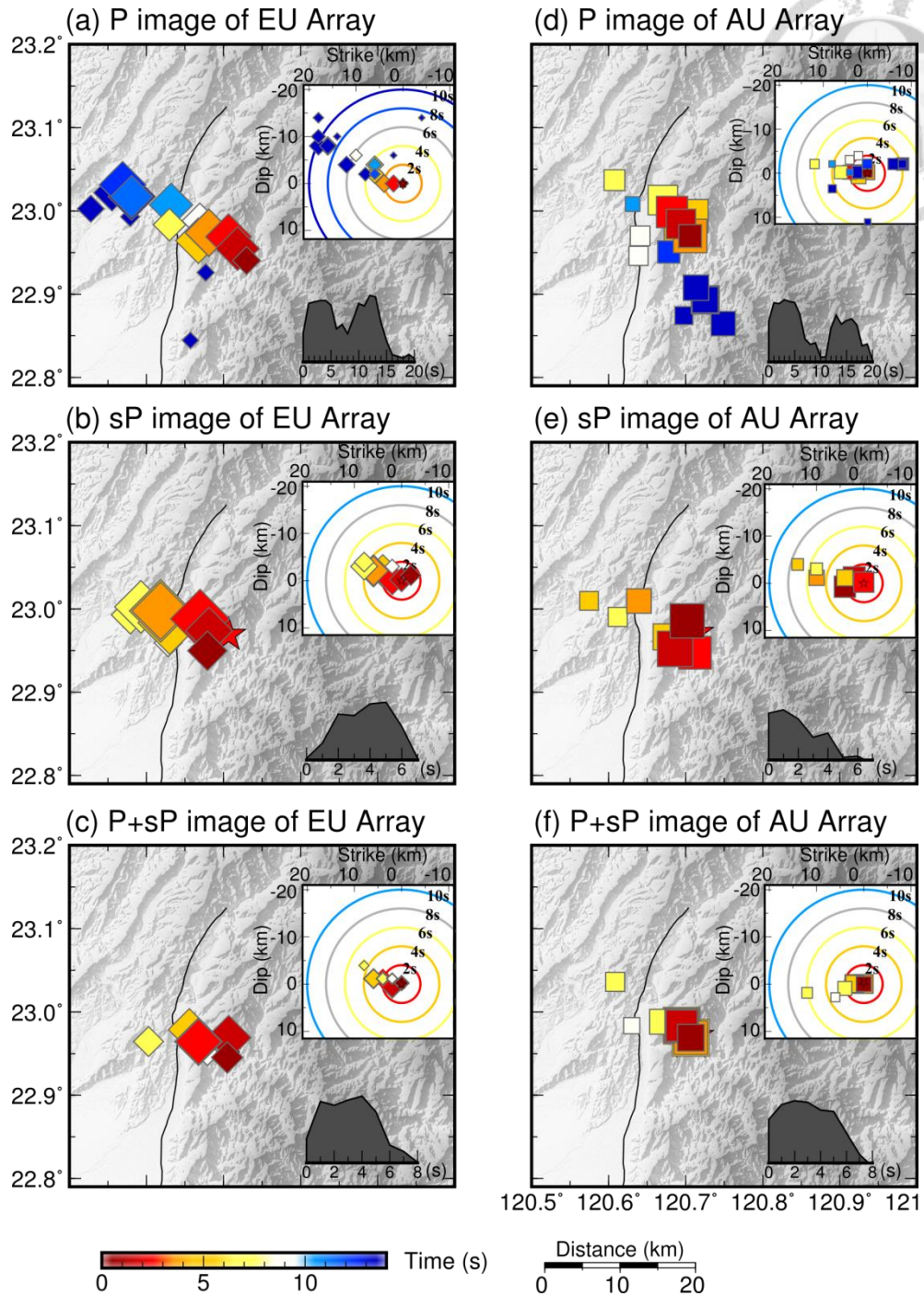
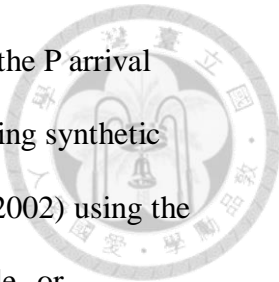


Figure 5.2 The resulting BP images of 2010 Jiashian earthquake from the EU and AU seismic array. The data used for BP images are ~20s P, ~7s sP waves at EU (a)-(b) and AU (d)-(e) array. The combined BP results of direct P- and sP- waves of EU and AU arrays are displayed in (c) and (f), respectively. The symbols are scaled by the BP pseudo-spectrum power and colored by time elapsed. Lower-right inset shows the source time function with pseudo-spectrum power. The upper inset shows the distance of the radiators from the hypocenter along the strike and dip, with concentric circles representing the rupture fronts by assuming a rupture speed of 2.0 km/sec.



To verify that the wavetrains beginning at ~ 7 s after the onset of the P arrival mainly comprise the depth-phase signals, we calculate the corresponding synthetic seismograms by a frequency-wave number method (Zhu and Rivera, 2002) using the global IASP91 model. The earthquake source is represented by a single- or double-point source model with the same focal mechanism provided by the US Geological Survey and the hypocenter by the Central Weather Bureau (CWB) of Taiwan. The synthetics generally reproduce the first-order features of the observed displacement pulses (Figure 5.4 & Figure B2), showing a polarity reversal of the pP and sP phases arriving at ~ 7 s and ~ 10 s and comparatively very low pP amplitudes at the azimuths between 120° and 190° to the AU array. Therefore, we select the larger-amplitude sP wavetrains sufficiently separated from the direct P-wave coda from both arrays to perform the same BP imaging as done with the P waves. The resulting BP images of EU and AU array exhibit a very similar pattern to that resolved from the P waves in the first 8-s period, confirming that the Jiashian mainshock ruptured unilaterally to the NW and updip direction with the effective source duration of about 5-6 s (Figure 5.2a & c). However, the sP BP images from the AU array, the relatively weak sP arrivals across the AU seismic network (Figure B1c) are not coherently enough to robustly locate the radiators in space and time. It is also noted that the depth phases travel through the crust with sharp lateral velocity gradients across the arc-continent collision suture zone in southeast Taiwan (Figure B3). The contamination of strongly scattered waves may lead to the unstable BP source images in the AU array. By summing the amplitudes of the P and sP pseudospectrum for each array to track the strongest radiators in time and space, we conclude that the rupture zone of the Jiashian earthquake extends respectively about 11-12 km and 3-5 km along the strike and updip

direction, largely overlapped with the distribution of relocated aftershocks (Figure 5.2c&f and Figure 5.3). The following discussions of the rupture properties of the Jiashian earthquake and comparisons with those of the Meinong earthquake are based on the P- and sP-wave integrated BP results from the EU array.

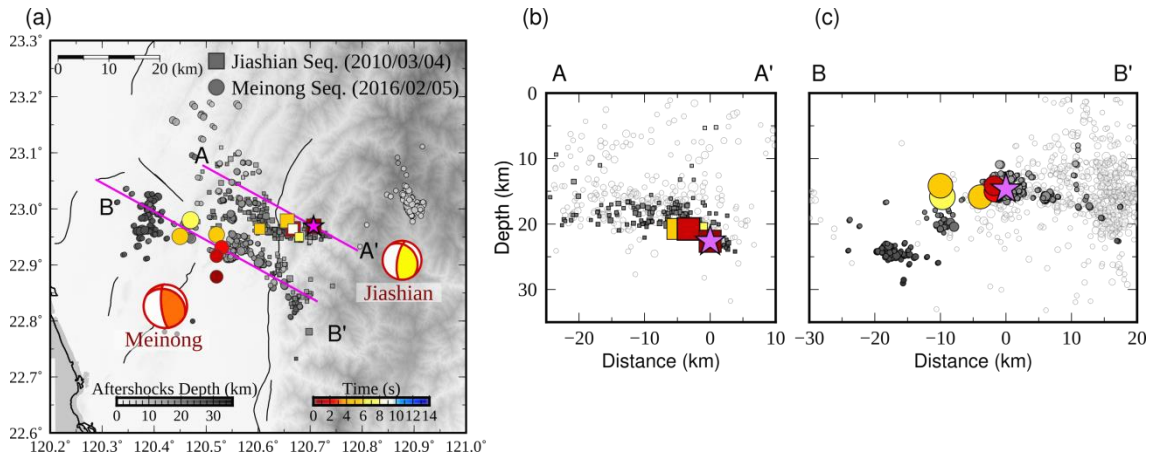


Figure 5.3 The resulting BP images of Jiashian and Meinong earthquakes.

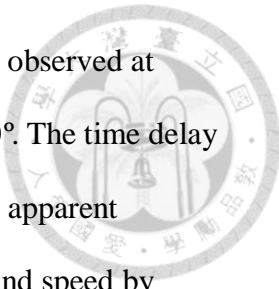
(a) Map showing the BP results and aftershocks in circles and diamonds for Meinong and Jiashian earthquakes, respectively. The BP results and aftershocks are colored by the elapsing time and focal depth, respectively. The cross-sections showing the BP results and aftershocks distributions along the profile of (b) AA' and (c) BB' for Jiashian and Meinong earthquakes, respectively. The symbols for BP results are the same as those shown in Figure 5.2.

5.4.2 3-D Rupture Directivity Analysis

Our previous BP and directivity study for the Meinong earthquake (Jian et al., 2017) indicates a near-horizontal rupture propagation toward the NW with negligible downdip movement (Figure 5.3c). For the Jiashian earthquake, the resulting BP image reveals both the along-strike and updip rupture propagation as shown in Figure 5.2 and Figure 5.3b. To further examine whether the up-dip rupture directivity significantly modulates the duration of the observed P wavetrains, we conduct a rupture directivity analysis by taking into account both the strike and dip components in a unilateral kinematic rupture model (Park and Ishii, 2015). The apparent rupture duration, t_d , of the teleseismic P wave at azimuth φ , is expressed as

$\frac{L}{v} - \frac{L(\sin r \cos i_h + \cos \gamma \cos(\varphi - \varphi_r) \sin i_h)}{c}$, where c is the P-wave velocity, v is the rupture speed, i_h is the take-off angle, φ_r is the azimuth of the rupture direction measured clockwise from the north and γ is the rupture dip angle positive downward from the horizontal. Given a ruptured event propagating in the direction specified by φ_r and γ , the apparent rupture duration viewed from the time span of P-wave displacement pulses at various station azimuths would increase linearly with the directivity parameter defined as $-\frac{\sin r \cos i_h + \cos \gamma \cos(\varphi - \varphi_r) \sin i_h}{c}$ and the slope of the linear trend is proportional to the rupture length L . If the rupture of the Jiashian earthquake, like that of the Meinong earthquake, primarily propagated horizontally toward the NW, the directivity parameter simply becomes $-\frac{\cos(\varphi - \varphi_r) \sin i_h}{c}$.

In Figure 5.4, the global vertical displacement waveforms of the Jiashian earthquake are aligned at the P-wave onset and presented as a function of station azimuth. Within the first 6-s time window that mainly comprises the direct P



wavetrains, the double-peaked pulses with comparable amplitudes are observed at most of the recording stations except those with azimuth in 290° - 310° . The time delay between the two pulses appears to vary with azimuth. Based on above apparent duration equation of horizontal rupture, we search the rupture length and speed by minimizing the observed and predicted rupture duration by assuming Jiashian earthquake ruptured horizontally along the strike of 325° from the focal mechanism reported by USGS. The resultant rupture length and speed are ~ 5 km and 1.0 km/s which are apparently much shorter and slower than the estimations with our BP result (Figure 5.5a). The resulting BP image indicates that the Jiashian earthquake ruptured upward $\sim 16^{\circ}$ along the strike of $\sim 300^{\circ}$, the rupture direction may not be the same as the strike of focal mechanism and the rupture dip angle should also be accounted for. In this case, the same global search on rupture strike, dip, length and speed is performed again. In order to demonstrate the importance of adding variables of rupture strike and dip into global search on minimizing the errors between observed and predict apparent source durations. We perform the F-test for three hypotheses of adding strike, dip or both with the presumed hypothesis in which there are only two searching variables of length and speed. According to the definition of the F-test statistics, when the P-value equals to 0, it means the tested hypothesis can't be rejected. The resulting F-test statistics are 207.5, 66.6 and 113 for three tested hypotheses and the corresponding P-values are all equals to 0. Through the F-test, we confirm the necessity on searching both strike and dip of rupture direction. Figure 5.5c shows the minimum errors respect to the scanned strike and dip, it should be noted that the directivity analysis having much larger uncertainty on the dip than strike. The best strike is about 275° ~ 285° and dip is -20° ~ -45° . However, the relocated aftershock sequence and BP result (Figure 5.3)

suggest the rupture dip angle should be in the range of -16° ~ -20° . When we fixed the strike of 280° and dip -20° , the resultant of rupture length and speed are 11.25 km and 2.2 km/s which are consistent with the results from BP images (Figure 5.5b&d).

Colligating the estimations of rupture length and width inferred from the BP images and relocated aftershock sequences (Figure 5.3), the static stress drops could be estimated with the assumption of $\lambda=\mu$. The stress drop of Jiashian earthquake ranges from 5 ~ 9 Mpa for rupture widths of 4-6 km. For Meinong earthquake, the stress drop is about 4 ~ 10 Mpa if the rupture width ranges in 5-8 km. Although the uncertainty of stress drop arises from the ambiguous of rupture width estimations, the stress drop of two earthquakes are comparable.

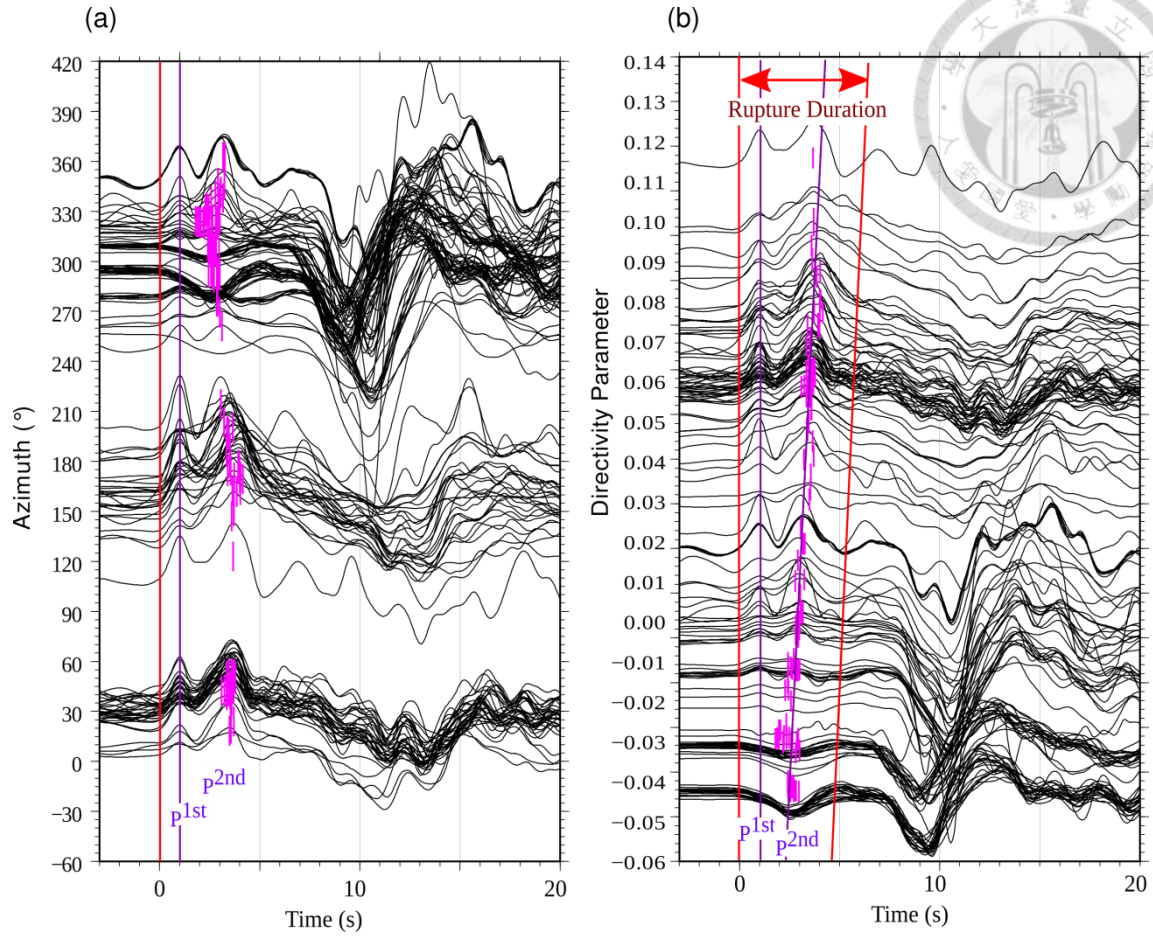


Figure 5.4 Global displacement waveforms of 2010 Jiashian earthquake.

The vertical displacement waveforms are assorted by the (a) azimuth and (b) directivity parameter by setting the rupture strike and dip of 310° and -16° . The purple lines mark the aligned crest of the P waves. The short pink lines mark the hand-picked second crest corresponding to the peak of the second subevent. The rupture duration varying with directivity parameter are marked by the red lines.

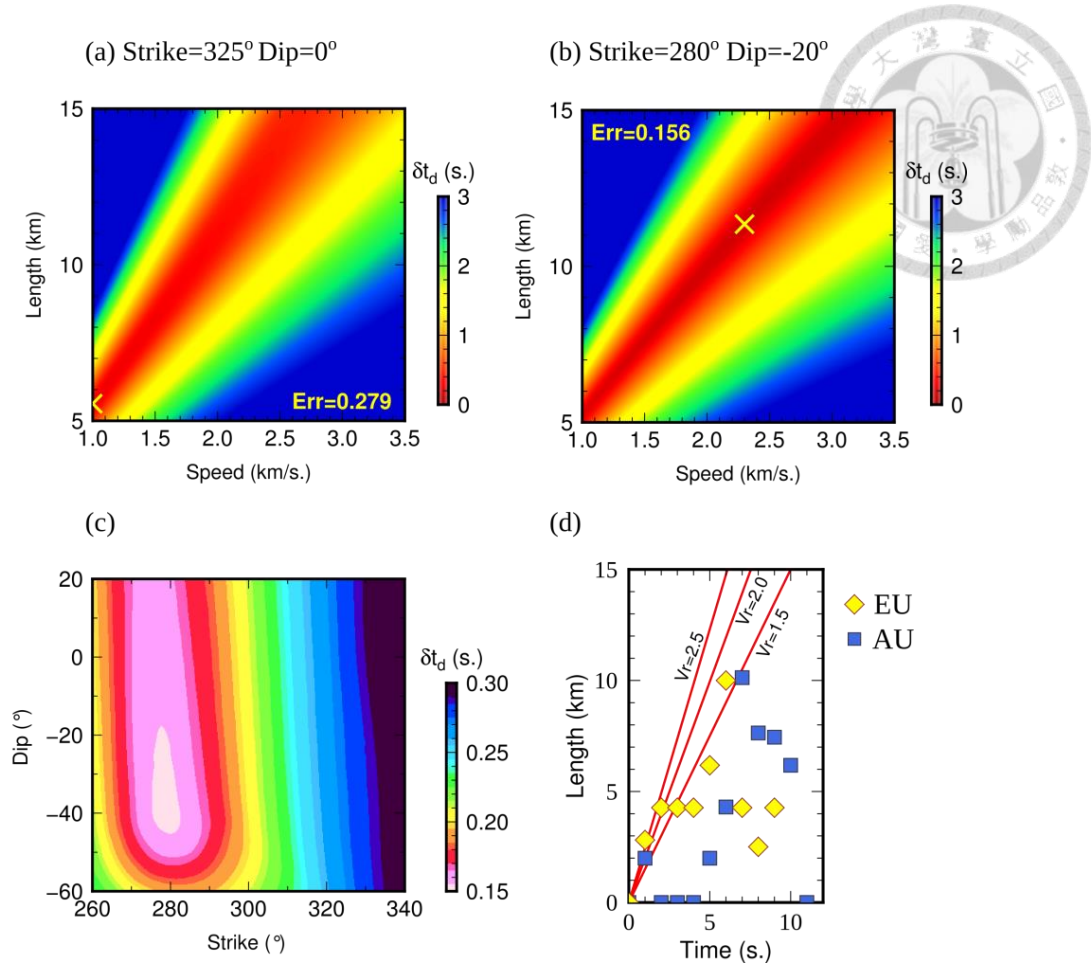
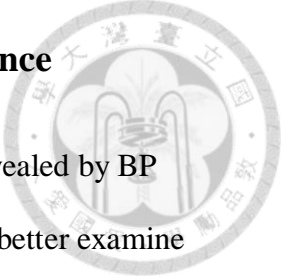


Figure 5.5 The directivity analysis results and comparison with BP results for 2010 Jiashian earthquake. (a)-(b) Misfit functions of apparent source durations respect to the rupture length and speed. (a) The best rupture length and speed (yellow cross) are 5.5 km and 1.0 km/s with error of 0.279 s with fixed rupture strike of 325° and dip of 0°. (b) The best rupture length and speed are 11.25 km and 2.2 km/s with error of 0.156 s with fixed rupture strike of 280° and dip of -16°. (c) The misfit function respect to the rupture strike and dip. The searching variables include rupture strike, dip, length and speed for best fitting the observed rupture durations. Note: each grid shown in (c) representing the smallest misfit among 4 scanned variable, which means the resultant length and speeds in each grid are all different. (d) The rupture length and time from the hypocenter and onset time of P wave from EU (yellow diamonds) and AU (blue squares) BP images. The text on each red line labels the rupture speed.

5.5 The 2010 Jiashian and 2016 Meinong doublet sequence



The slightly upward NW-ward rupture of Jiashian earthquake revealed by BP image and directivity analysis delineated the overall rupture zone. To better examine the aftershock sequence, we performed the cluster analysis proposed by Reasenber (1985) and Hypo-DD relocation (Waldhauser and Ellsworth, 2000) for aftershocks that occurred within 1 year after Jiashian earthquake. The relocated Jiashian aftershock sequence extends parallel with the NW-SE striking fault plane and also gradually shallows toward the west (Figure 5.1c & Figure 5.3a). The same procedures of cluster analysis and Hypo-DD relocation are also processed for Meinong aftershocks, and one of the clusters around the epicenter of Meinong event also distributed subhorizontal and parallel with the rupture direction of Meinong earthquake (Figure 5.3). We also notice a clear gap between two earthquake sequence both in horizontal and vertical direction which tell us the rupture zones of Jiashian and Meinong events are separated with each other. We proposed a blind causative fault responsible for these two major earthquakes because of two following observations. The first one, according to the focal mechanisms issued by USGS, the differences of strikes and dips between two closed by earthquakes are only 24° and 3° . The Second, the regional focal mechanisms for small aftershocks in this area from AutoBATS MT catalog (Jian et al., 2018) are showing similar focal mechanisms (Figure 5.6a) just like two mainshocks. The Figure 5.6 illustrates the fault geometry based on the focal mechanism of Meinong earthquake from USGS report. Along the cross-section of profile BB' (Figure 5.6b), we see the Jiashian earthquake sequence lying at the deeper part of the same proposed fault plane which ascertain our assumption about the one blind causative fault in the crust. The

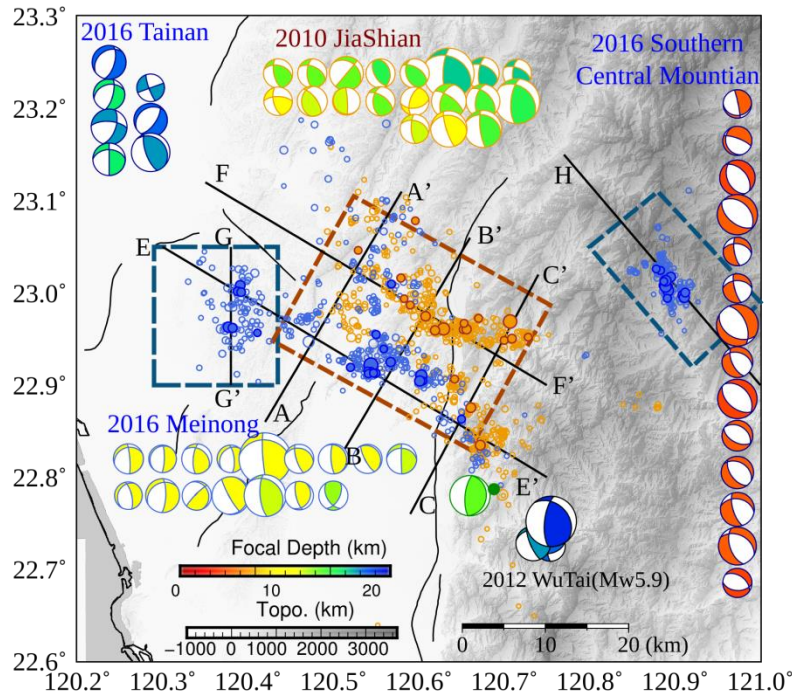
width of this blind fault can be roughly confined by the delineations of two aftershock sequences. To the east along the strike, we see a small group of vertical distributed earthquakes which is not along the blind fault plane (profile CC' & EE' in Figure 5.6b) and those can be treated as the east boundary of our presumed fault. The western bound of the fault is not easy to determine because of the sparse distributed aftershocks in the west. Summarizing above the rupture extends from BP results and aftershock sequences of Jiashian and Meinong earthquakes, we define the causative fault plane with a minimum rupture area of $27 \times 22 \text{ km}^2$ (abbreviated as JSMN fault).

The 2010 Jiashian and 2016 Meinong earthquakes not only might occur on a blind JSMN fault but also can be regarded as a doublet sequence because of several similar kinematical rupture properties of two events including closed epicenters, nearly identical focal mechanisms, rupture directions and speeds (Lay and Kanamori, 1980; Kagan and Jackson, 1999). Moreover the 6 years apart of the occurrences of Jiashian and Meinong earthquakes are not too long considering that SW Taiwan is an over 50 years seismic quiescence area before the 2010 Jiashian earthquake. Prior this doublet sequence, there was a NW-SE trend background seismic belt composed by small events ($M_L < 5.0$) and the Meinong earthquake just occurred on it (Figure 5.1b). As mentioned above, in the presumed JSMN fault area, the focal mechanisms of background earthquakes (Figure 5.1b) and the aftershocks are overall consistent with two mainshocks (Figure 5.6) (Jian et al., 2018). To understand the seismologic properties of this JSMN fault which has deficient geological observations, we first study the seismic activities by calculating the frequency-magnitude distribution and then calculate the Coulomb stress change on the fault itself and two off the fault triggered aftershock clusters by Meinong earthquake induced by two mainshocks. All

the computations are based on the rough geometry estimation of JS-MN fault as shown in Figure 5.6.



(a)



(b)

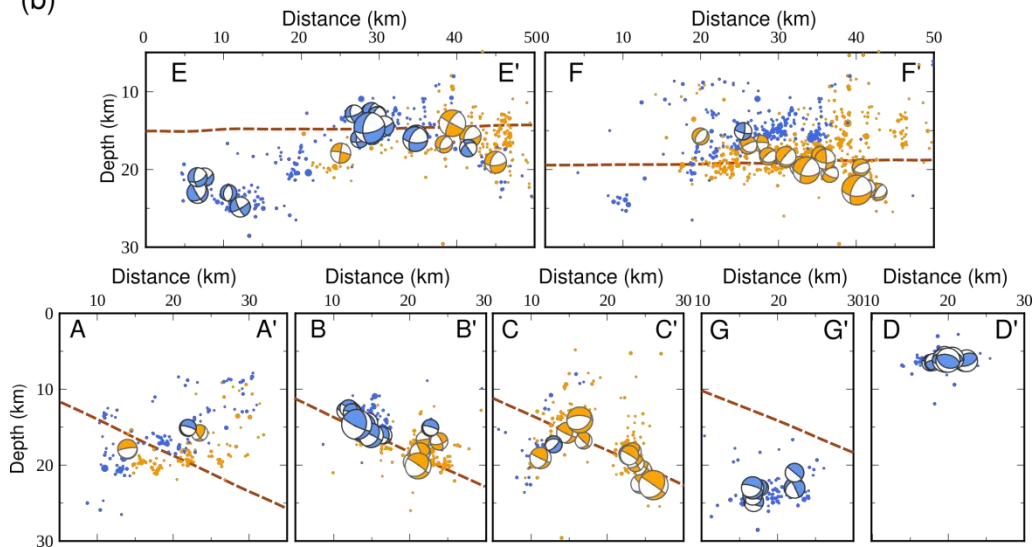
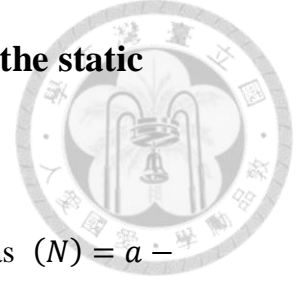


Figure 5.6 Fault settings for 2010 JiaShian and 2016 Meinong doublet events. 錯誤！尚未定義書籤。

(a) Map showing regional focal mechanisms and aftershock sequences (circles) denoted by orange for JiaShian and blue for Meinong earthquakes. Regional focal mechanisms are from AutoBATS MT catalog (Jian et al., 2018) or first motion method. The color of the beach ball shows the focal depth. The circles with thick outline are those events having focal mechanisms displayed on the map. The brown and blue dash boxes mark the fault areas of JSMN fault for the doublet events and two receiver faults, respectively.

(b) The cross-sections of profiles A to H. The dash brown lines mark the JSMN fault plane along each profile. To better illustrate two sequences in cross-sections, the beach balls are colored by orange for JiaShian and blue for Meinong aftershock sequences.

5.6 The frequency-magnitude distribution (FMD) and the static stress transfer in Southwestern Taiwan



The power law form of size distribution of earthquake is given as $(N) = a - bM$, where N is the cumulative number of earthquakes with magnitude larger than M , and a and b are two constants. The b -value, slope of the FMD, is believed varying temporally or spatially within different tectonic stress regime (Wyss and Lee, 1973; Zobin, 1979; Wiemer and Benoit, 1996; Wyss et al., 1997; Wiemer and Katsumata, 1999). Here, we examine the spatial differences and temporal variations of b -values for the JSMN fault and Southwestern Taiwan area. We calculate the b -values by using maximum likelihood (Aki, 1965) and follow the error estimation method proposed by

Shi and Bolt (1982): $\log(e) \frac{1}{\bar{M} - (M_c - \delta m/2)}$ and $2.3b^2 \left[\frac{\sum (M_i - \bar{M})^2}{n(n-1)} \right]^{\frac{1}{2}}$ respectively, where

\bar{M} is the mean magnitude of the catalog, M_c is the completeness of magnitude, δm is the bin size of magnitude, n is the number of earthquakes. The M_c is estimated by

searching the maximum curvature of the FMD (Wiemer and Wyss, 2000). The probability (Pr) of Akaike information criterion (AIC) is a statistic way to examine the reliability of differences in b -values between two earthquake groups. The probability

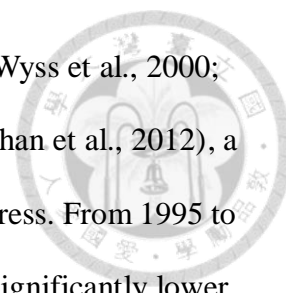
(Pr) of AIC is defined as $Pr \approx \exp\left(\frac{-\Delta AIC}{2} - 2\right)$, where $\Delta AIC = -2N \ln(N) +$

$2N_1 \ln\left(N_1 + N_2 \frac{b_1}{b} 2\right) + 2N_2 \ln\left(N_1 \frac{b_2}{b} 1 + N_2\right) - 2$, $N = N_1 + N_2$ and N_1, b_1 and

N_2, b_2 are event numbers, b -values for catalog 1 and 2 (Utsu, 1966, 1992; Wiemer and

Wyss, 2002). Following the criteria proposed by Wiemer and Wyss (2002), only when

Pr is larger than 0.95 or ΔAIC is larger than 2, the difference of b -values between two earthquake sets is considered statistically significant.



According to previous studies (Wiemer and Wyss, 1994, 1997; Wyss et al., 2000; Schorlemmer and Wiemer, 2005; Wiemer and Schorlemmer, 2007; Chan et al., 2012), a region showing low b-value suggests the local concentration of the stress. From 1995 to 2010 (before two mainshocks), the b-value in JS-MN fault (0.79) is significantly lower than in Southwestern Taiwan area (0.85) with Pr larger than 0.99. Previous study (Chen et al., 2016) also observed apparent low b-value inside our presumed JSMN fault. The lower b-value in the JS-MN fault than in the surrounding area accompanying with a ~50 years seismic quiescence imply that the JS-MN fault is the local stress concentration and accumulation zone than the rest of the Southwestern Taiwan (Chen et al., 2016). In addition to compare the spatial differences of b-value, we also analyze the annual b-value variations in JSMN fault zone and whole Southwestern Taiwan (SW-TW) by applying rigorous constraint. Only when the differences of b-value between the year and the previous year having Pr larger than 0.95 are taken into account (marked by solid circles In Figure 5.7) for temporal b-value variation analysis. The annual b-values from 1995 to 2010 gradually declined until the Jiashian mainshock (Figure 5.7a). Then the b-value shortly increases in one year. Therefore, we consider that the JS-MN fault was continuously locked and at the same time the stress accumulation continues for several decades before 2010 Jiashian earthquake. After 2 years of Jiashian earthquake, not only the JS-MN fault but also the entire SWTW area becomes totally quiet for a whole year (Figure 5.7). Then, in JSMN fault area, the b-values continue to decline again until 2016 Meinong earthquake. Not like JSMN fault, we don't see obvious temporal b-value variations for whole SWTW area (Figure 5.7b). Based on the temporal evolution of b-value and seismic activities, we suspect that the accumulated stress for at least 50 years was not released by a single earthquake at once but by two comparable strong

earthquakes. We proposed that the Mw 6.2 Jiashian earthquake initiated the doublet sequence at deeper eastern part of the JSMN fault but may only release partial stress or it may trigger the western shallow area to further release more stress: the Mw 6.4 Meinong earthquake.

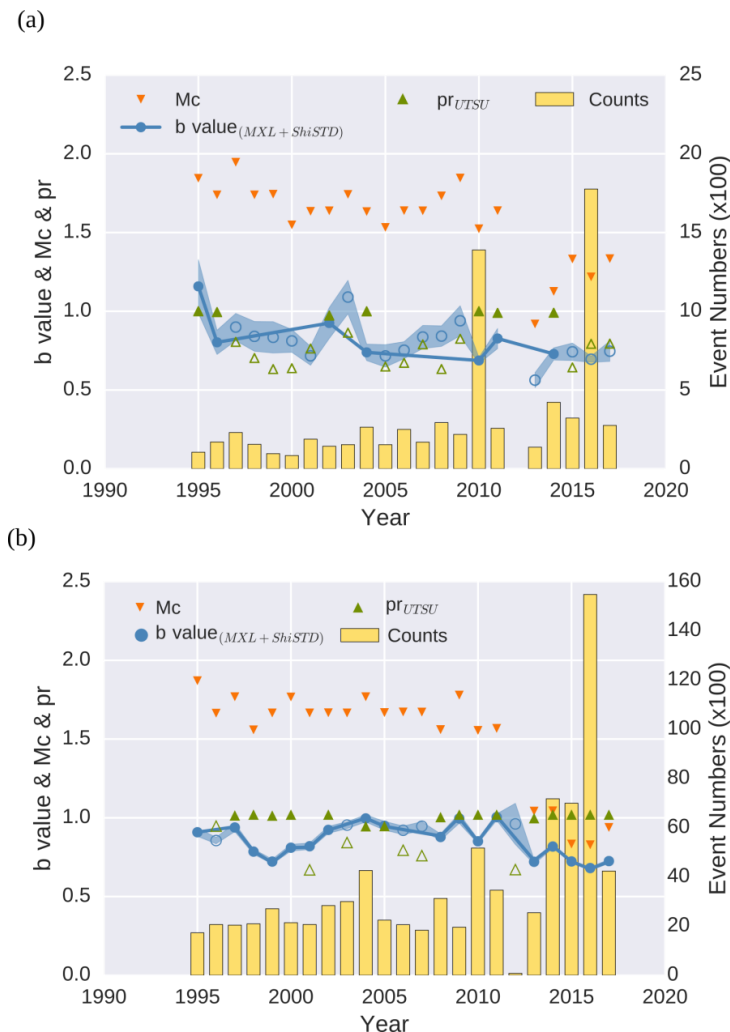
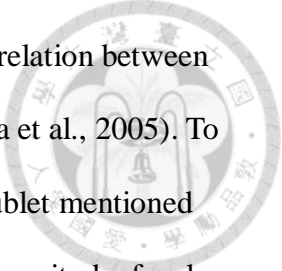
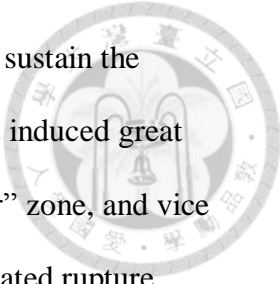


Figure 5.7 Earthquake numbers and temporal b-value variation in JSMN fault and Southwestern Taiwan. The b-value (circles), Mc (inverted triangle) and earthquake numbers (bar) as a function of time in (a) JSMN fault area and (b) SW-Taiwan area. The statistical significant probability (Pr) of each year denoted by triangles is calculated between the b-values of its corresponding and previous year. The symbols are solid when the Pr of that year is larger than 0.95. The shading blue zone shows the b-value uncertainties which are determined by the standard deviation of b-value (Shi and Bolt, 1982). Mc is determined by the maximum curvature strategy (Wiemer and Wyss, 2000). It's worth noted that we obtain the Mc pushing to below 1.0 after 2012 because the CWB has improved the seismicity detections by upgrading and installing borehole seismometers.

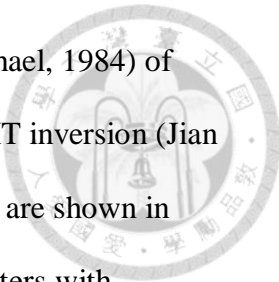


The Coulomb static stress change is widely studied to reveal the relation between the aftershocks and the static stress transfer (Lin and Stein, 2004; Toda et al., 2005). To inspect the potential triggering between the Jiashian and Meinong doublet mentioned above, we calculate the slip vectors approximated from the moment magnitude, focal mechanism and then distributed them into the subfaults following the source energy radiator locations from our BP results. Based on the sensitivity study of Coulomb stress change by Zhan et al. (2011), they concluded that focal depth and receiver fault geometry are more important on stress change outside the mainshock rupture zone. We also found the stress change on the receiver fault keeps similar pattern as long as the fault geometry of the triggering mainshock is the same; in other words, we have similar stress change distribution on the receiver faults no matter we have even-distributed slip-vectors on the whole rupture fault or contagious distribution of slip vectors following our BP results. Figure 5.8 shows the coulomb stress change results. After the Jiashian earthquake, the shallower area of the JSMN fault where the Meinong earthquake ruptured imparted a notable positive static stress change (>2 bars) but rare aftershocks were triggered by Jiashian earthquake. Likewise, the Meinong earthquake also delivered positive static stress (>1 bar) at deeper zone where the Jiashian earthquake ruptured but was not able to trigger any aftershocks (Figure 5.8d). In summary, both Jiashian and Meinong earthquakes induce positive stress changes across two rupture zones of the fault which are much larger than the proposed threshold (0.1 bar) of stress change (e.g., King et al. 1994; Stein 1999) for potential earthquake triggering (Figure 5.8c&d). However, the stress disturbances induced by Jiashian or Meinong earthquake didn't trigger aftershocks on each other's rupture zones. Following previous discussions about overall continue low b-value for the last



20 years in JSMN fault; we already suspect it may be a strong fault to sustain the concentration of regional stress. In addition, the first “deeper” doublet induced great increases of static stress and failed to trigger aftershocks at “shallower” zone, and vice versa. Based on above observations, we proposed that these two separated rupture zones are two strong asperities and not easy to be triggered. The occurrence of this doublet sequence started at the deeper strong asperity on the JS-MN fault, the 2010 Jiashian earthquake. And the 2010 Jiashian earthquake might release accumulated stress partially since the b-value continued declining until 2016 Meinong earthquake (Figure 5.7a). The 2016 Meinong earthquake might be triggered but it took 6 years for the shallower asperity to rupture and release more stress. The long delay triggering has been addressed by previous studies, such as 1992 Landers & 1999 Hector Mine earthquakes (Parsons and Dreger, 2000; Freed and Lin, 2001; Gomberg et al., 2001) and 1994 Northridge earthquake (Stein et al., 1994).

As the 2016 Meinong earthquake occurred, other than the aftershocks surround the epicenter, it also immediately triggered one western deeper (>20 km) cluster beneath Tainan (TN for short) which was adjacent to the rupture terminus of the mainshock (Figure 5.3). Within a week, another eastern group of shallow normal faulting earthquakes beneath South Central Mountain Range (SCM for short) was also triggered by Meinong earthquake (Figure 5.3). Along the profile of rupture propagation, we believe that the TN and SCM aftershock clusters not relate with the proposed JSMN fault. We can calculate the Coulomb stress change upon the receiver faults of two distance clusters to further approve the triggering of stress transfer from Meinong earthquake. However, there are absent of any identified fault structures linking to both clusters. Hence, we tried to have rough fault geometry approximations by the average



stress axes which are determined by the stress inversion method (Michael, 1984) of regional focal mechanisms from first-motion method or AutoBATS MT inversion (Jian et al., 2018). The fault planes of two clusters from the stress inversion are shown in Figure 5.8b and Figure B4. Then we also isolated two earthquake clusters with earthquake interaction model (Reasenberg, 1985) of 1 year seismicity after Meinong event and relocated the hypocenters by Hypo-DD technique (Waldhauser and Ellsworth, 2000). The resultant aftershock distributions of TN and SCM clusters demonstrate two fault zones clearly (Figure 5.6a). From the map view of TN cluster (Figure 5.6a), the aftershock distribution is more consistent with the fault plane having strike in N-S direction and eastward dipping angle. In addition, we obtain positive static stress change only when this N-S striking sub-vertical fault plane is the receiver fault (Figure 5.8b, cross-section DD'). As the normal faulting SCM cluster, the stress inversion result shows that two nodal planes are both in NW-SE striking direction. After taking either fault planes as the receiver fault, the resultant static stress are all positive which clarify that the SCM cluster was triggered by the Meinong earthquake (Figure 5.8b, cross-section CC') no matter which one is the rupture fault plane. After reviewing the cross-sections of two possible fault planes, the NE-ward dipping fault plane seems to be more consistent with distribution of SCM cluster.

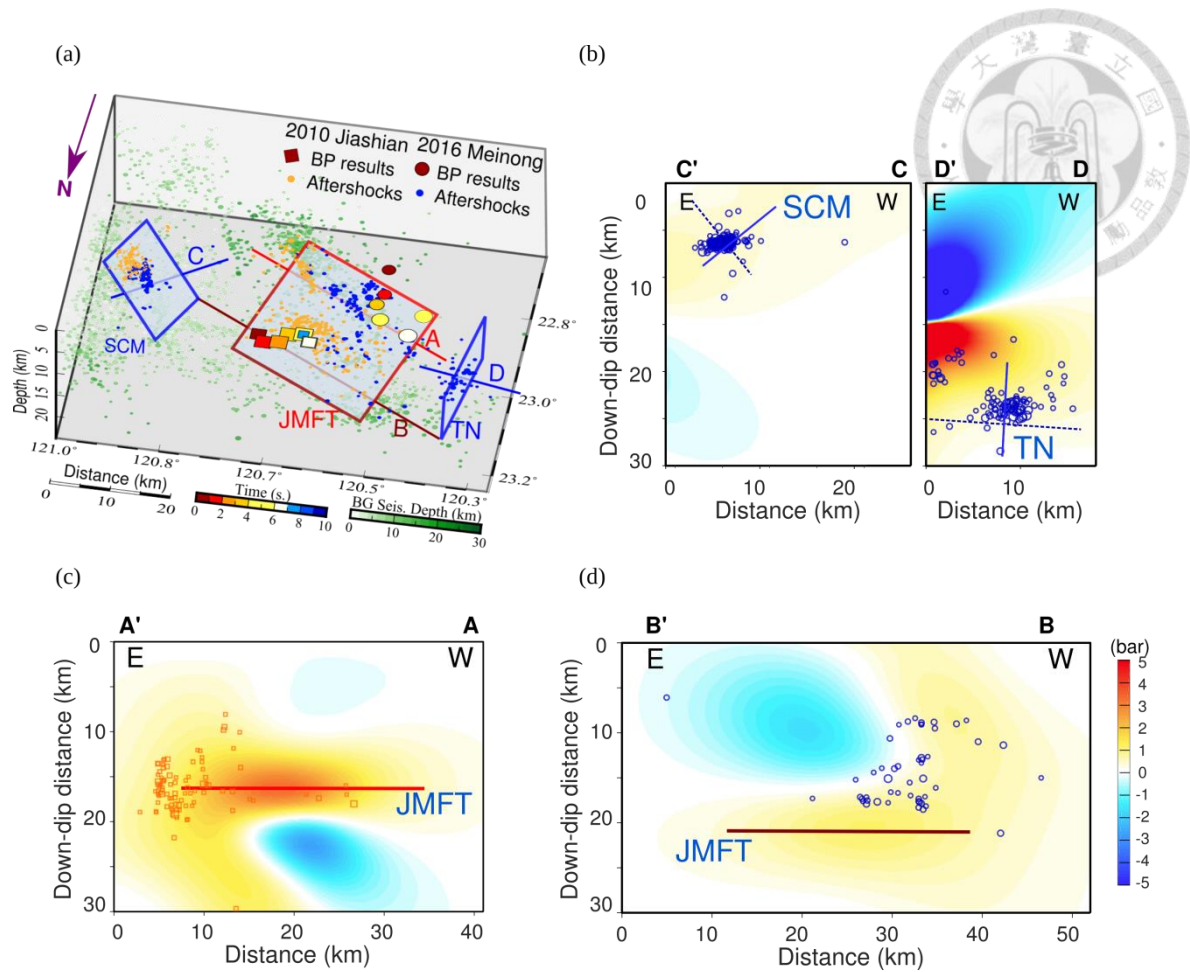



Figure 5.8 3D sketch of fault geometry settings and the Coulomb stress change induced by Jiashian and Meinong doublet.

(a) 3D sketch showing JS-MN fault (denoted as JMFT) and receiver faults of South Central Mountain (SCM) and Tainan faults (TN). The BP results of Jiashian and Meinong earthquakes are shown in diamonds and circles, respectively. The symbols are scaled with the pseudo-power of MUSIC BP images and colored according to the lapsed time. The Jiashian and Meinong aftershocks sequence are denoted by orange and blue dots, respectively. Green gradient dots show the background seismicity ($M_L \geq 2$) before Jiashian earthquake. (b) Cross-sections of Coulomb stress change on the receiver faults of SCM (CC') and TN (DD') induced by 2016 Meinong earthquake. The blue solid and dash lines mark the receiver fault and the conjugate nodal plane. Cross-sections of Coulomb stress change along the (c) shallower part induced (red line) and (d) deeper part (brown line) of the JSMN fault induced by Jiashian and Meinong earthquakes, respectively. The Jiashian and Meinong aftershocks are shown in red and blue circles, respectively.

5.7 Conclusions



In this chapter, I conclude that the rupture of 2010 Jiashian earthquake propagates N80°W ~ N60°W and updip of ~20° for about 11 km by the integrated BP images of P- and sP-waves recorded in EU array and 3D directivity analysis results. The rupture speed is about 2.0~2.2 km/s. As the 2016 Meinong earthquake, the rupture extend 16~18 km to N60°W with speed of 2.5 km/s (Jian et al., 2017). I propose that the Jiashian and Meinong earthquakes as a doublet sequence which occurred on a common unknown buried fault based on following observations: closed epicenter, similar focal mechanism and rupture properties. Moreover, the BP results and aftershock distribution indicate that two earthquake rupture independently in separate zones. Two relocated aftershock sequences and the BP results are well consistent with this JSMN fault plane which is determined from the USGS-MT solution of Meinong earthquake. The b-value on the JSMN fault is overall lower than the surrounding SW-Taiwan area for at least 20 years. The low b-value suggests the local stress accumulation on the JSMN fault. The Coulomb stress change approves that the 2016 Meinong earthquake triggered two distant aftershock clusters in Tainan and south central mountain range. However, two mainshocks on deeper and shallower rupture zones both transfer notable stress increases across the rupture zones without producing any triggered small events reciprocally. Low b-value suggests potential stress accumulation on the strong JSMN fault and troubling to trigger aftershocks on either rupture zones may imply two strong asperities on the JSMN fault. In conclusion, the doublet initiated at the eastern deep asperity, 6 years later, delayed triggered Meinong earthquake, the shallower asperity, released more accumulated stress which also caused great casualties unfortunately.

Chapter 6 Appendixes



6.1 Supplementary material of Chapter 4

This supplementary material contains four figures provided to support the results presented in the paper. Figure A1 shows the epicenter of the main shock and distribution of dense broadband stations in Europe (EU) and Australia (AU) and recorded vertical velocity seismograms used in our BP study. Figure A2 are the corresponding synthetic waveforms computed by the frequency-wavenumber (F-K) method assuming a CMT point-source model for the Meinong earthquake and 1-D velocity structures. Figure A3 shows variations of P- and S-wave velocity in the crust near the source region obtained from a 3D local tomography model. In addition, we show the 1-D P and S velocity profiles that can best predict the observed arrival times of depth phases, pP and sP, relative to P for a 16-km deep Meinong earthquake. Figure A4 shows a synthetic test to demonstrate whether the high-resolution MUSIC BP method is capable of resolving an assumed source scenario similar to the Meinong earthquake using the synthetic P and sP waveforms recorded by the same AU and EU stations.

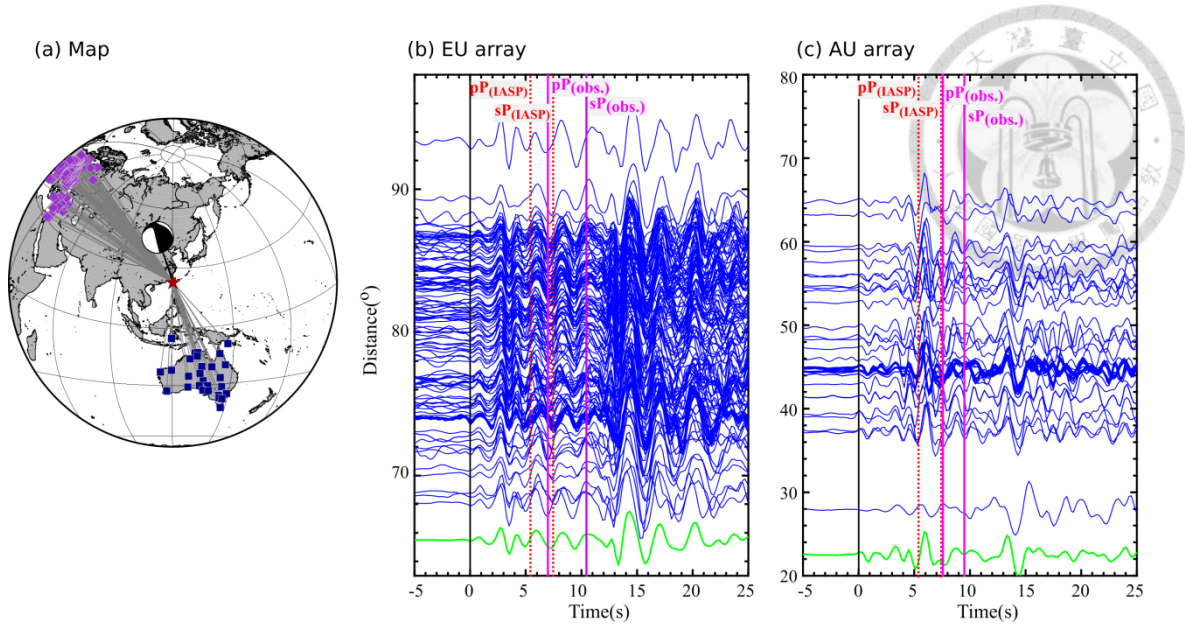


Figure A1. The epicenter and array distribution and the aligned vertical velocity waveforms of two arrays.

(a) The epicenter (star) and CMT solution of the 2016 Meinong earthquake and distribution of broadband seismic stations (squares) from the European (EU) and Australian (AU) network used in our BP rupture imaging. (b)-(c) Vertical velocity seismograms recorded at the EU and AU stations, respectively, plotted as a function of epicentral distance. The waveforms are aligned on the first P arrivals at zero time denoted by black lines after being bandpass filtered between 0.5 and 1.5 Hz. Solid purple and dashed red lines mark the observed and IASP91 predicted arrival times of pP and sP phases, respectively. The traces shown by green lines on the bottom of the plots are the stacks of all the aligned waveforms from each array.

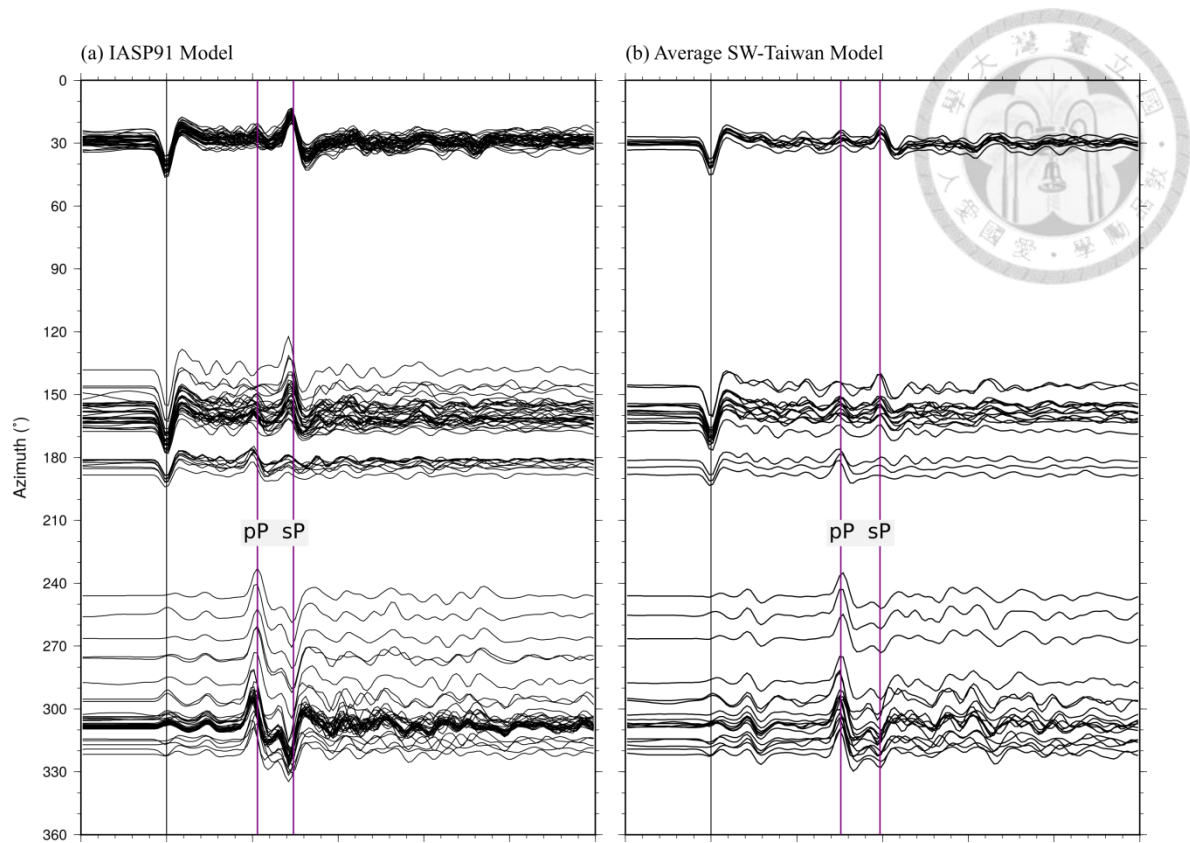


Figure A2. Synthetic velocity seismograms on the vertical component compared with the observed ones shown in Fig. 3(a).

The synthetics are computed by the F-K method assuming a 1-D velocity structure from (a) the IASP91 model and (b) laterally-average local tomographic model in SW Taiwan [Huang et al., 2014] (Figure A3b). The CWB located hypocenter and USGS CMT solution are adopted as the point-source model for the Meinong earthquake. The pP and sP arrival times for the local velocity model, similar to the observed depth-phase arrivals, are delayed by about 2 s relative to those for IASP91. The predicted sP/pP ratios shown in Fig. 3(d) are estimated by the peak amplitudes of the pP and sP phases from the IASP91 synthetics.

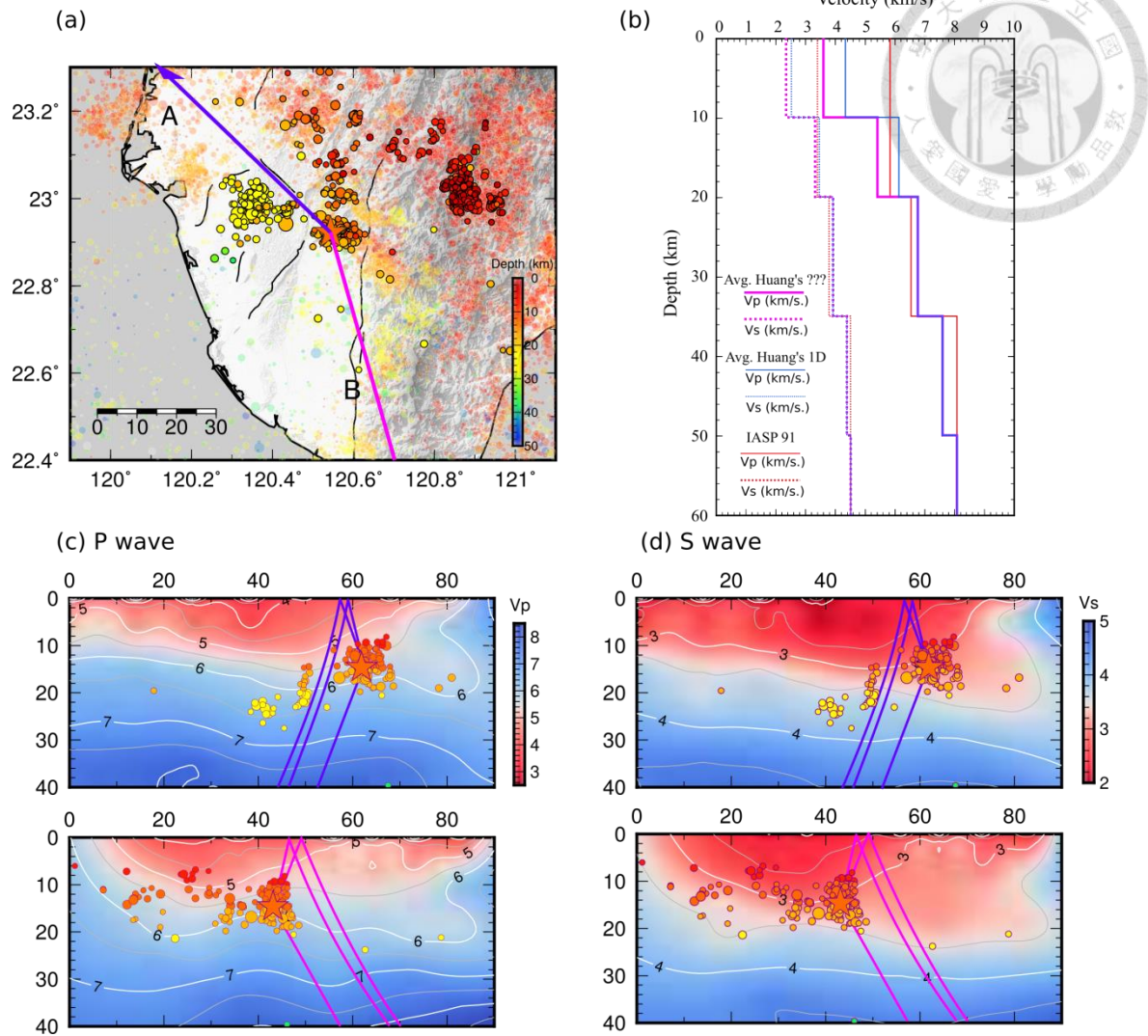


Figure A3 The P-wave ray paths, 1D average velocity model and the tomographic images along the ray path.

(a) Map showing the surface projection of P-wave ray paths to the EU (blue) and AU (magenta) array in the source area and two vertical cross sections of AA' and BB' along which P- and S-wave velocity (V_p and V_s) structures from Huang et al. [2014] are shown in (c) and (d). The epicenters of the Meinong main shock, aftershocks and background seismicity are also shown by star, circles, and dots, respectively, with color coded by hypocentral depth. (b) Comparison of the 1-D V_p and V_s structures at 0-60 km depth, obtained from the IASP91, laterally-average local model of Huang et al. [2014], and our study that matches the observed pP-P and sP-P differential times. (c)-(d) V_p and V_s structures along AA' and BB' cross sections, where the ray paths of P, pP and sP waves to the EU and AU array are shown with the corresponding blue and magenta colors.

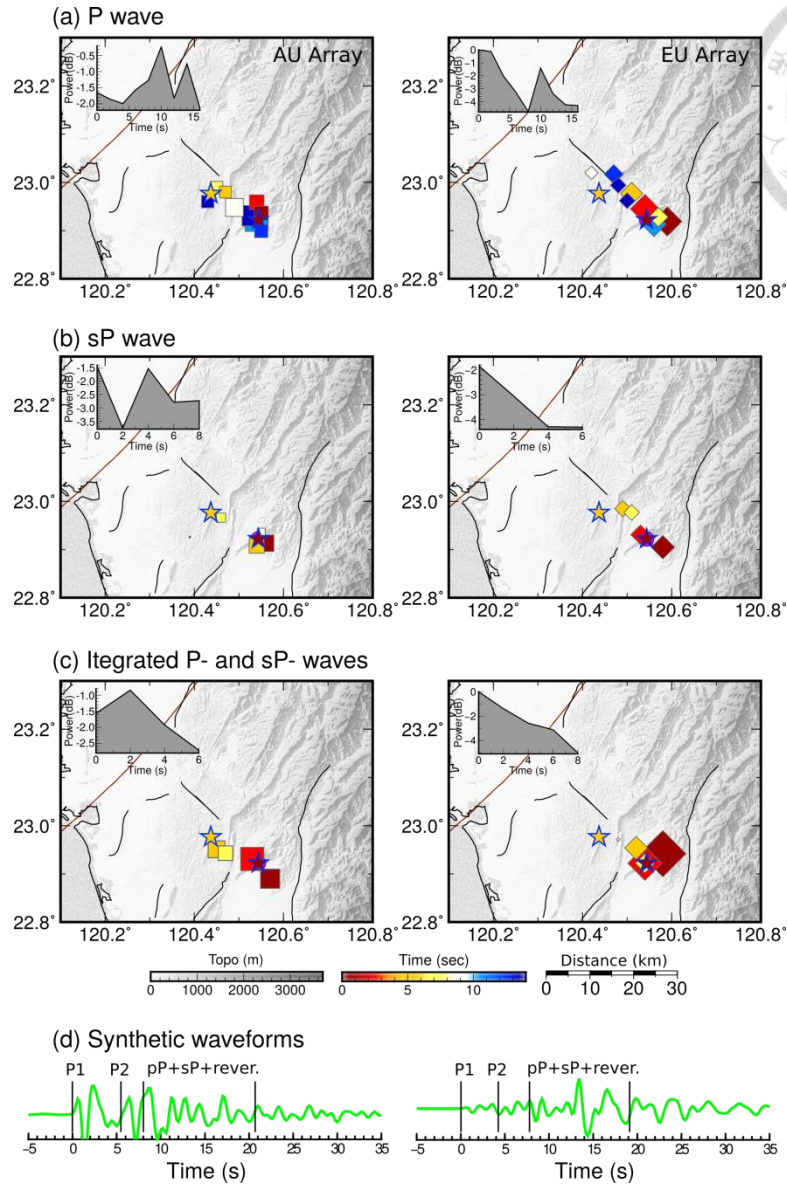
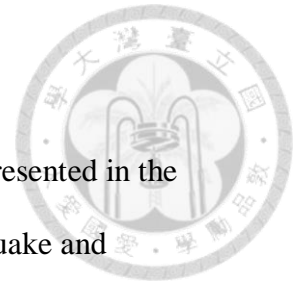


Figure A4 Test for recovery of a synthetic source scenario by the MUSIC BP method.

The test model comprises two point-source subevents (P1 and P2) with the locations denoted by stars. Considering the rupture directivity toward the EU array, the onset times of the two radiation sources are set to be separated respectively by 5.4 s and 4.2 s in the synthetic waveforms recorded at the AU and EU array. The same BP procedure applied to the real data is adopted to image assumed source scenario using the F-K synthetic seismograms for the 1-D local model from Huang et al. (2014). The space-time distributions of the strongest radiators imaged with (a) ~20-s long wave trains including direct P, depth phases, and following reverberations, and (b) ~8-s wave trains starting from the onset sP arrivals of subevent P1. (c) The source images which combine the BP results obtained with P and sP waves individually, indicating that the time and position of the two radiation sources can be well recovered by the MUSIC BP imaging, particularly seen from the AU array. (d) Stacks of all synthetic waveforms from AU and EU array.

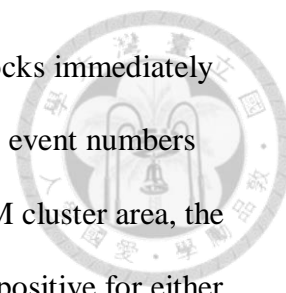
6.2 Supplementary material of Chapter 5



The supplementary figures are provided to support the results presented in the chapter 5. Figure B1 shows the epicenter of the 2010 Jiashian earthquake and distribution of seismic stations in Europe (EU) and Australia (AU) and recorded vertical velocity seismograms used in our BP study. Figure B2 are the corresponding synthetic waveforms computed by the frequency-wavenumber (F-K) method assuming a single or two subevents models for the Jiashian earthquake. Figure B3 shows the P- and S-wave velocity structures near the Jiashian and Meinong epicenters obtained from a 3D local tomography model.

We performed stress inversion of regional focal mechanisms as the alternative approximations on receiver fault geometry for Coulomb stress change analysis. The stress inversion results of Southern Central Mountain range and Tainan clusters are shown in Figure B4. In Chapter 5, we proposed a JSMN fault as the causative fault for the Jiashian and Meinong doublet events and calculate the b-value and Coulomb stress change. The alternative assumption is that the Jiashian and Meinong earthquakes were two different fault rupture events. The fault geometries of two earthquakes are from the USGS MT solutions as shown in Figure B7c. Figure B5 shows the earthquake numbers and temporal b-value variations in the Jiashian, Meinong fault areas, the Southern Central Mountain Range and the Tainan area.

Figure B6 shows the Coulomb stress change based on the two-separated fault assumption for further comparison with the results from single causative fault of Jiashian and Meinong earthquakes (Figure 5.8c&d). We also like to examine how the 2010 Jiashian earthquake cause the stress perturbations on the SCM or TN receiver



faults. Although the 2010 Jiashian earthquake did not trigger aftershocks immediately in the south central mountain range like Meinong earthquake did, the event numbers did increase during 2010~2011 in SCM area (Figure B7). As the SCM cluster area, the Coulomb stress changes induced by the Jiashian earthquake are also positive for either fault planes as shown in Figure B7. We also found the increase of stress change induced by Jiashian is actually larger than by Meinong earthquakes (Figure 5.8 & Figure B7). However, more studies are necessary to understand the reason why the Meinong earthquake triggered more SCM aftershocks and took much shorter time than Jiashian earthquake did (Figure B5c). As the TN cluster, not like Meinong earthquake, the Jiashian earthquake induce much less stress perturbation on the TN receiver fault and failed to trigger the TN cluster like the Meinong earthquake did (Figure 5.8b & Figure B7).

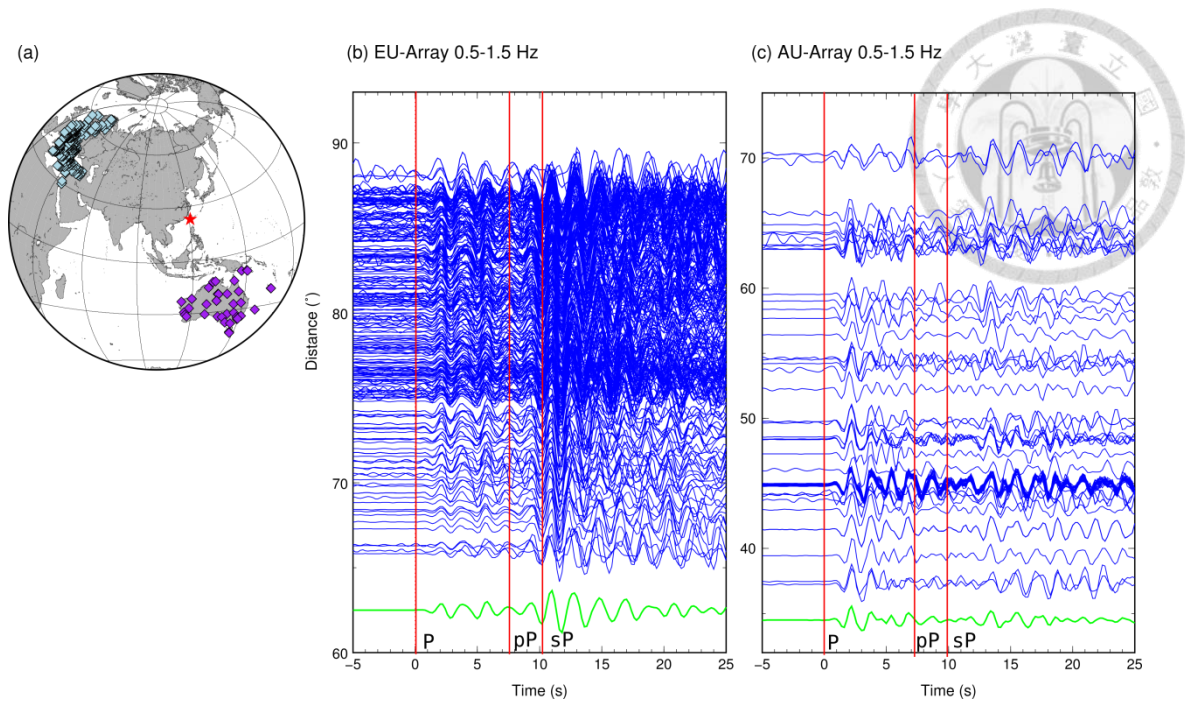


Figure B1 The seismic arrays and aligned P waves used for the BP images of 2010 Jiashian earthquake. (a) The epicenter of 2010 Jiashian earthquake and seismic stations from the European (EU) and Australian (AU) used in our BP rupture imaging. (b)-(c) Vertical velocity seismograms recorded at the EU and AU stations, respectively, plotted as a function of epicentral distance. The waveforms are aligned on the first P arrivals at zero time. The red lines mark the arrival times of pP and sP phases predicted by IASP91 model. The green traces at the bottom are the stacks of the aligned waveforms from each array.

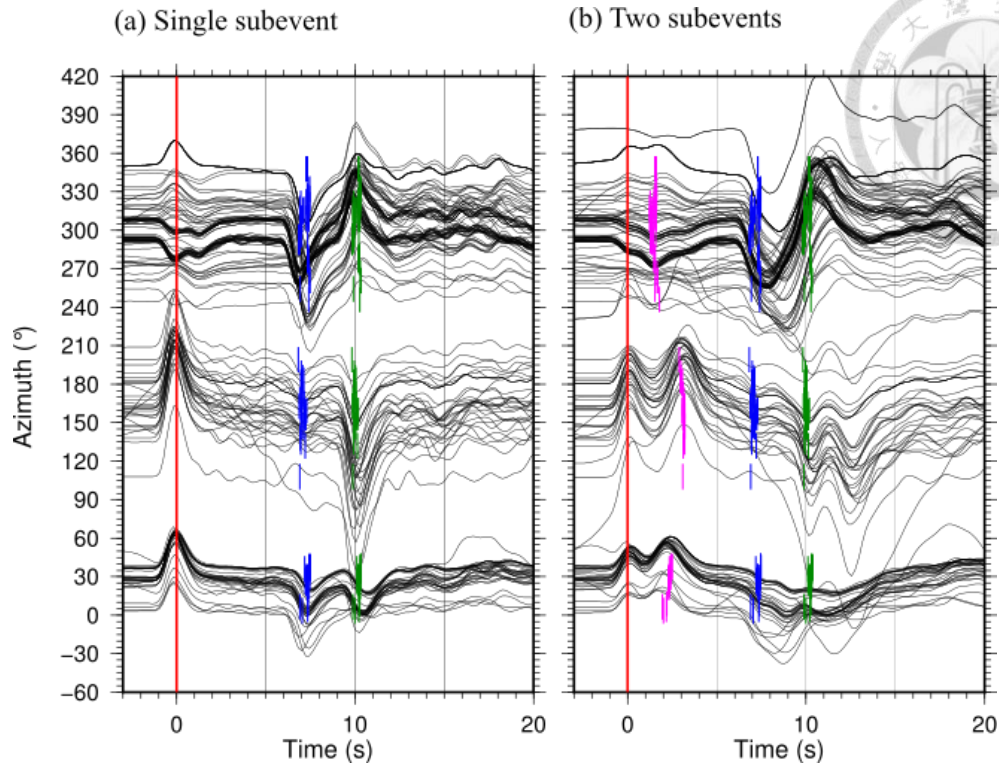


Figure B2 Synthetic velocity seismograms for comparison with the observed ones shown in Figure 5.4. Synthetic waveforms calculated by using FK method and USGS MT solution with (a) single and (b) two subevents. The epicenter of the second subevent is assumed by setting the rupture direction, speed and distance from the BP imaging and directivity analysis results. The pink short lines denote the peaks of second subevent. The arrivals of pP and sP phases from first subevent are marked with the short blue and green lines.

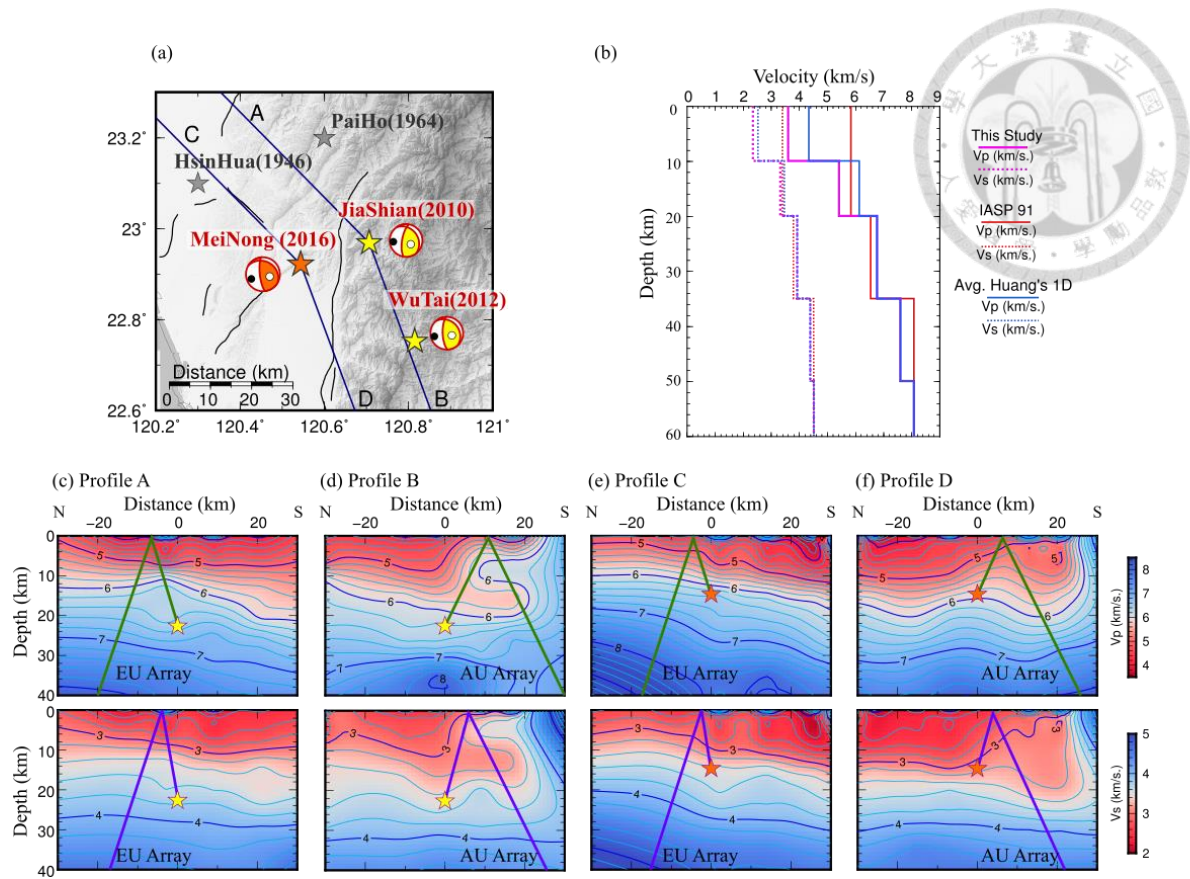


Figure B3 1D average velocity models and tomographic images along the ray paths of P and depth phases.

(a) Map showing the surface projection of P-wave ray paths to the EU (blue) and AU (magenta) array from the hypocenters of Jiashian and Meinong earthquakes. The epicenters (stars) and focal mechanisms of Jiashian and Meinong earthquakes are also shown. Vertical cross sections which P- and S-wave velocity (V_p and V_s) structures from Huang et al. (2014) are shown in (c)-(f). (b) Comparison of the 1-D V_p and V_s structures at 0-60 km depth, obtained from the IASP91, laterally-average local model of Huang et al. (2014), and our study that matches the observed pP-P and sP-P differential times of Meinong earthquake (Jian et al., 2017). (c)-(f) Cross-sections of V_p and V_s structures along A-D profiles, where the ray paths of pP and sP waves to the EU and AU array are shown with the corresponding green and blue lines.

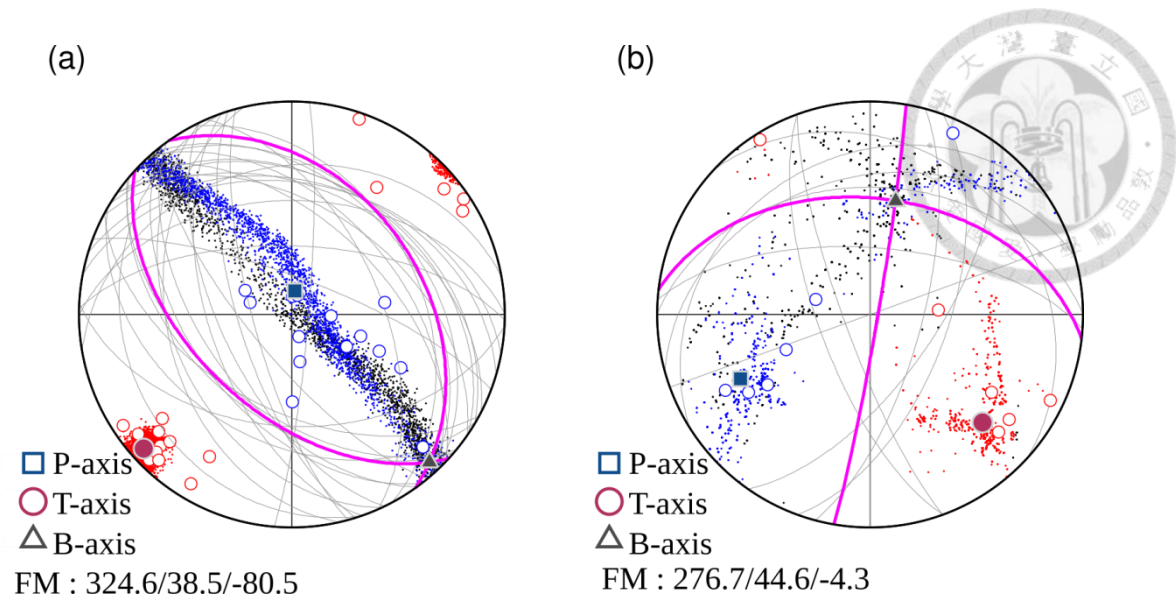
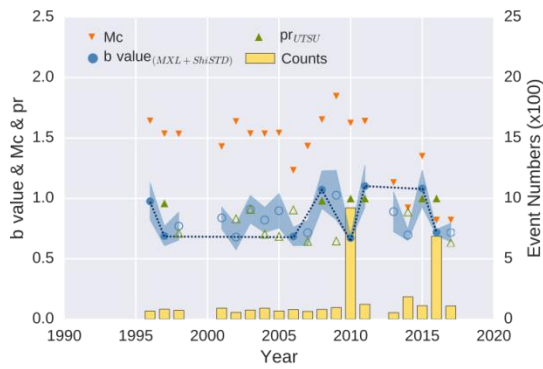


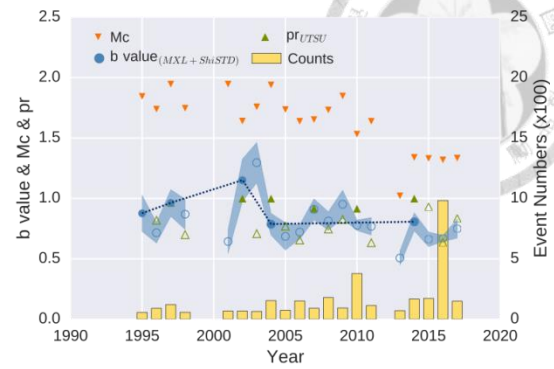
Figure B4 The stress inversion results.

The stress inversion for aftershock clusters of (a) Southern Central Mountain Range and (b) Tainan. The open circles represent the input P- (blue) and T-axes (red) of regional focal mechanisms. The resultant P- and T-axes are denoted by solid blue square and red circles, respectively. The thick magenta lines are the fault planes corresponding to the resultant P-,T-axes. The blue, red and black dots are 2000 random P-,T- and B- axes picked by the Monte-Carlo method for the purpose showing 95% confidence level.

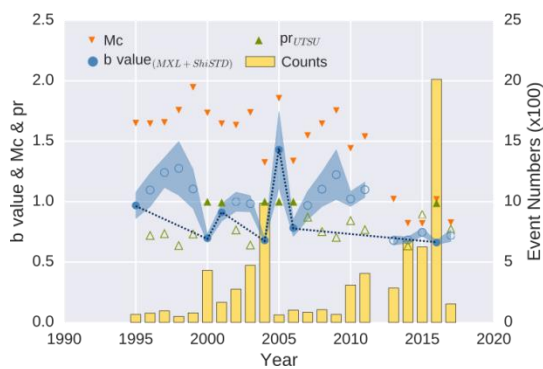
(a) Jiashian Area



(b) Meinong Area



(c) Southern Central Mountain Area



(d) Tainan Area

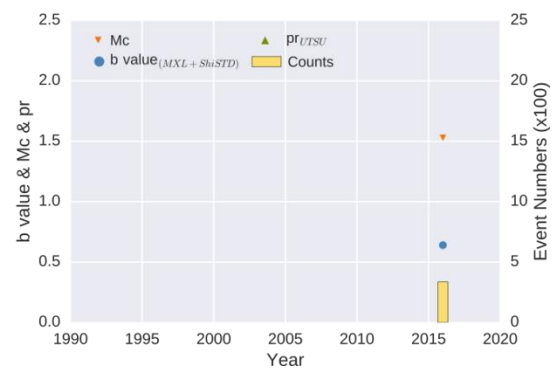


Figure B5 The earthquake numbers and temporal b-value variation.

The b-value (circles), Mc (inverted triangle) and earthquake numbers (bar) as a function of time in (a) Jiashian earthquake, (b) Meinong earthquake, (c) Southern Central Mountain and (d) Tainan areas. For the assumption of two different causative faults of 2010 Jiashian and 2016 Meinong earthquakes, the corresponding fault geometries of two events are illustrated in Figure B6a. The symbols and explanations are the same as those in the Figure 5.7.

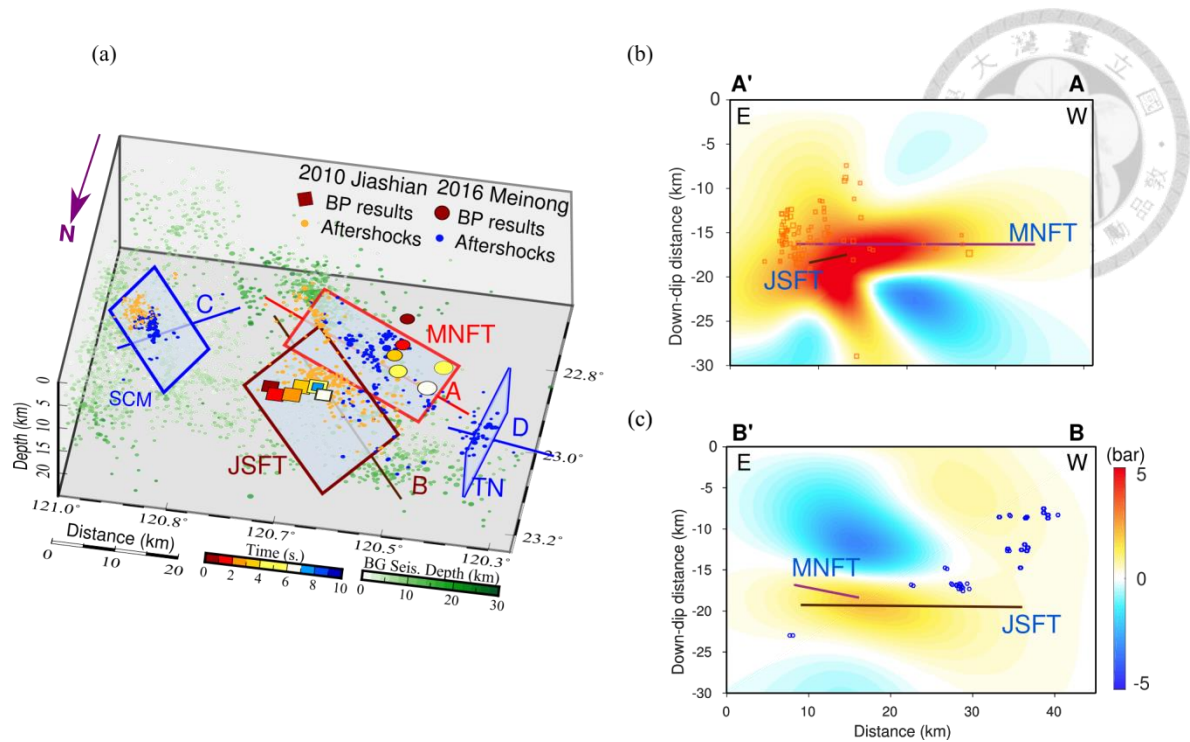


Figure B6 The 3D sketch of two causative faults for Jiashian and Meinong doublets and the Coulomb stress change induced by two earthquakes.

(a) The 3D sketch of the fault geometries based on the assumption that two earthquake occurred on two separated fault planes (denoted as JSFT and MNFT). The Coulomb stress change on (b) the MNFT induced by 2010 Jiashian earthquake and (c) the JSFT induced by 2016 Meinong earthquake. The symbols and explanations are the same as those in the Figure 5.8.

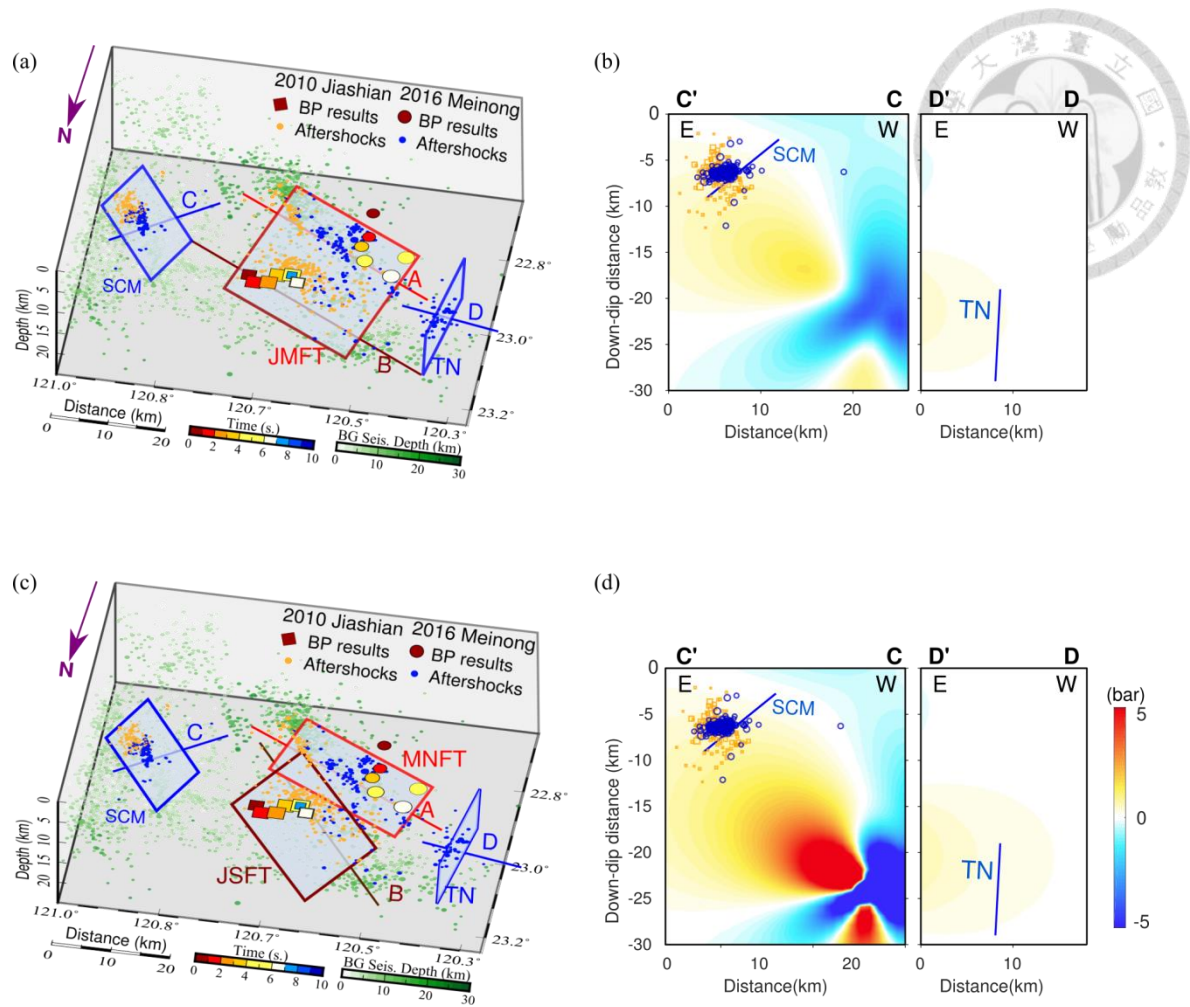
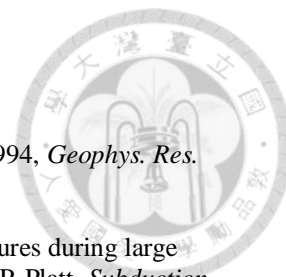


Figure B7 The 3D sketch of JSMN fault or two-separated faults and the Coulomb stress change across the SCM and TN fault areas induced by 2010 Jiashian earthquake.

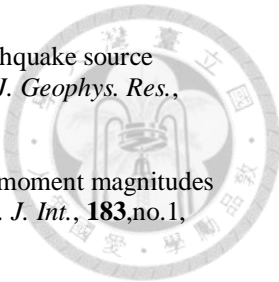
The 3D sketch of Jiashian fault geometry based on the assumption that Jiashian and Meinong occurred on (a) a single causative fault (JMFT) or (c) two separated faults (denoted as JSFT and MNFT). (b)&(d) The cross-sections of Coulomb stress change across the SCM (CC') and TN (DD') fault area after 2010 Jiashian earthquake with the fault geometries shown in (a) and (c) respectively. The symbols and explanations are the same as those in the Figure 5.8.

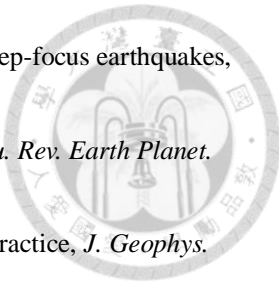
Reference

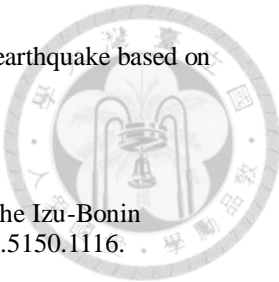
- Aki, K. (1965). Maximum likelihood estimate of b in the formula $\log N = a - bM$ and its confidence limits, *Bull. Earthq. Res. Inst., Tokyo Univ.*, **43**, 237–239.
- Aki, K., and P. G. Richards (1980). *Quantitative seismology: Theory and methods*, Freeman, San Francisco.
- Allen, R. V. (1978). Automatic earthquake recognition and timing from single traces, *Bull. Seismol. Soc. Am.*, **68**,no.5, 1521–1532.
- Angelier, J., T.-Y. Chang, J.-C. Hu, C.-P. Chang, L. Siame, J.-C. Lee, B. Deffontaines, H.-T. Chu, and C.-Y. Lu (2009). Does extrusion occur at both tips of the Taiwan collision belt? Insights from active deformation studies in the Ilan Plain and Pingtung Plain regions, *Tectonophysics*, **466**,no.3-4, 356–376, doi: 10.1016/j.tecto.2007.11.015.
- Antolik, M., D. Dreger, and B. Romanowicz (1996). Finite fault source study of the great 1994 deep Bolivia earthquake, *Geophys. Res. Lett.*, **23**,no.13, 1589–1592, doi: 10.1029/96gl00968.
- Bernardi, F., J. Braunmiller, U. Kradolfer, and D. Giardini (2004). Automatic regional moment tensor inversion in the European-Mediterranean region, *Geophys. J. Int.*, **157**,no.2, 703–716, doi: 10.1111/j.1365-246x.2004.02215.x.
- Bethmann, F., N. Deichmann, and P. M. Mai (2011). Scaling relations of local magnitude versus moment magnitude for sequences of similar earthquakes in Switzerland, *Bull. Seismol. Soc. Am.*, **101**,no.2, 515–534, doi: 10.1785/0120100179.
- Bormann, P. (Ed. . (2012). New manual of seismological observatory practice (NMSOP-2), edited by P. Bormann, *IASPEI, GFZ German Research Centre for Geosciences, Potsdam*; <http://nmsop.gfz-potsdam.de>, doi: 10.2312/GFZ.NMSOP-2.
- Braunmiller, J., U. Kradolfer, M. Baer, and D. Giardini (2002). Regional moment Tensor determination in the European-Mediterranean area - initial results, *Tectonophysics*, **356**,no.1-3, 5–22, doi: 10.1016/s0040-1951(02)00374-8.
- Cambaz, M. D., and A. K. Mutlu (2016). Regional Moment Tensor Inversion for Earthquakes in Turkey and Its Surroundings: 2008–2015, *Seismol. Res. Lett.*, **87**,no.5, 1082–1090, doi: 10.1785/0220150276.
- Chan, C.-H., and Y.-M. Wu (2012). A seismicity burst following the 2010M 6.4 Jiashian earthquake—Implications for short-term seismic hazards in southern Taiwan, *J. Asian Earth Sci.*, **59**, 231–239.
- Chan, C.-H., Y.-M. Wu, T.-L. Tseng, T.-L. Lin, and C.-C. Chen (2012). Spatial and temporal evolution of b -values before large earthquakes in Taiwan, *Tectonophysics*, **532**, 215–222.
- Chen, C., S. Chang, and K. Wen (2017). Stochastic Finite-Fault Modeling of Ground Motions from the 2016 Meinong Taiwan earthquake, in *EGU General Assembly Conference Abstracts*, vol. 19, p. 2082.
- Chen, K.-C., W.-T. Liang, Y.-H. Liu, W.-G. Huang, and J.-H. Wang (2008). Seismic moments of Taiwan's earthquakes evaluated from a regional broadband array, *Earth Planets and Space*, **60**,no.6, 559–564, doi: 10.1186/bf03353118.
- Chen, R.-Y., H. Kao, W.-T. Liang, T.-C. Shin, Y.-B. Tsai, and B.-S. Huang (2009). Three-dimensional patterns of seismic deformation in the Taiwan region with special implication from the 1999

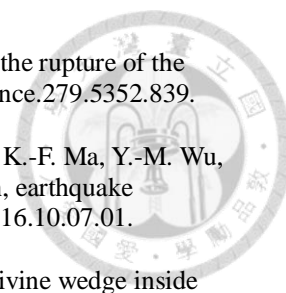


- Chi-Chi earthquake sequence, *Tectonophysics*, **466**,no.3-4, 140–151, doi: 10.1016/j.tecto.2007.11.037.
- Chen, W.-P. (1995). En echelon ruptures during the great Bolivian earthquake of 1994, *Geophys. Res. Lett.*, **22**,no.16, 2261–2264, doi: 10.1029/95GL01805/full.
- Chen, W.-P., L.-R. Wu, and M. A. Glennon (1996). Characteristics of multiple ruptures during large deep-focus earthquakes, edited by S. H. K. D. W. Scholl G. E. Bebout and J. P. Platt, *Subduction Top to Bottom*, 357–368, doi: doi: 10.1029/GM096p0357.
- Chen, Y., and L. Wen (2015). Global large deep-focus earthquakes: Source process and cascading failure of shear instability as a unified physical mechanism, , **423**., 134–144, doi: 10.1016/j.epsl.2015.04.031.
- Chen, Y., L. Wen, and C. Ji (2014). A cascading failure during the 24 May 2013 great Okhotsk deep earthquake, *J. Geophys. Res.*, **119**,no.4, 3035–3049, doi: 10.1002/2013jb010926.
- Chen, Y.-L., S.-H. Hung, J.-S. Jiang, and L.-Y. Chiao (2016). Systematic correlations of the earthquake frequency-magnitude distribution with the deformation and mechanical regimes in the Taiwan orogen, *Geophysical Research Letters*, **43**,no.10, 5017–5025.
- Cheng, S. N., and Y. T. Yeh (1989). *Catalog of the Earthquakes in Taiwan from 1604 to 1988*, Institute of Earth Sciences, Academia Sinica.
- Ching, K.-E., R.-J. Rau, J.-C. Lee, and J.-C. Hu (2007). Contemporary deformation of tectonic escape in SW Taiwan from GPS observations, 1995-2005, *Earth Planet. Sci. Lett.*, **262**,no.3-4, 601–619, doi: 10.1016/j.epsl.2007.08.017.
- Clinton, J. F., E. Hauksson, and K. Solanki (2006). An evaluation of the SCSN moment tensor solutions: Robustness of the Mw magnitude scale, style of faulting, and automation of the method, *Bull. Seismol. Soc. Am.*, **96**,no.5, 1689–1705, doi: 10.1785/0120050241.
- Dahlen, F. A., and J. Tromp (1998). *Theoretical global seismology*, Princeton university press.
- Davaille, A., and J. M. Lees (2004a). Thermal modeling of subducted plates: tear and hotspot at the Kamchatka corner, *Earth Planet. Sci. Lett.*, **226**,no.3, 293–304.
- Davaille, A., and J. M. Lees (2004b). Thermal modeling of subducted plates: tear and hotspot at the Kamchatka corner, *Earth Planet. Sci. Lett.*, **226**,no.3, 293–304.
- Deffontaines, B., C.-S. Liu, and H.-H. Hsu (2016). Structure and deformation of the Southern Taiwan accretionary prism: The active submarine Fangliao Fault Zone offshore west Hengchun Peninsula, *Tectonophysics*, **692**., 227–240, doi: 10.1016/j.tecto.2016.11.007.
- Deichmann, N. (2006). Local Magnitude, a Moment Revisited, *Bull. Seismol. Soc. Am.*, **96**,no.4A, 1267–1277, doi: 10.1785/0120050115.
- Dreger, D. S. (2003). TDMT_INV: Time domain seismic moment tensor inversion, in *International Handbook of Earthquake and Engineering Seismology*, vol. B, edited by H. Kanamori P. C. Jennings W. H. K. Lee and C. Kisslinger, p. 1627, Academic Press, An Imprint of Elsevier Science, London.
- Dreger, D. S., and D. V. Helmberger (1993). Determination of source parameters at regional distances with three-component sparse network data, *J. Geophys. Res.*, **98**,no.B5, 8107–8125, doi: 10.1029/93jb00023.

- 
- Dziewonski, A. M., T.-A. Chou, and J. H. Woodhouse (1981). Determination of earthquake source parameters from waveform data for studies of global and regional seismicity, *J. Geophys. Res.*, **86**,no.B4, 2825–2852, doi: 10.1029/jb086ib04p02825.
- Edwards, B., B. Allmann, D. Fäh, and J. Clinton (2010). Automatic computation of moment magnitudes for small earthquakes and the scaling of local to moment magnitude, *Geophys. J. Int.*, **183**,no.1, 407–420, doi: 10.1111/j.1365-246x.2010.04743.x.
- Ekström, G., M. Nettles, and A. Dziewoski (2012). The global CMT project 2004–2010: centroid-moment tensors for 13,017 earthquakes, *Phys. Earth Planet. In.*, **200**,, 1–9, doi: 10.1016/j.pepi.2012.04.002.
- Fletcher, J. B., P. Spudich, and L. M. Baker (2006). Rupture propagation of the 2004 Parkfield, California, earthquake from observations at the UPSAR, *Bull. Seismol. Soc. Am.*, **96**,no.4B, S129–S142, doi: 10.1785/0120050812.
- Freed, A. M., and J. Lin (2001). Delayed triggering of the 1999 Hector Mine earthquake by viscoelastic stress transfer, *Nature*, **411**,no.6834, 180, doi: 10.1038/35075548.
- Frohlich, C. (2001). Display and quantitative assessment of distributions of earthquake focal mechanisms, *Geophys. J. Int.*, **144**,no.2, 300–308, doi: 10.1046/j.1365-246x.2001.00341.x.
- Frohlich, C. (2006). *Deep earthquakes*, Cambridge university press.
- Fukahata, Y., Y. Yagi, and L. Rivera (2014). Theoretical relationship between back-projection imaging and classical linear inverse solutions, *Geophys. J. Int.*, **196**,no.1, 552–559.
- Fukao, Y., and M. Obayashi (2013). Subducted slabs stagnant above, penetrating through, and trapped below the 660 km discontinuity, *J. Geophys. Res.*, **118**,no.11, 5920–5938, doi: 10.1002/2013jb010466.
- Fukuyama, E., and D. S. Dreger (2000). Performance test of an automated moment tensor determination system for the future “Tokai” earthquake, *Earth Planets Space*, **52**,no.6, 383–392, doi: 10.1186/bf03352250.
- Furukawa, Y. (1994). Two types of deep seismicity in subducting slabs, *Geophys. Res. Lett.*, **21**,no.12, 1181–1184, doi: 10.1029/94gl01083.
- Gasperini, P., B. Lolli, G. Vannucci, and E. Boschi (2012). A comparison of moment magnitude estimates for the European—Mediterranean and Italian regions, *Geophys. J. Int.*, **190**,no.3, 1733–1745.
- Goldstein, P., and R. J. Archuleta (1987). Array analysis of seismic signals, *Geophys. Res. Lett.*, **14**,no.1, 13–16, doi: 10.1029/gl014i001p00013.
- Gomberg, J., P. Reasenberg, P. Bodin, and R. Harris (2001). Earthquake triggering by seismic waves following the Landers and Hector Mine earthquakes, *Nature*, **411**,no.6836, 462, doi: 10.1038/35078053.
- Gorbatov, A., and V. Kostoglodov (1997). Maximum depth of seismicity and thermal parameter of the subducting slab: general empirical relation and its application, *Tectonophysics*, **277**,no.1-3, 165–187, doi: 10.1016/s0040-1951(97)00084-x.
- Gorbatov, A., V. Kostoglodov, G. Suárez, and E. Gordeev (1997). Seismicity and structure of the Kamchatka subduction zone, *J. Geophys. Res.*, **102**,no.B8, 17883–17898, doi: 10.1029/96jb03491.

- 
- Green II, H. W., and P. C. Burnley (1989). A new self-organizing mechanism for deep-focus earthquakes, *Nature*, **341**,no.6244, 733–737, doi: 10.1038/341733a0.
- Green II, H. W., and H. Houston (1995). The Mechanics of Deep Earthquakes, *Annu. Rev. Earth Planet. Sci.*, **23**,no.1, 169–213, doi: 10.1146/annurev.ea.23.050195.001125.
- Hanks, T. C., and D. M. Boore (1984). Moment-magnitude relations in theory and practice, *J. Geophys. Res. Solid Earth*, **89**,no.B7, 6229–6235, doi: 10.1029/jb089ib07p06229.
- Hayes, G. P., D. J. Wald, and R. L. Johnson (2012). Slab1.0: A three-dimensional model of global subduction zone geometries, *J. Geophys. Res.*, **117**,no.B1, doi: 10.1029/2011JB008524.
- Heaton, H. K. D. L. A. T. H. (1998). Frictional Melting During the Rupture of the 1994 Bolivian Earthquake, *Science*, **279**,no.5352, 839, doi: 10.1126/science.279.5352.839.
- Houston, H., and J. E. Vidale (1994). The temporal distribution of seismic radiation during deep earthquake rupture, *Science*, **265**,no.5173, 771–774, doi: 10.1126/science.265.5173.771.
- Hsu, Y.-J., S.-B. Yu, M. Simons, L.-C. Kuo, and H.-Y. Chen (2009). Interseismic crustal deformation in the Taiwan plate boundary zone revealed by GPS observations, seismicity, and earthquake focal mechanisms, *Tectonophysics*, **479**,no.1-2, 4–18, doi: 10.1016/j.tecto.2008.11.016.
- Hsu, Y.-J., L. Rivera, Y.-M. Wu, C.-H. Chang, and H. Kanamori (2010). Spatial heterogeneity of tectonic stress and friction in the crust: new evidence from earthquake focal mechanisms in Taiwan, *Geophys. J. Int.*, no–no, doi: 10.1111/j.1365-246x.2010.04609.x.
- Hsu, Y.-J., S.-B. Yu, L.-C. Kuo, Y.-C. Tsai, and H.-Y. Chen (2011a). Coseismic deformation of the 2010 Jiashian, Taiwan earthquake and implications for fault activities in southwestern Taiwan, *Tectonophysics*, **502**,no.3-4, 328–335, doi: 10.1016/j.tecto.2011.02.005.
- Hsu, Y.-J., S.-B. Yu, L.-C. Kuo, Y.-C. Tsai, and H.-Y. Chen (2011b). Coseismic deformation of the 2010 Jiashian, Taiwan earthquake and implications for fault activities in southwestern Taiwan, *Tectonophysics*, **502**,no.3-4, 328–335, doi: 10.1016/j.tecto.2011.02.005.
- Huang, B.-S., Y.-L. Huang, S.-J. Lee, Y.-G. Chen, and J. S. Jiang (2008). Initial Rupture and Processes of the and Pingtung Earthquake and from near and Source Strong-Motion and Records, *Terr. Atmos. Ocean. Sci.*, **19**,no.6, 547–554, doi: 10.3319/TAO.2008.19.6.547(PT).
- Huang, G. D., S. W. Roecker, V. Levin, H. Wang, and Z. Li (2017). Dynamics of intracontinental convergence between the western Tarim basin and central Tien Shan constrained by centroid moment tensors of regional earthquakes, *Geophys. J. Int.*, **208**,no.1, 561–576, doi: 10.1093/gji/ggw415.
- Huang, H.-H., Y.-M. Wu, T.-L. Lin, W.-A. Chao, J. B. H. Shyu, C.-H. Chan, and C.-H. Chang (2011). The Preliminary Study of the 4 March 2010 Mw 6.3 Jiasian and Taiwan and Earthquake Sequence, *Terr. Atmos. Ocean. Sci.*, **22**,no.3, 283–290, doi: 10.3319/TAO.2010.12.13.01(T).
- Huang, H.-H., Y.-M. Wu, X. Song, C.-H. Chang, S.-J. Lee, T.-M. Chang, and H.-H. Hsieh (2014). Joint Vp and Vs tomography of Taiwan: Implications for subduction-collision orogen, *Earth Planet. Sci. Lett.*, **392**,, 177–191, doi: 10.1016/j.epsl.2014.02.026.
- Huang, R.-H., and T.-L. Lin (2017). On-line application of the waveform stacking method for the local EEW arrays in Taiwan: A case study of the 6 February, 2016, Mw 6.4 Meinong, Taiwan earthquake, in *EGU General Assembly Conference Abstracts*, vol. 19, p. 11602.
- Huang, W.-G., J.-H. Wang, B.-S. Huang, K.-C. Chen, T.-M. Chang, R.-D. Hwang, H.-C. Chiu, and C.-C.

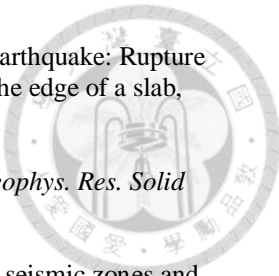
- 
- P. Tsai (2001). Estimates of source parameters for the 1999 Chi-Chi, Taiwan, earthquake based on Brune's source model, *Bull. Seismol. Soc. Am.*, **91**,no.5, 1190–1198.
- Ide, S. (2015). Slip Inversion, in *Treatise on Geophysics*, pp. 215–241, Elsevier.
- Iidaka, T., and Y. Furukawa (1994). Double Seismic Zone for Deep Earthquakes in the Izu-Bonin Subduction Zone, *Science*, **263**,no.5150, 1116–1118, doi: 10.1126/science.263.5150.1116.
- International Seismological Centre (2015). *On-line Bulletin*, Internatl. Seismol. Cent., Thatcham, United Kingdom.
- Isacks, B., J. Oliver, and L. R. Sykes (1968). Seismology and the new global tectonics, *J. Geophys. Res.*, **73**,no.18, 5855–5899, doi: 10.1002/9781118782149.ch7.
- Ishii, M., P. M. Shearer, H. Houston, and J. E. Vidale (2005). Extent, duration and speed of the 2004 Sumatra-Andaman earthquake imaged by the Hi-Net array, *Nature*, **435**,no.7044, 933–936, doi: 10.1038/nature03675.
- Ishii, M., P. M. Shearer, H. Houston, and J. E. Vidale (2007). Teleseismic P wave imaging of the 26 December 2004 Sumatra-Andaman and 28 March 2005 Sumatra earthquake ruptures using the Hi-net array, *J. Geophys. Res.*, **112**,, B11307, doi: 10.1029/2006JB004700.
- Ito, Y., S. Sekiguchi, T. Okada, R. Honda, K. Obara, and S. Hori (2006). Performance of regional distance centroid moment tensor inversion applied to the 2004 mid-Niigata prefecture earthquake, Japan, *Geophys. J. Int.*, **167**,no.3, 1317–1331, doi: 10.1111/j.1365-246x.2006.03109.x.
- Ji, C., D. J. Wald, and D. V. Helmberger (2002). Source description of the 1999 Hector Mine, California, earthquake, part I: Wavelet domain inversion theory and resolution analysis, *Bull. Seismol. Soc. Am.*, **92**,no.4, 1192–1207.
- Jian, P.-R., S.-H. Hung, L. Meng, and D. Sun (2017). Rupture characteristics of the 2016 Meinong earthquake revealed by the back projection and directivity analysis of teleseismic broadband waveforms, *Geophys. Res. Lett.*, **44**,no.8, 3545–3553, doi: 10.1002/2017gl072552.
- Jian, P.-R., T.-L. Tseng, W.-T. Liang, and P.-H. Huang (2018). A new automatic full-waveform regional moment tensor inversion algorithm and its applications in the Taiwan area, *Bull. Seismol. Soc. Am.*, **108**,no.2, 573–587, doi: 10.1785/0120170231.
- Jiang, G., D. Zhao, and G. Zhang (2008). Seismic evidence for a metastable olivine wedge in the subducting Pacific slab under Japan Sea, *Earth Planet. Sci. Lett.*, **270**,no.3, 300–307.
- John, T., S. Medvedev, L. H. Rüpke, T. B. Andersen, Y. Y. Podladchikov, and H. Austrheim (2009). Generation of intermediate-depth earthquakes by self-localizing thermal runaway, *Nat. Geosci.*, **2**,no.2, 137–140.
- Jost, M. L., and R. B. Herrmann (1989). A student's guide to and review of moment tensors, *Seismol. Res. Lett.*, **60**,no.2, 37–57, doi: 10.1785/gssrl.60.2.37.
- Kagan, Y. Y. (2002). Modern California Earthquake Catalogs and Their Comparison, *Seismol. Res. Lett.*, **73**,no.6, 921–929, doi: 10.1785/gssrl.73.6.921.
- Kagan, Y. Y. (2003). Accuracy of modern global earthquake catalogs, *Phys. Earth Planet. In.*, **135**,no.2, 173–209, doi: 10.1016/s0031-9201(02)00214-5.
- Kagan, Y. Y., and D. Jackson (1999). Worldwide doublets of large shallow earthquakes, *Bull. Seismol. Soc. Am.*, **89**,no.5, 1147–1155.

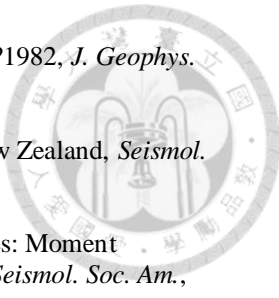
- 
- Kanamori, H., D. L. Anderson, and T. H. Heaton (1998). Frictional melting during the rupture of the 1994 Bolivian earthquake, *Science*, **279**,no.5352, 839–842, doi: 10.1126/science.279.5352.839.
- Kanamori, H., L. Ye, B.-S. Huang, H.-H. Huang, S.-J. Lee, W.-T. Liang, Y.-Y. Lin, K.-F. Ma, Y.-M. Wu, and T.-Y. Yeh (2017). A strong-motion hot spot of the 2016 Meinong, Taiwan, earthquake (Mw=6.4), *Terr. Atmos. Ocean. Sci.*, **28**,no.5, 637–650, doi: 10.3319/TAO.2016.10.07.01.
- Kaneshima, S., T. Okamoto, and H. Takenaka (2007). Evidence for a metastable olivine wedge inside the subducted Mariana slab, *Earth Planet. Sci. Lett.*, **258**,no.1, 219–227.
- Kao, H., and W.-P. Chen (2000). The Chi-Chi earthquake sequence: Active, out-of-sequence thrust faulting in Taiwan, *Science*, **288**,no.5475, 2346–2349, doi: 10.1126/science.288.5475.2346.
- Kao, H., and P.-R. Jian (1999). Source parameters of regional earthquakes in Taiwan: July 1995–December 1996, *Terr. Atmos. Ocean. Sci.*, **10**,, 585–604, doi: 10.3319/TAO.1999.10.3.585(T).
- Kao, H., and P.-R. Jian (2001). Seismogenic patterns in the Taiwan region: insights from source parameter inversion of BATS data, *Tectonophysics*, **333**,no.1, 179–198, doi: 10.1016/s0040-1951(00)00274-2.
- Kao, H., and R.-J. Rau (1999). Detailed structures of the subducted Philippine Sea plate beneath northeast Taiwan: a new type of double seismic zone, *J. Geophys. Res.*, **104**,no.B1, 1015–1033, doi: 10.1029/1998jb900010.
- Kao, H., P.-R. Jian, K.-F. Ma, B.-S. Huang, and C.-C. Liu (1998a). Moment-tensor inversion for offshore earthquakes east of Taiwan and their implications to regional collision, *Geophys. Res. Lett.*, **25**,no.19, 3619–3622, doi: 10.1029/98GL02803.
- Kao, H., S. J. Shen, and K.-F. Ma (1998b). Transition from oblique subduction to collision: Earthquakes in the southernmost Ryukyu arc-Taiwan region, *J. Geophys. Res. Solid Earth*, **103**,no.B4, 7211–7229, doi: 10.1029/97JB03510.
- Kao, H., G.-C. Huang, and C.-S. Liu (2000). Transition from oblique subduction to collision in the northern Luzon arc-Taiwan region: Constraints from bathymetry and seismic observations, *J. Geophys. Res.*, **105**,no.B2, 3059–3079, doi: 10.1029/1999jb900357.
- Kao, H., Y.-H. Liu, W.-T. Liang, and W.-P. Chen (2002). Source parameters of regional earthquakes in Taiwan: 1999–2000 including the Chi-Chi earthquake sequence, *Terr. Atmos. Ocean. Sci.*, **13**,no.3, 279–298, doi: 10.3319/tao.2002.13.3.279(CCE).
- Karato, S., M. R. Riedel, and D. A. Yuen (2001). Rheological structure and deformation of subducted slabs in the mantle transition zone: implications for mantle circulation and deep earthquakes, *Phys. Earth Planet. In.*, **127**,no.1, 83–108.
- Kawakatsu, H., and S. Yoshioka (2011). Metastable olivine wedge and deep dry cold slab beneath southwest Japan, *Earth Planet. Sci. Lett.*, **303**,no.1, 1–10.
- Kilb, D., J. Gomberg, and P. Bodin (2000). Triggering of earthquake aftershocks by dynamic stresses, *Nature*, **408**,no.6812, 570–574.
- Kirby, S. H., W. B. Durham, and L. A. Stern (1991). Mantle Phase Changes and Deep-Earthquake Faulting in Subducting Lithosphere, *Science*, **252**,no.5003, 216–225, doi: 10.1126/science.252.5003.216.
- Kirby, S. H., S. Stein, E. A. Okal, and D. C. Rubie (1996). Metastable mantle phase transformations and

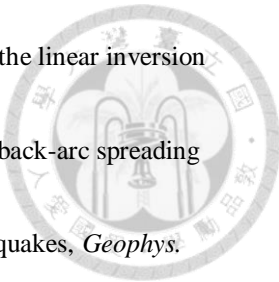
deep earthquakes in subducting oceanic lithosphere, *Rev. Geophys.*, **34**,no.2, 261–306, doi: 10.1029/96RG01050.

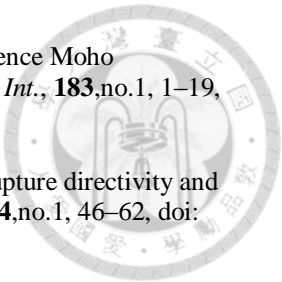
- Kiser, E., and M. Ishii (2012). The March 11, 2011 Tohoku-oki earthquake of the plate interface, *Geophys. Res. Lett.*, **39**,no.7, n/a–n/a, doi: 10.1029/2012GL051170.
- Kiser, E., M. Ishii, C. H. Langmuir, P. M. Shearer, and H. Hirose (2011a). Insights into the mechanism of intermediate -depth earthquakes from source properties as imaged by back projection of multiple seismic phases, *J. Geophys. Res.*, **116**, B06310, doi: 10.1029/2010JB007831.
- Kiser, E., M. Ishii, C. H. Langmuir, P. M. Shearer, and H. Hirose (2011b). Insights into the mechanism of intermediate-depth earthquakes from source properties as imaged by back projection of multiple seismic phases, *J. Geophys. Res.*, **116**,no.B6, doi: 10.1029/2010JB007831.
- Koper, K. D., and D. A. Wiens (2000). The waveguide effect of metastable olivine in slabs, *Geophys. Res. Lett.*, **27**,no.4, 581–584, doi: 10.1029/1999GL011007/full.
- Koper, K. D., A. R. Hutko, T. Lay, C. J. Ammon, and H. Kanamori (2011). Frequency-dependent rupture process of the 2011 M(w) 9.0 Tohoku Earthquake: Comparison of short-period P wave backprojection images and broadband seismic rupture models, *Earth Planets and Space*, **63**,no.7, 599–602, doi: 10.5047/eps.2011.05.026.
- Koper, K. D., A. R. Hutko, T. Lay, and O. Sufri (2012). Imaging short-period seismic radiation from the 27 February 2010 Chile (MW 8.8) earthquake by back-projection of P, PP, and PKIKP waves, *J. Geophys. Res.*, **117**,no.B2, n/a–n/a, doi: 10.1029/2011JB008576.
- Kubo, A., E. Fukuyama, H. Kawai, and K. Nonomura (2002). NIED seismic moment tensor catalogue for regional earthquakes around Japan: quality test and application, *Tectonophysics*, **356**,no.1, 23–48, doi: 10.1016/s0040-1951(02)00375-x.
- Kubo, T., S. Kaneshima, Y. Torii, and S. Yoshioka (2009). Seismological and experimental constraints on metastable phase transformations and rheology of the Mariana slab, *Earth Planet. Sci. Lett.*, **287**,no.1-2, 12–23, doi: 10.1016/j.epsl.2009.07.028.
- Kuo-Chen, H., F. T. Wu, and S. W. Roecker (2012). Three-dimensional P velocity structures of the lithosphere beneath Taiwan from the analysis of TAIGER and related seismic data sets, *J. Geophys. Res. Solid Earth*, **117**,no.B6.
- Lacombe, O., F. Mouthereau, J. Angelier, and B. Deffontaines (2001). Structural, geodetic and seismological evidence for tectonic escape in SW Taiwan, *Tectonophysics*, **333**,no.1, 323–345, doi: 10.1016/s0040-1951(00)00281-x.
- Lallemand, S., Y. Font, H. Bijwaard, and H. Kao (2001). New insights on 3-D plates interaction near Taiwan from tomography and tectonic implications, *Tectonophysics*, **335**,no.3, 229–253.
- Lay, T., and H. Kanamori (1980). Earthquake doublets in the Solomon Islands, *Phys. Earth Planet. In.*, **21**,no.4, 283–304, doi: 10.1016/0031-9201(80)90134-x.
- Lee, E.-J., P. Chen, T. H. Jordan, and L. Wang (2011). Rapid full-wave centroid moment tensor (CMT) inversion in a three-dimensional earth structure model for earthquakes in Southern California, *Geophys. J. Int.*, **186**,no.1, 311–330.
- Lee, S.-J., W.-T. Liang, and B.-S. Huang (2008). Source mechanisms and rupture processes of the 26 December 2006 Pingtung earthquake doublet as determined from the regional seismic records, *Terr. Atmos. Ocean. Sci.*, **19**,no.6, 555–565, doi: 10.3319/TAO.2008.19.6.555(PT).

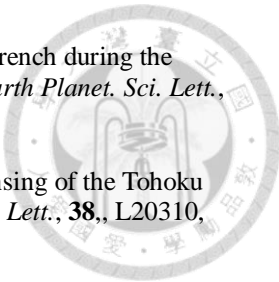
- Lee, S.-J., L. Mozziconacci, W.-T. Liang, Y.-J. Hsu, W.-G. Huang, and B.-S. Huang (2013). Source complexity of the 4 March 2010 Jiashiah, Taiwan, Earthquake determined by joint inversion of teleseismic and near field data, *J. Asian Earth Sci.*, **64**, 14–26, doi: 10.1016/j.jseaes.2012.11.018.
- Lee, S.-J., W.-T. Liang, H.-W. Cheng, F.-S. Tu, K.-F. Ma, H. Tsuruoka, H. Kawakatsu, B.-S. Huang, and C.-C. Liu (2014). Towards real-time regional earthquake simulation I: Real-time moment tensor monitoring (RMT) for regional events in Taiwan, *Geophys. J. Int.*, **196**,no.1, 432–446, doi: 10.1093/gji/ggt371.
- Lee, S.-J., T.-Y. Yeh, and Y.-Y. Lin (2016). Anomalous large ground motion in the 2016 ML 6.6 Meinong, Taiwan, earthquake: A synergy effect of source rupture and site amplification, *Seismol. Res. Lett.*, **87**,no.6, 1319–1326, doi: 10.1785/0220160082.
- Liang, W.-T., Y.-H. Liu, H. Kao, and others (2004). Source parameters of regional earthquakes in Taiwan: January–December, 2002, *Terr. Atmos. Ocean. Sci.*, **15**,no.4, 727–742, doi: 10.3319/TAO.2004.15.4.727(T).
- Liang, W.-T., J.-C. Lee, K. H. Chen, and N.-C. Hsiao (2017). Citizen Earthquake Science in Taiwan: From Science to Hazard Mitigation, *Journal of Disaster Research*, **12**,no.6, 1174–1181, doi: 10.20965/jdr.2017.p1174.
- Lin, J., and R. S. Stein (2004). Stress triggering in thrust and subduction earthquakes and stress interaction between the southern San Andreas and nearby thrust and strike-slip faults, *J. Geophys. Res. Solid Earth*, **109**,no.B2, doi: 10.1029/2003JB002607.
- Lin, J.-Y., J.-C. Sibuet, C.-S. Lee, S.-K. Hsu, and F. Klingelhoefer (2007). Origin of the southern Okinawa Trough volcanism from detailed seismic tomography, *J. Geophys. Res. Solid Earth*, **112**,no.B8, doi: 10.1029/2006jb004703.
- Marone, C., and M. Liu (1997). Transformation shear instability and the seismogenic zone for deep earthquakes, *Geophys. Res. Lett.*, **24**,no.15, 1887–1890, doi: 10.1029/97gl01851.
- Martin, R., D. Stich, J. Morales, and F. Mancilla (2015). Moment tensor solutions for the Iberian-Maghreb region during the IberArray deployment (2009–2013), *Tectonophysics*, **663**, 261–274, doi: 10.1016/j.tecto.2015.08.012.
- McKenzie, D. P. (1969). Speculations on the consequences and causes of plate motions, *Geophys. J. Int.*, **18**,no.1, 1–32, doi: 10.1111/j.1365-246x.1969.tb00259.x.
- Meade, C., and R. Jeanloz (1991). Deep-Focus Earthquakes and Recycling of Water into the Earth's Mantle, *Science*, **252**,no.5002, 68–72, doi: 10.1126/science.252.5002.68.
- Mellman, G., L. Burdick, and D. Helmberger (1975). Determination of source parameters from body wave seismograms, *Earthquake Notes*, **46**,no.1, 44.
- Meng, L., A. Inbal, and J.-P. Ampuero (2011). A window into the complexity of the dynamic rupture of the 2011 Mw 9 Tohoku-Oki earthquake, *Geophys. Res. Lett.*, **38**,no.7, L00G07, doi: 10.1029/2011GL048118.
- Meng, L., J.-P. Ampuero, A. Sladen, and H. Rendon (2012a). High-resolution backprojection at regional distance: Application to the HaitiM7.0 earthquake and comparisons with finite source studies, *J. Geophys. Res.*, **117**,no.B4, doi: 10.1029/2011JB008702.
- Meng, L., J.-P. Ampuero, Y. Luo, W. Wu, and S. Ni (2012b). Mitigating artifacts in back-projection source imaging with implications for frequency-dependent properties of the Tohoku-Oki earthquake, *Earth Planets and Space*, **64**,no.12, 1101–1109, doi: 10.5047/eps.2012.05.010.

- 
- Meng, L., J.-P. Ampuero, and R. Bürgmann (2014). The 2013 Okhotsk deep-focus earthquake: Rupture beyond the metastable olivine wedge and thermally controlled rise time near the edge of a slab, *Geophys. Res. Lett.*, **41**,no.11, 3779–3785.
- Michael, A. J. (1984). Determination of stress from slip data: Faults and folds, *J. Geophys. Res. Solid Earth*, **89**,no.B13, 11517–11526, doi: 10.1029/jb089ib13p11517.
- Molnar, P., D. Freedman, and J. S. F. Shih (1979). Lengths of intermediate and deep seismic zones and temperatures in downgoing slabs of lithosphere, *Geophysical Journal of the Royal Astronomical Society*, **56**,no.1, 41–54, doi: 10.1111/j.1365-246X.1979.tb04766.x.
- Mosenfelder, J. L., F. C. Marton, C. R. Ross, L. Kerschhofer, and D. C. Rubie (2001). Experimental constraints on the depth of olivine metastability in subducting lithosphere, *Phys. Earth Planet. In.*, **127**,no.1-4, 165–180, doi: 10.1016/s0031-9201(01)00226-6.
- Myers, S. C., T. C. Wallace, S. L. Beck, P. G. Silver, G. Zandt, J. Vandecar, and E. Minaya (1995). Implications of spatial and temporal development of the aftershock sequence for the Mw 8.3 June 9, 1994 deep Bolivian earthquake, *Geophys. Res. Lett.*, **22**,no.16, 2269–2272, doi: 10.1029/95gl01600.
- Nakano, M., H. Kumagai, and H. Inoue (2008). Waveform inversion in the frequency domain for the simultaneous determination of earthquake source mechanism and moment function, *Geophys. J. Int.*, **173**,no.3, 1000–1011, doi: 10.1111/j.1365-246x.2008.03783.x.
- Ogawa, M. (1987). Shear instability in a viscoelastic material as the cause of deep focus earthquakes, *Journal of Geophysical Research: Solid Earth (1978–2012)*, **92**,no.B13, 13801–13810, doi: 10.1029/JB092iB13p13801.
- Park, J., V. Levin, M. Brandon, J. Lees, V. Peyton, E. Gordeev, and A. Ozerov (2002). A dangling slab, amplified arc volcanism, mantle flow and seismic anisotropy in the Kamchatka plate corner, in *Mantle Dynamics and Plate Interactions in East Asia*, vol. 30, pp. 295–324, American Geophysical Union.
- Park, S., and M. Ishii (2015). Inversion for rupture properties based upon 3-D directivity effect and application to deep earthquakes in the Sea of Okhotsk region, *Geophys. J. Int.*, **203**,no.2, 1011–1025, doi: 10.1093/gji/ggv352.
- Parsons, T., and D. S. Dreger (2000). Static-stress impact of the 1992 Landers earthquake sequence on nucleation and slip at the site of the 1999 M= 7.1 Hector Mine earthquake, southern California, *Geophys. Res. Lett.*, **27**,no.13, 1949–1952, doi: 10.1029/1999gl011272.
- Peacock, S. M. (2001). Are the lower planes of double seismic zones caused by serpentine dehydration in subducting oceanic mantle?, *Geology*, **29**,no.4, 299, doi: 10.1130/0091-7613(2001)029<0299:ATLPOD>2.0.CO;2.
- Peyton, V., V. Levin, J. Park, M. Brandon, J. Lees, E. Gordeev, and A. Ozerov (2001). Mantle flow at a slab edge: Seismic anisotropy in the Kamchatka region, *Geophys. Res. Lett.*, **28**,no.2, 379–382, doi: 10.1029/2000gl012200.
- Pondrelli, S., A. Morelli, G. Ekström, S. Mazza, E. Boschi, and A. Dziewonski (2002). European–Mediterranean regional centroid-moment tensors: 1997–2000, *Phys. Earth Planet. In.*, **130**,no.1, 71–101, doi: 10.1016/s0031-9201(01)00312-0.
- Rau, R.-J., and F. T. Wu (1995). Tomographic imaging of lithospheric structures under Taiwan, *Earth Planet. Sci. Lett.*, **133**,no.3, 517–532, doi: 10.1016/0012-821x(95)00076-o.

- 
- Reasenbergs, P. (1985). Second-order moment of central California seismicity, 1969–1982, *J. Geophys. Res. Solid Earth*, **90**,no.B7, 5479–5495, doi: 10.1029/JB090iB07p05479.
- Ristau, J. (2008). Implementation of routine regional moment tensor analysis in New Zealand, *Seismol. Res. Lett.*, **79**,no.3, 400–415, doi: 10.1785/gssrl.79.3.400.
- Ristau, J. (2009). Comparison of Magnitude Estimates for New Zealand Earthquakes: Moment Magnitude, Local Magnitude, and Teleseismic Body-Wave Magnitude, *Bull. Seismol. Soc. Am.*, **99**,no.3, 1841–1852, doi: 10.1785/0120080237.
- Rost, S., and C. Thomas (2002). Array seismology: Methods and applications, *Rev. Geophys.*, **40**,no.3, 1008, doi: 10.1029/2000RG000100.
- Rueda, J., and J. Mezcua (2005). Near-real-time seismic moment-tensor determination in Spain, *Seismol. Res. Lett.*, **76**,no.4, 455–465, doi: 10.1785/gssrl.76.4.455.
- Schmidt, R. O. (1986). Multiple Emitter Location and Signal Parameter-estimation, *IEEE Trans. Antennas Propag.*, **34**,no.3, 276 – 280, doi: 10.1109/TAP.1986.1143830.
- Schorlemmer, D., and S. Wiemer (2005). Earth science: Microseismicity data forecast rupture area, *Nature*, **434**,no.7037, 1086–1086.
- Scognamiglio, L., E. Tinti, and A. Michelini (2009). Real-time determination of seismic moment tensor for the Italian region, *Bull. Seismol. Soc. Am.*, **99**,no.4, 2223–2242, doi: 10.1785/0120080104.
- Seno, T., S. Stein, and A. E. Gripp (1993). A model for the motion of the Philippine Sea plate consistent with NUVEL-1 and geological data, *J. Geophys. Res. Solid Earth*, **98**,no.B10, 17941–17948.
- Shi, Y., and B. A. Bolt (1982). The standard error of the magnitude-frequency b value, *Bull. Seismol. Soc. Am.*, **72**,no.5, 1677–1687.
- Shin, T.-C. (1993). The calculation of local magnitude from the simulated Wood-Anderson seismograms of the short-period seismograms in the Taiwan area, *Terr. Atmos. Ocean. Sci.*, **4**,, 155–170, doi: 10.3319/TAO.1993.4.2.155(T).
- Sileny, J., P. Campus, and G. F. Panza (1996). Seismic moment tensor resolution by waveform inversion of a few and local noisy records-I. Synthetic and tests, *Geophys. J. Int.*, **126**,, 605–619.
- Silver, P. G., S. L. Beck, T. C. Wallace, C. Meade, and others (1995). Rupture characteristics of the deep Bolivian earthquake of 9 June 1994 and the mechanism of deep-focus earthquakes, *Science*, **268**,no.5207, 69, doi: 10.1126/science.268.5207.69.
- Spikin, S. A. (1986). Estimation of earthquake source parameters by the inversion of waveform data: global seismicity, 1981–1983, *Bull. Seismol. Soc. Am.*, **76**,no.6, 1515–1541.
- Starr, A. (1928). Slip in a crystal and rupture in a solid due to shear, in *Mathematical Proceedings of the Cambridge Philosophical Society*, vol. 24, pp. 489–500, Cambridge University Press (CUP).
- Stein, R. S., G. C. King, and J. Lin (1994). Stress triggering of the 1994 M=6.7 Northridge, California, earthquake by its predecessors, *Science*, **265**,no.5177, 1432–1435, doi: 10.1126/science.265.5177.1432.
- Stich, D., C. J. Ammon, and J. Morales (2003). Moment tensor solutions for small and moderate earthquakes in the Ibero-Maghreb region, *J. Geophys. Res. Solid Earth*, **108**,no.B3, doi: 10.1029/2002jb002057.

- 
- Stump, B. W., and L. R. Johnson (1977). The determination of source properties by the linear inversion of seismograms, *Bull. Seismol. Soc. Am.*, **67**,no.6, 1489–1502.
- Suppe, J. (1984). Kinematics of arc-continent collision, flipping of subduction, and back-arc spreading near Taiwan, *Mem. Geol. Soc. China*, **6**,no.21, V33.
- Suzuki, M., and Y. Yagi (2011). Depth dependence of rupture velocity in deep earthquakes, *Geophys. Res. Lett.*, **38**,no.5, n/a–n/a, doi: 10.1029/2011GL046807.
- Tange, O. (2011). GNU Parallel - The Command-Line Power Tool, ;login: *The USENIX Magazine*, **36**,no.1, 42–47, doi: 10.5281/zenodo.16303.
- Thomson, D. J. (1982). Spectrum estimation and harmonic analysis, *Proc. IEEE*, **70**,no.9, 1055–1096.
- Tibi, R., D. A. Wiens, and H. Inoue (2003a). Remote triggering of deep earthquakes in the 2002 Tonga sequences, *Nature*, **424**,no.6951, 921–925.
- Tibi, R., G. Bock, and D. A. Wiens (2003b). Source characteristics of large deep earthquakes: Constraint on the faulting mechanism at great depths, *J. Geophys. Res.*, **108**,no.B2, 2091, doi: 10.1029/2002JB001948.
- Toda, S., R. S. Stein, K. Richards-Dinger, and S. B. Bozkurt (2005). Forecasting the evolution of seismicity in southern California: Animations built on earthquake stress transfer, *J. Geophys. Res. Solid Earth*, **110**,no.B5, n/a–n/a, doi: 10.1029/2004JB003415.
- Tseng, T.-L., H.-C. Hsu, P.-R. Jian, B.-S. Huang, J.-C. Hu, and S.-L. Chung (2016). Focal mechanisms and stress variations in the Caucasus and northeast Turkey from constraints of regional waveforms, *Tectonophysics*, **691**,, 362–374, doi: 10.1016/j.tecto.2016.10.028.
- Utsu, T. (1966). A statistical significance test of the difference in b-value between two earthquake groups, *Journal of Physics of the Earth*, **14**,no.2, 37–40.
- Utsu, T. (1992). Introduction to seismicity, *Mathematical Seismology*, **7**,, 139–157.
- Vallée, M., J. Charléty, A. M. Ferreira, B. Delouis, and J. Vergoz (2011). SCARDEC: a new technique for the rapid determination of seismic moment magnitude, focal mechanism and source time functions for large earthquakes using body-wave deconvolution, *Geophys. J. Int.*, **184**,no.1, 338–358, doi: 10.1111/j.1365-246x.2010.04836.x.
- Vandecar, J. C., and R. S. Crosson (1990). Determination of teleseismic relative phase arrival times using multi-channel cross-correlation and least squares, *Bull. Seismol. Soc. Am.*, **80**,No.1,, 150–169.
- Waldhauser, F., and W. L. Ellsworth (2000). A double-difference earthquake location algorithm: Method and application to the northern Hayward fault, California, *Bull. Seismol. Soc. Am.*, **90**,no.6, 1353–1368, doi: 10.1785/0120000006.
- Walker, K. T., and P. M. Shearer (2009). Illuminating the near-sonic rupture velocities of the intracontinental Kokoxili Mw 7.8 and Denali fault Mw 7.9 strike-slip earthquakes with global P wave back projection imaging, *J. Geophys. Res. Solid Earth*, **114**,no.B2, doi: 10.1029/2008jb005738.
- Wallace, T. C., D. V. Helmberger, and G. R. Mellman (1981). A technique for the inversion of regional data in source parameter studies, *J. Geophys. Res.*, **86**,no.B3, 1679, doi: 10.1029/jb086ib03p01679.

- 
- Wang, H.-L., H.-W. Chen, and L. Zhu (2010). Constraints on average Taiwan Reference Moho Discontinuity Model-receiver function analysis using BATS data, *Geophys. J. Int.*, **183**,no.1, 1–19, doi: 10.1111/j.1365-246x.2010.04692.x.
- Warren, L. M., and P. M. Shearer (2006). Systematic determination of earthquake rupture directivity and fault planes from analysis of long-period P -wave spectra, *Geophys. J. Int.*, **164**,no.1, 46–62, doi: 10.1111/j.1365-246X.2005.02769.x.
- Wiemer, S., and J. P. Benoit (1996). Mapping the B-value anomaly at 100 km depth in the Alaska and New Zealand Subduction Zones, *Geophys. Res. Lett.*, **23**,no.13, 1557–1560, doi: 10.1029/96gl01233.
- Wiemer, S., and K. Katsumata (1999). Spatial variability of seismicity parameters in aftershock zones, *J. Geophys. Res. Solid Earth*, **104**,no.B6, 13135–13151.
- Wiemer, S., and D. Schorlemmer (2007). ALM: An asperity-based likelihood model for California, *Seismol. Res. Lett.*, **78**,no.1, 134–140.
- Wiemer, S., and M. Wyss (1994). Seismic quiescence before the Landers (M= 7.5) and Big Bear (M= 6.5) 1992 earthquakes, *Bull. Seismol. Soc. Am.*, **84**,no.3, 900–916.
- Wiemer, S., and M. Wyss (1997). Mapping the frequency-magnitude distribution in asperities: An improved technique to calculate recurrence times?, *J. Geophys. Res. Solid Earth*, **102**,no.B7, 15115–15128, doi: 10.1029/97jb00726.
- Wiemer, S., and M. Wyss (2000). Minimum magnitude of completeness in earthquake catalogs: Examples from Alaska, the western United States, and Japan, *Bull. Seismol. Soc. Am.*, **90**,no.4, 859–869.
- Wiemer, S., and M. Wyss (2002). Mapping spatial variability of the frequency-magnitude distribution of earthquakes, *Advances in geophysics*, **45**,, 259–V.
- Wiens, D. A., and J. J. McGuire (1995). The 1994 Bolivia and Tonga Events - fundamentally different types of deep earthquakes, *Geophys. Res. Lett.*, **22**,no.16, 2245–2248, doi: 10.1029/95gl01598.
- Wiens, D. A., and N. O. Snider (2001). Repeating deep earthquakes: evidence for fault reactivation at great depth, *Science*, **293**,no.5611, 1463–1466, doi: 10.1126/science.1063042.
- Wiens, D. A., J. J. McGuire, P. J. Shore, M. G. Bevis, K. Draunidalo, G. Prasad, and S. P. Helu (1994). A deep earthquake aftershock sequence and implications for the rupture mechanism of deep earthquakes, *Nature*, **372**,no.6507, 709–709, doi: 10.1038/372540a0.
- Wyss, M., and W. Lee (1973). Time variations of the average earthquake magnitude in central California, in *Proceedings of the conference on tectonic problems of the San Andreas fault system*, pp. 24–42, Stanford University Geol. Sci.
- Wyss, M., K. Shimazaki, and S. Wiemer (1997). Mapping active magma chambers by b values beneath the off-Ito volcano, Japan, *J. Geophys. Res. Solid Earth*, **102**,no.B9, 20413–20422.
- Wyss, M., D. Schorlemmer, and S. Wiemer (2000). Mapping asperities by minima of local recurrence time: San Jacinto-Elsinore fault zones, *J. Geophys. Res. Solid Earth*, **105**,no.B4, 7829–7844, doi: 10.1029/1999jb900347.
- Xu, Y., K. D. Koper, O. Sufri, L. Zhu, and A. R. Hutko (2009). Rupture imaging of the Mw 7.9 12 May 2008 Wenchuan earthquake from back projection of teleseismic P waves, *Geochem. Geophys. Geosyst.*, **10**,no.4, doi: 10.1029/2008GC002335.

- 
- Yagi, Y., A. Nakao, and A. Kasahara (2012). Smooth and rapid slip near the Japan Trench during the 2011 Tohoku-oki earthquake revealed by a hybrid back-projection method, *Earth Planet. Sci. Lett.*, **355-356**, 94–101, doi: 10.1016/j.epsl.2012.08.018.
- Yao, H., P. Gerstoft, P. M. Shearer, and C. Mecklenbräuer (2011). Compressive sensing of the Tohoku -Oki Mw 9.0 earthquake: Frequency-dependent rupture modes, *Geophys. Res. Lett.*, **38**, L20310, doi: 10.1029/2011GL049223.
- Yao, Z., and D. Harkrider (1983). A generalized reflection-transmission coefficient matrix and discrete wavenumber method for synthetic seismograms, *Bull. Seismol. Soc. Am.*, **73**,no.6A, 1685–1699.
- Ye, L., T. Lay, and H. Kanamori (2012). Intraplate and interplate faulting interactions during the August 31, 2012, Philippine Trench earthquake (Mw 7.6) sequence, *Geophys. Res. Lett.*, **39**,no.24, doi: 10.1029/2012GL054164.
- Ye, L., T. Lay, H. Kanamori, and K. D. Koper (2013). Energy Release of the 2013 Mw 8.3 Sea of Okhotsk Earthquake and Deep Slab Stress Heterogeneity, *Science*, **341**,no.6152, 1380–1384, doi: 10.1126/science.1242032.
- Yen, Y.-T., and K.-F. Ma (2011). Source-scaling relationship for M 4.6 – 8.9 earthquakes, specifically for earthquakes in the collision zone of Taiwan, *Bull. Seismol. Soc. Am.*, **101**,no.2, 464–481, doi: 10.1785/0120100046.
- Yu, S.-B., H.-Y. Chen, and L.-C. Kuo (1997). Velocity field of GPS stations in the Taiwan area, *Tectonophysics*, **274**,no.1, 41–59.
- Yu, W.-C., and L. Wen (2012). Deep-Focus Repeating Earthquakes in the Tonga-Fiji Subduction Zone, *Bull. Seismol. Soc. Am.*, **102**,no.4, 1829–1849, doi: 10.1785/0120110272.
- Zhan, Z., B. Jin, S. Wei, and R. W. Graves (2011). Coulomb Stress Change Sensitivity due to Variability in Mainshock Source Models and Receiving Fault Parameters: A Case Study of the 2010-2011 Christchurch, New Zealand, Earthquakes, *Seismol. Res. Lett.*, **82**,no.6, 800–814, doi: 10.1785/gssrl.82.6.800.
- Zhan, Z., H. Kanamori, V. C. Tsai, D. V. Helmberger, and S. Wei (2014). Rupture complexity of the 1994 Bolivia and 2013 Sea of Okhotsk deep earthquakes, *Earth Planet. Sci. Lett.*, **385**, 89–96, doi: 10.1016/j.epsl.2013.10.028.
- Zhu, L., and D. V. Helmberger (1996). Advancement in source estimation techniques using broadband regional seismograms, *Bull. Seismol. Soc. Am.*, **86**,no.5, 1634–1641.
- Zhu, L., and L. A. Rivera (2002). A note on the dynamic and static displacements from a point source and in multilayered media, *Geophys. J. Int.*, **148**,no.3, 619–627, doi: 10.1046/j.1365-246x.2002.01610.x.
- Zhu, L., N. Akyol, B. J. Mitchell, and H. Sozbilir (2006). Seismotectonics of western Turkey from high resolution earthquake relocations and moment tensor determinations, *Geophys. Res. Lett.*, **33**,no.7, doi: 10.1029/2006gl025842.
- Zobin, V. M. (1979). Variations of volcanic earthquake source parameters before volcanic eruptions, *J. Volcanol. Geotherm. Res.*, **6**,no.3-4, 279–293.